
This is an electronic reprint of the original article.
This reprint may differ from the original in pagination and typographic detail.

Liu, Yinping; Niu, Yingchun; Ouyang, Xiangcheng; Guo, Chao; Han, Peiyu; Zhou, Ruichen; Heydari, Ali; Zhou, Yang; Ikkala, Olli; Tigranovich, Glazkov Artem; Xu, Chunming; Xu, Quan
Progress of organic, inorganic redox flow battery and mechanism of electrode reaction

Published in:
Nano Research Energy

DOI:
[10.26599/NRE.2023.9120081](https://doi.org/10.26599/NRE.2023.9120081)

Published: 01/12/2023

Document Version
Publisher's PDF, also known as Version of record

Published under the following license:
CC BY

Please cite the original version:
Liu, Y., Niu, Y., Ouyang, X., Guo, C., Han, P., Zhou, R., Heydari, A., Zhou, Y., Ikkala, O., Tigranovich, G. A., Xu, C., & Xu, Q. (2023). Progress of organic, inorganic redox flow battery and mechanism of electrode reaction. *Nano Research Energy*, 2(4), 1-40. Article e9120081. <https://doi.org/10.26599/NRE.2023.9120081>

This material is protected by copyright and other intellectual property rights, and duplication or sale of all or part of any of the repository collections is not permitted, except that material may be duplicated by you for your research use or educational purposes in electronic or print form. You must obtain permission for any other use. Electronic or print copies may not be offered, whether for sale or otherwise to anyone who is not an authorised user.



Progress of organic, inorganic redox flow battery and mechanism of electrode reaction

Yinping Liu^{1,§}, Yingchun Niu^{1,§}, Xiangcheng Ouyang^{1,§}, Chao Guo¹, Peiyu Han¹, Ruichen Zhou¹, Ali Heydari¹, Yang Zhou¹, Olli Ikkala², Glazkov Artem Tigranovich³, Chunming Xu¹, and Quan Xu¹ (✉)

¹ State Key Laboratory of Heavy Oil Processing, Beijing Key Laboratory of Biogas Upgrading Utilization, China University of Petroleum (Beijing), Beijing 102249, China

² Center of Excellence Molecular Engineering of Biosynthetic Hybrid Materials Research, Aalto University and VTT, Espoo FI-00076, Finland

³ EMCPDS Department, Mendeleev University of Chemical Technology of Russia, Moscow 125047, Russia

[§] Yinping Liu, Yingchun Niu, and Xiangcheng Ouyang contributed equally to this work.

Received: 7 March 2023 / Revised: 1 April 2023 / Accepted: 30 April 2023

ABSTRACT

With the deployment of renewable energy and the increasing demand for power grid modernization, redox flow battery has attracted a lot of research interest in recent years. Among the available energy storage technologies, the redox flow battery is considered the most promising candidate battery due to its unlimited capacity, design flexibility, and safety. In this review, we summarize the latest progress and improvement strategies of common inorganic redox flow batteries, such as vanadium redox flow batteries, iron-chromium redox flow batteries, and zinc-based redox flow batteries, including electrolyte, membrane, electrode, structure design, etc. In addition, we introduce the latest progress in aqueous and non-aqueous organic redox flow batteries. We also focus on the modification mechanism, optimization design, improvement strategy, and modeling method of the redox flow battery reaction. Finally, this review presents a brief summary, challenges, and perspectives of the redox flow battery.

KEYWORDS

inorganic redox flow batteries, organic redox flow batteries, electrode modification mechanism, novel flow batteries, challenges and perspective

1 Introduction

With the attention to energy shortage and environmental problems, renewable energy such as hydropower, wind, and solar has attracted more and more attention [1, 2]. It is predicted that by 2050, renewable energy will become the primary energy, with an average annual growth rate of 3.6%, of which solar and wind energies account for 70% of the total output of renewable energy [3]. However, the volatility and intermittency of electricity generated by these renewable energy sources make them challenging for practical applications. Electric energy storage is a powerful tool to improve the grid-connection flexibility of renewable energy, improve the reliability of the power grid, increase the utilization rate of renewable resources, extend the service life of infrastructure, and improve power quality [4].

The battery can store the electric energy generated by renewable energy in the form of chemical energy and convert the chemical energy into the required electric energy. Therefore, battery technology can accelerate the utilization of renewable energy. The capacity or energy of the redox flow batteries (RFBs) can be independently designed [4], and the power range of the RFBs is

from 100 kW to 100 MW; the energy range is from 100 kW-h to 100 MW-h. Therefore, RFBs have the advantages of inherent security, easy expansion, moderate cost, flexible operation, etc., and are considered to be promising large-scale storage technology [5, 6]. The basic components of the RFBs include electrodes, bipolar plates, membranes, and two external tanks [7]. In the RFBs, the cathode and anode materials are made from an electrolyte solution in which energy is stored. The electrolyte on the anode and cathode sides is pumped into porous electrodes on both sides of the stack, where ion exchange membranes or porous separators separate these electrodes to prevent mixing. Electrochemical redox reactions of the batteries take place at the electrode surface [4, 8]. As a common evaluation indicator for RFBs, it mainly includes energy efficiency (EE), capacity decay rate, current density, and Coulomb efficiency (CE), which is of great significance for understanding the performance and long-term operational stability of batteries [9].

As a representative flow battery, vanadium RFBs (VRFBs) [10, 11] have been considered one of the most mature technologies for a long time and are currently in the commercial demonstration

© The Author(s) 2023. Published by Tsinghua University Press. The articles published in this open access journal are distributed under the terms of the Creative Commons Attribution 4.0 International License (<http://creativecommons.org/licenses/by/4.0/>), which permits use, distribution and reproduction in any medium, provided the original work is properly cited.

Address correspondence to Quan Xu, xuquan@cup.edu.cn

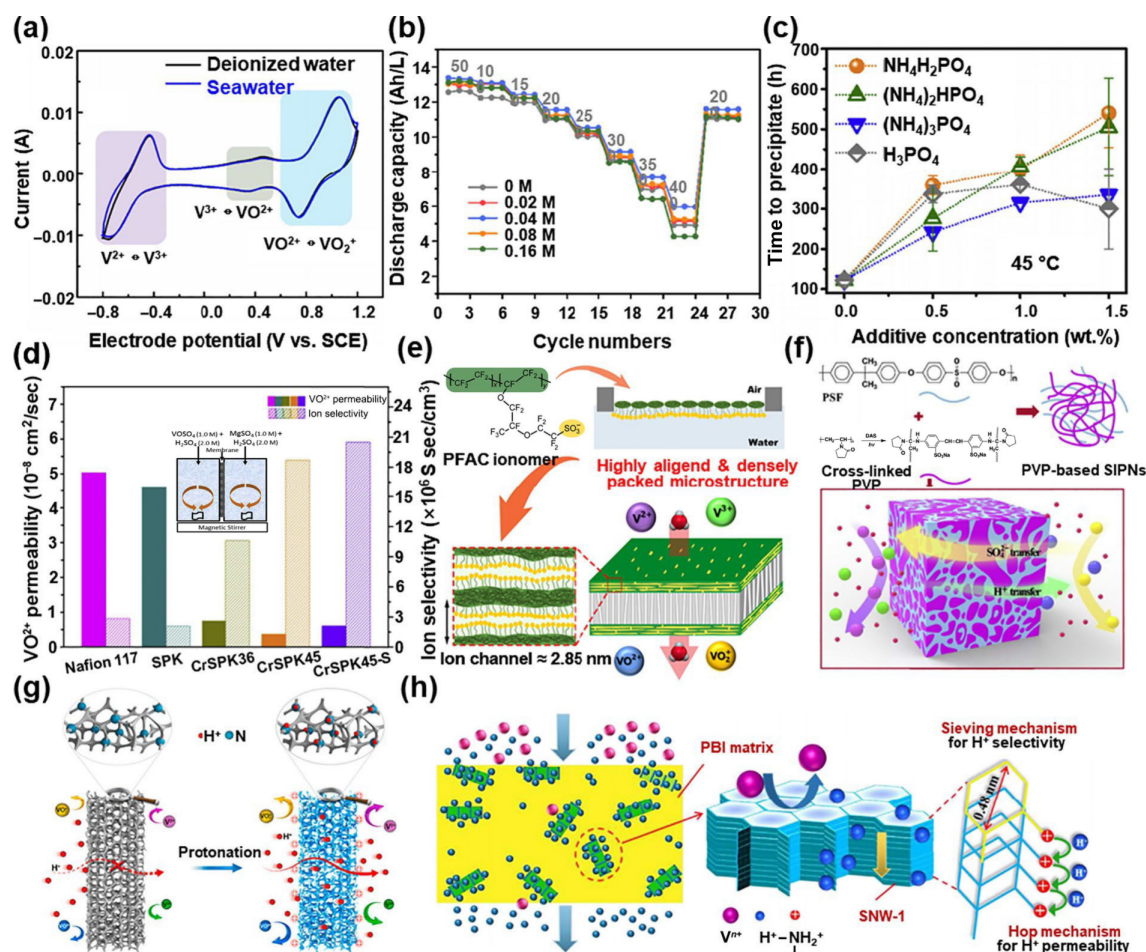


Figure 2 (a) Cyclic voltammograms of electrolytes prepared from seawater and deionized water. Reproduced with permission from Ref. [31], © Elsevier B.V. 2019. (b) Discharge capacity performance of electrolytes prepared with different Cl⁻ concentrations. Reproduced with permission from Ref. [32], © Elsevier Ltd. 2021. (c) Effects of four different additives on the thermal stability of electrolytes at 45 °C. Reproduced with permission from Ref. [29], © Elsevier B.V. 2018. (d) Comparison of several membranes' VO₂⁺ permeability and selectivity. Reproduced with permission from Ref. [41], © Elsevier B.V. 2019. (e) Preparation mechanism diagram of ultrathin PFSA membrane. Reproduced with permission from Ref. [38], © American Chemical Society 2020. (f) Schematic diagram of PVP-based SIPNs composition. Reproduced with permission from Ref. [39], © Elsevier B.V. 2016. (g) Schematic diagram of microporous skeleton transport of TB membrane after protonation. Reproduced with permission from Ref. [42], © Elsevier B.V. 2020. (h) The PBI/SNW membrane transport mechanism. Reproduced with permission from Ref. [45], © Elsevier B.V. 2020.

performance [32]. After adding 0.02 M Cl⁻ into the electrolyte, due to the catalytic effect of chloride ions on the VO²⁺/VO₂⁺ redox reaction, the peak voltage resolution of cyclic voltammetry (CV) measurement decreased from 132 to 106 mV, and the peak current increased by 3.5 mA. Moreover, the impedance value of electrolytes containing the Cl⁻ additive was lower, which also verified the catalytic effect of the Cl⁻ ion on vanadium reaction kinetics. As shown in Fig. 2(b), the electrochemical measurement results showed that with the increase of Cl⁻ content, the discharge capacity of the VFB was higher than that of the original battery. When the optimal Cl⁻ concentration was 0.04 M, the battery achieved the high EE of 82.5% at 200 mA/cm², and the capacity retention rate after 100 cycles was 83.1%, much higher than that of the battery without additives (71.3%).

Phosphoric acid is usually used for heat-stable vanadium electrolytes, but the vanadium electrolyte supported by phosphoric acid and H₂SO₄ is easy to self-precipitate to form VOPO₄, which has poor stability. Nguyen et al. discussed the synergistic effect of ammonium ions and phosphate ions [29]. At 45 °C, all ammonium phosphate compounds showed relatively high effectiveness in preventing the formation of VOPO₄ and improving the stability of the electrolyte (Fig. 2(c)). The thermal

stability effects of the tested ammonium and phosphorus (P)-containing compounds are as follows: NH₄H₂PO₄ > (NH₄)₂HPO₄ > H₃PO₄ > (NH₄)₃PO₄.

Additives are added to the electrolyte to enhance the stability and performance of VFBs over a wide temperature range. Li et al. mixed vanadium sulfate with chloride, leading to a stable mixed electrolyte over a much broader temperature window of -5–50 °C than that of 10–40 °C [8]. Nuclear magnetic resonance (NMR) studies and quantum calculations were conducted to demonstrate the formation of stable VO₂Cl(H₂O)₂ at high temperatures and the reduction in SO₄²⁻ concentration, which might be the key to the improvement of the battery. Mousa et al. found that ammonium and phosphate ions acted as precipitation-inhibiting additives in the negative electrolyte of VFBs, which could help reduce the lower temperature limit from 10 to 5 °C [33]. They believed that the added ions should be absorbed on the nucleation sites, resulting in the inhibition of vanadium crystal growth at low temperatures and the extension of the induction time for precipitation.

Further studies have been conducted on the electrolyte additives in order to design high-power and stable VFBs for extreme weather conditions. Lu et al. reported a multi-electron

heteropoly acid negolyte $H_6P_2W_{18}O_{62}$ (HPOM), which exhibited a low freezing point and high conductivity resulting from its high solubility and Grotthuss proton-conduction mechanism [34]. VFBs that contain 0.5 M HPOM in the electrolyte showed high stability and superior electrochemical performance at $-20\text{ }^\circ\text{C}$ with a negative electrolyte capacity of 79.6 Ah/L and a power density of 282.4 mW/cm^2 over 800 cycles at 160 mA/cm^2 . Their work plays an important role in the design of VFBs for extreme weather conditions.

2.1.2 Membranes

For the ionic membrane of VFBs, low permeability of vanadium ions, high proton conductivity, and good stability are indicators to evaluate the applicability of the membrane in VFB application [35]. The membranes in the VFBs system mainly include ion exchange membranes and non-ion exchange membranes. Ion exchange membranes include cation exchange membrane (CEM), anion exchange membrane (AEM), and zwitterion exchange membrane (AIEM), depending on the ionic functional groups on the membrane. The perfluoro membrane is the most commonly used ion exchange membrane in VFB, with its high proton conductivity and excellent chemical stability [36, 37]. Next, we introduce the latest progress of VFB membranes.

Commercial perfluoropolymer ion exchange membranes (Nafion) are most widely used due to their high ion conductivity and stability in acidic and oxidizing electrolyte solutions of VFB. Commercial perfluorinated sulfonic acid (PFSA) has a high vanadium ion cross degree and poor circulation capacity. Kim et al. developed an ultrathin molecular controlled PFSA membrane with highly aligned ion channels through molecular alignment at the air/water interface (Fig. 2(e)) [38]. The ultrathin PFSA membrane had 3000 times fewer ionomers than the conventional Nafion 115 membrane and had a lower cost. And the ion selectivity of the ultrathin PFSA membrane was 500 times higher than traditional PFSA membrane. Moreover, the RFB assembled with ultrathin PFSA membrane had high stability. The EE under 800 long-term cycles was 78%, which was higher than that of the RFB assembled with the Nafion membrane of similar thickness (70%).

Due to the application of the perfluorinated membrane, VFB has a high cost and severe vanadium ions migration. Zeng et al. fabricated semi-interpenetrating polymer networks (SIPNs) composed of crosslinked polyvinylpyrrolidone (PVP) and polysulfone (PSF) [39]. As shown in Fig. 2(f), PVP is a hydrophilic polymer, and PSF is a hydrophobic polymer. The crosslinked polymer could hinder the crosslinking of vanadium ions, and the pyrrolidone segment in PVP can be protonated by H_2SO_4 . There should be a Donnan repulsion between vanadium ions and protonated pyrrolidone segment, which could greatly reduce the permeability of vanadium ions. Moreover, the open-circuit voltages (OCV) time of the VFB (170 h) added with SIPNs-60 was much longer than that of the VFB using the N212 membrane (50.6 h). And PVP-based SIPNs had excellent cycle stability and were suitable for RFBs membrane.

Sulfonated poly(ether ether ketone) (SPK) membrane has attracted more attention because of its low cost, high stability, and simple manufacture [40]. Bhushan et al. achieved effective crosslinking of SPK through sulfonamide bonding, avoiding deterioration of functional group concentration on the membrane matrix due to crosslinking [41]. From the comparison of the ion selectivity and VO^{2+} permeability of five different membranes (Fig. 2(d)), it can be seen that the unmodified SPK membrane was

highly expanded in H_2SO_4 aqueous solution. The VO^{2+} permeability of the Nafion 117 membrane ($503 \times 10^{-10}\text{ cm}^2/\text{s}$) was about 8 times higher than the CrSPK45-S membrane ($61 \times 10^{-10}\text{ cm}^2/\text{s}$), indicating CrSPK45-S was more suitable for the VFBs. Moreover, the VFB assembled with the CrSPK45-S membrane had higher EE (85%) and CE (98%) values. Under the same conditions, the self-discharge time (1850 min) of the CrSPK45-S membrane was significantly higher than that of the Nafion 117 membrane (990 min) and original SPK membrane (1340 min), so the battery had a longer cycle life.

The high activity of active substances and the unwillingness to mix positive and negative electrode electrolytes make low-cost microporous membranes a more promising alternative for the successful commercial application of VFB. The difference in membrane conductivity due to factors such as thickness, pore size, and porosity has become the main challenge for their low voltage efficiency at high current densities. Zhou et al. proposed a highly conductive and vanadium-sieved microporous membrane from a shape-durable Tröger's based polymer (TB membrane) [42]. TB has been compounded with dimethyldiphenylmethane (DMDPM-TB) and dimethylbiphenyl (DMBP-TB). The prepared polymers had regularly arranged bridged bicyclic diamines, which were easily protonated in acidic solutions, making the polymer skeleton hydrophilic, thus promoting proton exchange (Fig. 2(g)). The composite membrane can achieve high vanadium ion selectivity and proton permeability. The assembled vanadium flow battery had high output power and long cycle life.

The covalent organic framework (COF) has a high surface area and good chemical and thermal stability [43, 44]. And it has great flexibility, which provides opportunities for designing and adjusting the pore size, porosity, conductivity, and other characteristics of the membrane. And through the organic ligand structure of COFs materials, functional groups can be easily introduced, which makes them widely used in electrochemical energy storage. Di et al. first designed a membrane based on the covalent organic framework for VFB [45]. The presence of micropores and amino groups in the covalent organic framework led to low area impedance ($0.46\text{ }\Omega\text{-cm}^2$). The membrane without ion exchange groups had good chemical stability. Figure 2(h) shows the proton transfer mechanism of the covalent organic framework membrane. The pore channel formed by Schiff base networks-type COF (SNW-1) could allow the hydrated protons in solution to pass through while blocking vanadium ions. The tertiary amine group on the wall of SNW-1 could be protonated in an acidic environment and might act as a proton acceptor to transfer protons. Polybenzimidazole (PBI)/SNW-1 membrane-assembled VFBs had high CE and EE, good proton permeability, and selectivity.

2.1.3 Electrodes

Among the components of VFBs, VO^{2+}/VO_2^+ (cathode) and V^{2+}/V^{3+} (anode) redox couples are essential components of the VFB system, which mainly occur on the surface of the electrodes [46]. Therefore, the electrodes are the main factor limiting the performance of VFB. Graphite felt (GF), carbon felt (CF), carbon cloth (CC), and other carbon-based electrode materials have the advantages of low cost, high stability and conductivity, corrosion resistance, and so on [5, 47, 48]. Various strategies, including heat treatment, acid activation, chemical etching, and polymer modification, have been successfully used to improve the wettability and activity of electrodes [26, 48, 49].

Graphene material has excellent conductivity and a large

specific surface area, and is inert to the strong acid electrolyte, so it has a promising prospect on the electrode in VFB [50]. Li et al. used *in situ* chemical vapor deposition to grow a uniform and dense three-dimensional (3D) graphene layer on CF (Fig. 3(a)) [51]. With the deposition of graphene, the specific surface area of the electrode increased significantly. In addition, the peak current of the graphene nanowall-modified CF (CF-G) electrode was about 3–4 times that of the pristine CF electrode, indicating that the catalytic activity of the CF-G electrode was much higher than that of the original electrode. Moreover, compared with the pristine CF electrode, the reaction rate of the CF-G electrode to the $\text{VO}_2^+/\text{VO}_2^{2+}$ redox couple was increased by three times, and the EE of the battery was increased by 11%.

Unlike the traditional multi-step process of growing nanostructures on CF, Abbas et al. proposed a new method to improve CF [26]. This method only needs thermal treatment of the felt loaded with the catalyst in the air to generate well-arranged nanorods on the CF surface. The nanorods were part of the CF and did not involve any external carbon source, which was simple and economical. Compared with the pristine CF, the surface wettability of the CF catalytically etched by Co_3O_4 was better, showing a better electrochemically active surface area, reducing

the overpotential of the redox reaction, and improving the overall performance.

The heteroatom-doped electrode has good stability and low cost and can be modified while preserving the morphology of the electrode. Huang et al. developed P and fluorine (F) co-doped GF (PF-GF) electrodes by dipping and high-temperature carbonization (Fig. 3(b)) [52]. Compared with the pristine GF, P and F co-doping increased the number of defects and oxygen-containing functional groups in the GF, thus promoting more active sites. And the PF-GF electrode with high reversibility accelerated the kinetics of $\text{VO}_2^+/\text{VO}_2^{2+}$ and $\text{V}^{2+}/\text{V}^{3+}$ redox reaction. Moreover, the PF-GF electrode had good cycle stability, and no morphological changes were observed on the electrode surface in 1000 cycles.

Mn_3O_4 and MnO_2 are intensively researched for their low cost, attractive catalytic activity, and environmental friendliness. Ma et al. synthesized GF/ MnO_2 (GF-MNO) composite electrodes by one-step hydrothermal method [53]. Since the nucleation and growth of MnO_2 particles are sensitive to pH, they have been uniformly loaded on the GF electrodes at low pH (Fig. 3(c)). MnO_2 particles can increase the absorption sites and reduce the polarization potential of the redox reaction of vanadium ions. At the current

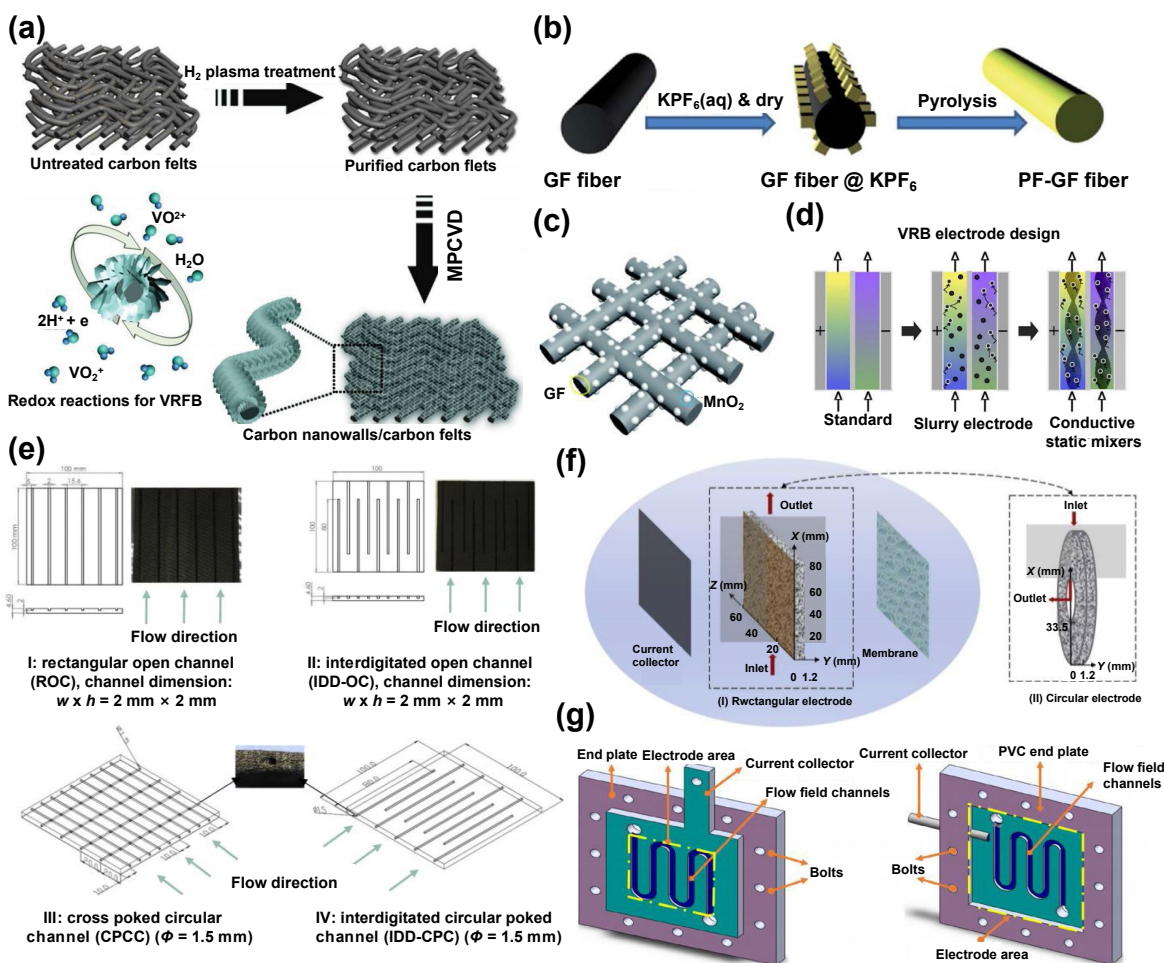


Figure 3 (a) Fabrication process and design mechanism of the CF-G electrode. Reproduced with permission from Ref. [51], © The Author(s) 2015. (b) An explanatory diagram of the PF-GF electrode preparation process. Reproduced with permission from Ref. [52], © The Royal Society of Chemistry 2018. (c) Schematic diagram of MnO_2 nanoparticles uniformly attached to the surface of GF. Reproduced with permission from Ref. [53], © Science China Press and Springer-Verlag GmbH Germany 2018. (d) Schematic diagram of slurry electrode used in VFB. Reproduced with permission from Ref. [55], © Elsevier B.V. 2018. (e) Schematic diagram of four channel designs on porous electrodes. Reproduced with permission from Ref. [57], © Elsevier B.V. 2016. (f) VFB with the rectangular electrode and circular electrode, respectively. Reproduced with permission from Ref. [56], © Elsevier B.V. 2014. (g) Schematic diagram of electrode area structure of traditional and new design batteries. Reproduced with permission from Ref. [58], © Elsevier Ltd. 2018.

density of 150 mA/cm², the EE and discharge capacity of VFBS assembled with GF-MNO electrodes were increased by 12.5% and 40%, respectively, compared with those assembled with original GF electrodes.

Slurry electrodes are a dispersion of conductive particles in liquid electrolytes. It has the advantage of easy production and can be recycled and filtered without disassembling the battery [54]. Percin et al. dispersed activated carbon and graphite powder particles into vanadium electrolytes [55]. They introduced 3D printing conductive static mixer to improve charge transfer by strengthening slurry mixing and increasing surface area (Fig. 3(d)). The cyclic charge and discharge experiments showed that CE was 95% and EE was 65% when a static mixer was used.

The gel polymer interface can effectively prevent vanadium ions from passing through the membrane of the battery. Lim et al. modified graphite carbon electrodes (GCFs) by immersing polyethyleneimine (PEI) with amino and carboxyl groups to form spider-like PEIAA-GCF polymer electrodes [49]. Compared with the original electrode, the polymer electrode had better surface wettability, and the contact angle was reduced from 112° to 45°, thus reducing the charge transfer resistance. Compared with the GCFs, the capacity retention of the PEIAA-GCF polymer-modified electrode has been greatly increased from 17.65% to 86.46%, which was due to the remarkable blocking effect of the modified electrode in preventing the cross of active vanadium species.

2.1.4 Cell structure

One of the main problems in the performance of restricted RFBs is the decrease of charge–discharge capacity due to inadequate electrolyte reaction. The cell structure design can increase the reaction area of the electrolyte, which can reduce this phenomenon [56]. Using a suitable channel can improve the flow distribution in the electrode and reduce the flow resistance, thus reducing the pump's energy consumption [57]. Next, we will introduce several battery design and flow channel improvement strategies.

Bhattarai et al. studied four kinds of electrodes with channels, including rectangular open channel (ROC), interdigitated open channel (IDD-OC), interdigitated circular poked channel (IDD-CPC), and cross-poked circular channel (CPCC). They compared the electrodes with four design channels with those without channels (Fig. 3(e)) [57]. The results showed that at all current densities tested, the IDD-OC and IDD-CPC had better EE and voltage efficiency (VE) because of more uniform electrolyte flow distribution and higher reaction surface utilization. The ROC had poor efficiency due to a lack of electrolytes. Using IDD-OC and IDD-CPC could prove that the overall EE is improved by 2.7% and 2.5%, respectively.

Zheng et al. proposed a new type of circular VFB for the first time to improve the quality transportation of traditional rectangular VFB (Fig. 3(f)) [56]. Comparing the polarization curve and electrochemical impedance spectroscopy (EIS) showed that the circular VFB could improve mass transport and reduce concentration polarization. Better battery performance can be achieved by optimizing internal and external diameters and flow paths. And trapezoidal or fan-shaped structures would be also expected to exhibit excellent performance.

Al-Yasiri et al. designed a new battery structure to eliminate end plates and gaskets, improve safety, and extend service life, including embedding serpentine flow channels without holes and brittleness [58]. And the traditional graphite plate has been

replaced by the thermoplastic material polyvinyl chloride (PVC) to avoid electrolyte leakage between the assembled components (Fig. 3(g)). The polarization test shows that the electrochemical surface area in the new battery structure was more extensive, and there was more power under the same external size. And the electrolyte entering both sides had a higher supply rate so that the output capacity of the battery increased.

2.1.5 Commercialization progress

The application research on VFB is mainly focused on the field of energy storage. Foreign Research & Development institutions have invested a lot of money to conduct decades of in-depth research and have successively built KW-MW-class VFBS energy storage systems in Thailand, Japan, the USA, South Africa, and other places for peak regulation of power stations and power supply to remote areas. At present, a number of effective Research & Development and application institutions at home and abroad are conducting VFB research and development and have entered the commercialization stage [59].

Before 2018, due to the relatively high cost of flow batteries and the weak demand for energy storage technology, the VFB energy storage power station scale was mainly from 100 kW to MW. The largest power station was the 15 MW/60 MW-h energy storage power station provided by Sumitomo Electrician for Hokkaido Electric Power Company. In recent years, with the development of the energy storage market at home and abroad and the decline of vanadium prices, many VFBS demonstration projects have been built worldwide.

In 2021, vanadium producer Bushveld Minerals announced the construction of an annual production capacity in South Africa of 200 MW-h vanadium electrolyte production plant. On March 30, 2022, Invinity signed a contract to manufacture a VFB system in Wujiang District, Suzhou Mesh. Sumitomo Electric signed a contract with Hokkaido Electric Power Industries to build a 17 MW/51 MW-h VFB energy storage power in 2022 stations. These will accelerate the application and promotion of the VFBS energy storage demonstration project [60].

In China, VFB has been applied in smart grids, communication base stations, power supply in remote areas, renewable energy, peak-shifting, and valley-filling projects. Take Beijing Puneng as an example, its current VFBS energy storage applications cover kilowatt to megawatt systems. The kilowatt-level system is mainly composed of a 20/40 MW-h energy storage system, mainly used in laboratory energy storage, communication base station power supply, etc.

The megawatt level system mainly comprises multiple 250 kW standard modules and covers the reactor structure, liquid storage tank, electronic equipment, control device, air conditioning system, etc., which is mainly used in power grid energy storage, peak shifting, valley filling, and other projects.

At present, Wuhan Nanrui (Fig. 4(a)) has fully mastered the VFB modification selection technology and has the ability for vanadium battery body design, material development, and system integration. It has successfully developed a high-power vanadium battery stack and 250 kW/500 kW-h energy storage system [61], applied for 70 invention and utility model patents and authorized more than 40 patents.

Weili Energy is one of the emerging energy storage battery enterprises in China. Its photovoltaic VFB energy storage power station and the first phase of the 7.5 MW/22.5 MW-h optical storage demonstration project in Awati County, Xinjiang province, successfully connected to the grid in December 2020 (Figs. 4(b) and 4(c)) [62].

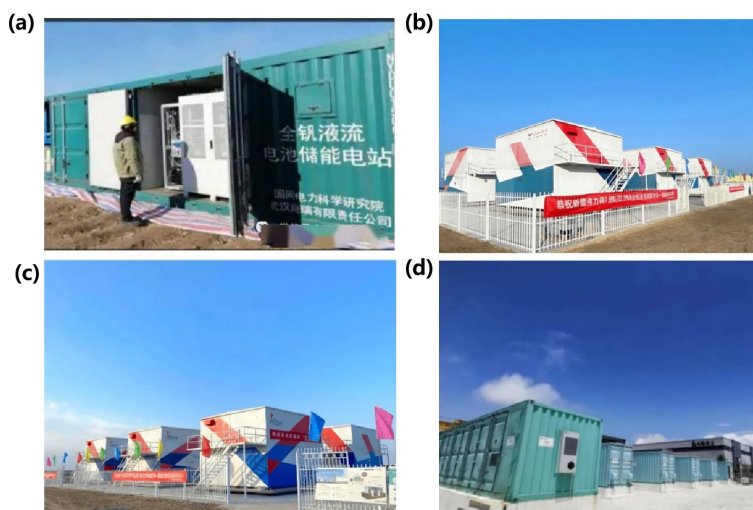


Figure 4 (a) Wuhan Nanrui VFBs energy storage system [61]. (b) and (c) Weilide Xinjiang Awati VFBs energy storage power station [62]. (d) Shantou Smart Energy RFBs Energy Storage [63].

The VFBs energy storage projects, such as Yellow River Upstream Hydropower Company and Changde 10 kW/60 kW-h flow energy storage system designed and developed by Shanghai Electric Energy Storage Company, are already in the project delivery and acceptance stage and are about to be connected to the grid.

Shantou Smart Energy RFB Energy Storage project 1 MW/1 MW-h VFBs energy storage power station (Fig. 4(d)) has successfully passed the acceptance inspection in 2021 [63].

According to the half-annual report of Shanghai Electric in 2021, Shanghai Electric added orders for energy storage equipment of RMB 2.88 billion, up 145.0% year on year; the company placed orders for manual energy storage equipment of RMB 3.08 billion.

In 2022, the 100-megawatt-level flow battery energy storage peak shaving power station provided by the team of Li Xianfeng, a researcher at the Energy Storage Technology Research Department of the Dalian Institute of Chemical Physics, Chinese Academy of Sciences, was officially connected to the grid for power generation. The project size is 100 MW/400 MW-h. The main function of this technology is to provide auxiliary services such as peak shaving and frequency regulation for the power grid, alleviate the stability problems caused by large-scale renewable energy integration to a certain extent, promote the consumption of renewable energy power generation in the power system, and improve the operation economy of the power system.

2.1.6 Brief conclusion

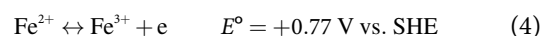
VFBs have a wide range of applications, flexible design concepts, good charge-discharge performance, high capacity, high energy efficiency, and long life. Recently, the electrolyte, electrode, membrane, and structure design of VFBs have been extensively studied (Table 1). And many domestic and foreign enterprises are also actively engaged in the research and development of VFBs. VFBs have entered the stage of commercialization.

2.2 ICRFB

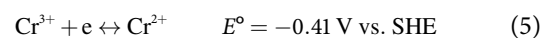
ICRFBs also consist of two half-cells separated by an ion exchange membrane. An external storage tank provides half the battery, and its size determines the capacity of the system [64]. ICRFBs have a flexible design, high security, long service life, and low maintenance cost [65]. The redox couples of its cathode electrolyte

and anode electrolyte are $\text{Fe}^{2+}/\text{Fe}^{3+}$ and $\text{Cr}^{3+}/\text{Cr}^{2+}$, respectively. Iron and chromium are abundant and cheap, so ICRFBs are very suitable for large-scale energy storage [66]. The positive and negative reactions of the ICRFBs are shown as Eqs. (4)–(6) [67]

Positive electrode:



Negative electrode:



Overall reaction:



Next, we will introduce the latest progress in the electrolyte, membrane, electrode, and battery structure of ICRFBs.

2.2.1 Electrolytes

Initially, the cathode and anode electrolytes of ICRFBs were $\text{Fe}^{2+}/\text{Fe}^{3+}$ and $\text{Cr}^{3+}/\text{Cr}^{2+}$ in hydrochloric acid (HCl) solution redox couples, respectively [66]. However, the isomerization of Cr^{3+} complex ions will degrade the performance of ICRFBs continuously [68]. To solve this problem, the National Aeronautics and Space Administration (NASA) proposed an electrolyte that uses a redox couple of $\text{Cr}^{3+}/\text{Cr}^{2+}$ and $\text{Fe}^{2+}/\text{Fe}^{3+}$ in an HCl solution as an electrolyte, which can reduce capacity decay [69]. Next, we introduce the influence of concentration change in the electrolyte [70], chelation [71], and catalyst addition [67] on the electrochemistry of ICRFBs.

Wang et al. studied the electrochemical performance of ICRFB with electrolytes containing FeCl_2 , CrCl_3 , and HCl with different molar masses [70]. The results showed that the electrolyte viscosity was proportional to the concentration of the CrCl_3 and FeCl_2 , and the conductivity of the electrolyte was inversely proportional. Both viscosity and conductivity should be proportional to the concentration of HCl. With the increase of the concentration of Fe/Cr in the electrolyte, the redox reaction peak current increased. When the concentration of Fe/Cr in the electrolyte was 0.75 M, the ratio of peak current was closest to 1 (Fig. 5(a)). The charge transfer resistance (R_{ct}) was the lowest at 3 M HCl, showing the best electrochemical performance. The cyclic properties of the electrolytes with different Fe/Cr ratios and HCl concentrations were tested. The results showed that the capacity decay rate of the

Table 1 Operational parameters and performance of VFEB in recent years

Electrolyte	Membrane	Electrode (treatment; size)	Parameters of cells: max. j (mA/cm ²)	CE (%)	VE (%)	EE (%)	Capacity decay	References
1.5 M V ³⁺ + X M H ₂ SO ₄	Nafion 115	GF; none; 25 cm ²	300	~ 97	—	77	—	[27]
1.7 M V + 3 M H ₂ SO ₄ and 0.5 M V + 3.5 M H ₂ SO ₄	Nafion 212	GF; none; 28 cm ²	250	98	81.6	80	—	[30]
1 M VOSO ₄ + 3 M H ₂ SO ₄ + seawater	Nafion 212	GF; thermal; 4.7 cm ²	200	98.5	87.5	86.2	0.15% per cycle	[31]
1 M VO ²⁺ + 1 M V ³⁺ in 3 M H ₂ SO ₄ with Cl ⁻ concentrations of 0, 0.02, 0.04, 0.08, and 0.16 M	Nafion 212	GF; thermal; 4 cm ²	400	98.3	83.9	82.5	—	[32]
1.5 M VOSO ₄ + 2.0 M H ₂ SO ₄	CrSPK45-S membrane	Carbon graphite; none; 25 cm ²	80	98	86.7	85	—	[41]
1.65 M V ³⁺ /VO ²⁺ + 3 M H ₂ SO ₄	PFSA membrane	CF; none; 4 cm ²	200	94	82	78	—	[38]
1 M V(V) + 3 M H ₂ SO ₄ in the positive side and 1 M V(III) + 3 M H ₂ SO ₄ in the negative side	SIPNs membrane	GF; thermal; 6 cm ²	100	97.6	92.2	90	0.056% per cycle	[39]
1.0 M V ²⁺ /V ³⁺ + 5.0 M H ₂ SO ₄ as the negative electrolyte, 1.0 M VO ²⁺ /VO ₂ ⁺ in 5.0 M H ₂ SO ₄ as the positive electrolyte	DMBP-TB ⁺ or DMDPM-TB ⁺ membrane	Carbon paper; thermal; 5 cm ²	150	99	80.8	80	—	[42]
1.5 M VO ²⁺ /VO ₂ ⁺ + 3.0 M H ₂ SO ₄ as the positive electrolyte, 1.5 M V ²⁺ /V ³⁺ + 3.0 M H ₂ SO ₄ as the negative electrolyte	PBI/SNW-25% membrane	CF; none; 9 cm ²	180	98.7	94.8	93.5	0.42% (80 mA/cm ²)	[45]
2.5 M VOSO ₄ + 2.5 M H ₂ SO ₄	Nafion 212	CF-G; none; 6.25 cm ²	125	—	—	~ 90	—	[51]
1.5 M V ⁴⁺ + 3.0 M H ₂ SO ₄ as the positive electrolyte, 1.5 M V ³⁺ + 3.0 M H ₂ SO ₄ as the negative electrolyte	Nafion 117	Co ₃ O ₄ -loaded CF; thermal; 25 cm ²	150	~ 97.5	~ 90	~ 87.5	—	[26]
0.75 M VOSO ₄ + 0.375 M V ₂ (SO ₄) ₃ + 3 M H ₂ SO ₄	Nafion 115	PF-GF; thermal; 4 cm ²	250	96.6	82.0	79.2	0.03% (120 mA/cm ²)	[52]
0.75 M V ₂ (SO ₄) ₃ + 0.75 M VOSO ₄ + 3 M H ₂ SO ₄	Nafion 115	GF-MNO; thermal; 4 cm ²	250	—	—	80	—	[53]
1.5 M VO ²⁺ + 3 M H ₂ SO ₄ as the positive electrolyte, 1.5 M V ³⁺ + 3 M H ₂ SO ₄ as the negative electrolyte	Nafion 115	CF; none; 48 cm ²	160	96.22	78.68	75.71	—	[56]
1.04 M VOSO ₄ ·xH ₂ O + 4 M H ₂ SO ₄	Nafion 117	GF; none; 25 cm ²	—	90.57	86.21	79.03	—	[58]

electrolytes containing 3 M HCl and the Fe/Cr ratio of 1 was low (Fig. 5(b)).

Chelation affects the redox potential of metal ions and the transfer kinetics to improve the RFBs' performance. Waters et al. reported the effect of chelation on ICRFB by preparing an electrolyte containing Fe diethylenetriaminepentaacetic acid (FeDTPA) and Cr 1,3-diaminopropanetetraacetic acid (CrPDTA) in KBI with pH = 9 [71]. As shown in Fig. 5(c), the chelated metal had a more prominent redox peak, better electrochemical reversibility, and faster current response. At the current density of 50 mA/cm², the maximum discharge power density of fully chelated ICRFBs assembled with unmodified carbon electrodes was 216 mW/cm², CE was 97%, and EE was 78%. The modified electrode-assembled ICRFB had better stability. The cycle time of 40 cycles at pH = 9.5 was 46.25 h, and the cut-off voltages of charging and discharging batteries were 2 and 0 V, respectively.

Indium and indium oxide can effectively increase the hydrogen overpotential and cycle stability of RFBs. Wang and co-workers have previously found that electrolytes containing 1 M FeCl₂, 1 M CrCl₃, and 3 M HCl have the best chemical properties. Recently, they directly added indium chloride (InCl₃) to the electrolyte of ICRFB to investigate the battery's performance [67]. The results showed that In³⁺ effectively inhibited the HER and accelerated the kinetics of Fe²⁺/Fe³⁺ and Cr³⁺/Cr²⁺ to a certain extent. As shown in Fig. 5(d), at 160 mA/cm², the ICRFB with 0.01 M In³⁺ and perfluorosulfonic-acid ion exchange membrane (IEM) was used in the anolyte and operated for 140 cycles. The discharge capacity maintained 77.1% of its initial capacity (0.16% per cycle). In

comparison, the discharge capacity of the original anolyte maintained only 40.8% of its initial capacity.

Non-aqueous RFBs (NARFBs) use organic solvents that have a wider electrochemical potential window, higher energy density, and a broader operating temperature range than RFBs. Bamgbopa et al. reported for the first time that a NA ICRFB contained chromium(III) acetylacetonate (Cr(acac)₃), iron(III) acetylacetonate (Fe(acac)₃) active species, and active substance tetraethylammonium tetrafluoroborate (TEABF₄), which would not be affected by the undesired and efficiency limited HER in the aqueous RFBs [14]. This Fe-Cr NARFB allows rapid charging up to 1.8 V above the OCV and is suitable for large-scale stationary applications.

2.2.2 Membranes

As a critical component of ICRFBs, the ionic conductive membranes prevent the intersection of cathode and anode electrolytes while conducting protons to complete the circuit [72]. For RFBs, the ideal membrane should have good mechanical stability, low cost, less cross of active substances, high ionic conductivity, and so on [14, 73]. Due to the excellent proton conductivity of perfluorinated sulfonic acid polymer electrolytes, the Nafion membranes are the most widely used membrane material in RFBs [15, 74]. Recently, some researchers have also developed newly sulfonated poly(ether ether ketone) (SPEEK) membranes, zeolite membranes [75], etc.

Sun et al. researched different thicknesses of commercial Nafion membranes (N212 (50 μm), N115 (126 μm), and N117 (178 μm))

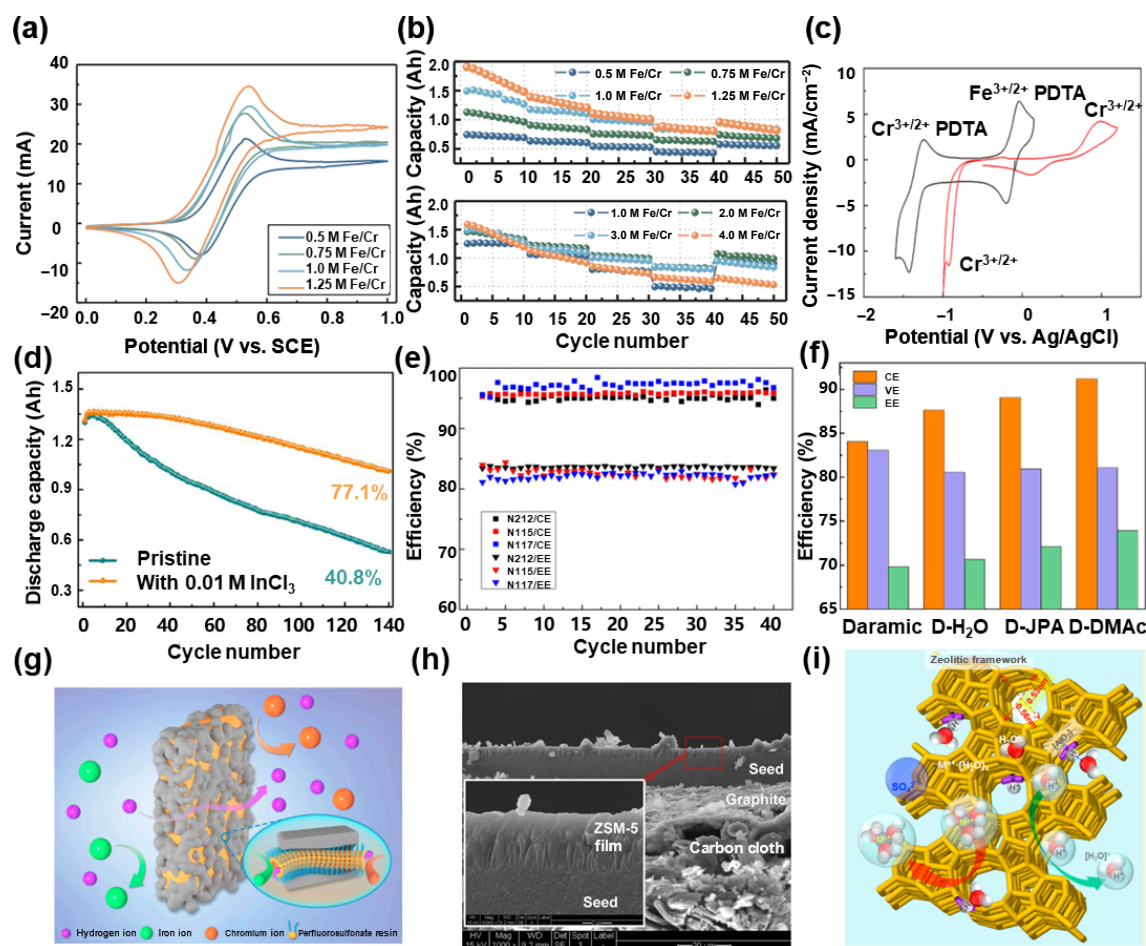


Figure 5 (a) CV curves of electrolyte at several Fe/Cr concentrations. (b) The ICRFBs capacity of electrolytes containing different HCl and Fe/Cr ratio concentrations varies with the number of cycles. Reproduced with permission from Ref. [70], © Elsevier Ltd. 2020. (c) CV of electrolyte of $\text{CrCl}_3/\text{FeCl}_2$ and electrolyte of $\text{CrPDTA}/\text{FeDTPA}$ at 100 mV/s. Reproduced with permission from Ref. [71], © American Chemical Society 2020. (d) Discharge capacity curves of ICRFB with original electrolyte and an electrolyte containing 0.01 M InCl_3 within 140 cycles. Reproduced with permission from Ref. [67], © Elsevier Ltd. 2020. (e) EE and CE curves of ICRFBs assembled with three kinds of membranes for 40 cycles at 80 mA/cm². Reproduced with permission from Ref. [72], © John Wiley & Sons, Ltd. 2019. (f) CE, VE, and EE of four different membranes assembled ICRFBs at 80 mA/cm². (g) Transmission mechanism diagram of ICRFBs composite membrane. Reproduced with permission from Ref. [79], © MDPI AG 2022. (h) Scanning electron microscopy (SEM) images of carbon cloth and ZSM-5 zeolite membrane on it. (i) Zeolite membrane framework and reaction diagram. Reproduced with permission from Ref. [75], © American Chemical Society 2016.

on the performance of ICRFBs [72]. The results showed that the thicker membrane has a relatively low permeability of electroactive substances and a high discharge capacity decay rate, so the CE of the N212 membrane was relatively lowest (Fig. 5(e)), and the discharge capacity decay rate was relatively highest. Moreover, the OCV curve showed that the discharge time of the N117 membrane was 108 h, which was much longer than that of the N212 membrane (50 h), which was because the N117 membrane was thicker and the active species cross was lower, so the charge retention time was longer. However, the internal resistance of the N212 membrane was low. When the current density was 40–120 mA/cm², considering the permeability and resistance of the membrane, the ICRFBs assembled with the N212 membrane had the highest cost-performance ratio.

Zeng et al. further studied the N211 membrane (25 μm) and the N212 membrane (50 μm) [76]. The area specific resistance (ASR) of the ICRFBs assembled with N211 membrane was 180 mΩ/cm², which was smaller than that of the ICRFBs assembled with N212 (217 mΩ/cm²). And because the Ohmic resistance of the N211 membrane was lower, it had higher VE and EE. Therefore, the N211 membrane could be more suitable for working in ICRFBs with high current density.

The high cost of the Nafion membrane is not conducive to commercial large-scale energy storage applications [77, 78]. Sun et al. successfully synthesized a low-cost SPEEK membrane [60]. Compared with the N115 membrane assembled battery, the SPEEK membrane had a lower discharge capacity decay rate, showing more stable battery performance. In addition, the cost of the SPEEK membrane was low, accounting for only 5% of the total energy storage system cost, which was far lower than the cost of using the Nafion membrane (39%).

Qiao et al. designed a Nafion dispersion (D2020) cast N,N-dimethylacetamide (DMAc) composite membrane (D-DMAC) filled with Nafion resin using a polyethylene skeleton structure [79]. The porous skeleton limited the swelling and phase separation of Nafion resin at 65 °C, which significantly improved the selectivity and stability of ions (Fig. 5(g)). Compared with the Daramic membrane, the composite membrane was prepared by the drop coating method and had smaller pores and lower permeability, thus improving ion selectivity. As shown in Fig. 5(f), the ICRFB assembled by the composite membrane was high at 91.18%, and the VE was 80.81% at 80 mA/cm².

Recently, Xu et al. showed a novel aluminum-containing zeolite membrane [75]. It is possible to achieve both extraordinary proton

transport selectivity and low ASR with the structural and chemical stability required by the RFBs. As shown in Fig. 5(h), the zeolite socony mobil #5 (ZSM-5) membranes were synthesized on a carbon cloth coated with alumina sheets and graphite nanoparticles. The ZSM-5 zeolites are structural analogs of silicalite obtained by substituting Al^{3+} for Si^{4+} . The obtained skeleton $[AlO_2]^-$ tetrahedrons make the zeolite surface hydrophilic and enhances protons' permeability, thereby improving the ionic conductivity (Fig. 5(i)).

2.2.3 Electrodes

The electrode surface is where the redox reaction of the cathode and anode occurs, so the electrodes greatly influence the performance of the battery [64]. Carbon materials are generally considered ideal electrode materials for applying ICRFBs because of their high chemical stability, long service life, and wide range of operating potential in high oxidation media. Various carbon materials, such as GF, CC, carbon paper (CP), and CF, have been studied as electrodes for ICRFBs [60, 76]. GF is a relatively commonly used electrode material in RFBs due to its reasonable cost and high porosity [66, 80]. At present, the modification of GF [81] includes thermal activation, acid treatment, metal doping, etc.

Zhang et al. described the essential differences in structure and performance as electrodes between rayon-based GF (RGF) and polyacrylonitrile-based GF (PGF) [82]. As shown in Fig. 6(b), PGF

and RGF electrodes had a rough surface in common. The difference was that PGF had typical fine rib-like gullies (Figs. 6(b)(I) and 6(b)(III)), while RGF had pits on the electrode fibers (Figs. 6(b)(II) and 6(b)(IV)). The oxygen functional groups and Bi on the electrode fiber surface can catalyze the redox reaction (Fig. 6(a)). Due to the higher graphitization degree and electrochemical activity of positive redox coupling in PGF, compared with the battery using RGF, the battery using PGF had higher VE, EE, and ASR. Because the Bi was deposited *in situ* on the negative electrode of the ICRFBs, the performance of the battery was improved. Zhang et al. further studied the effects of electrochemical polarization, Ohmic polarization, and concentration polarization of RGF and PGF [64]. Comparing RGF and PGF in ICRFBs, it can be found that PGF had lower Ohmic polarization loss and better electrocatalysis performance. The RGF surface was rough, which was convenient for mass transfer and diffusion.

Zhang and co-workers further researched the electrochemical properties of PGF and CF and whether $BiCl_3$ catalyst is added [83]. Bi^{3+} has been considered to have dual effects of inhibiting HER and catalyzing the negative electrode reaction. The oxygen functional group could catalyze the path segment, which should be beneficial to improve the performance of ICRFBs. Therefore, $BiCl_3$ in thermally activated GF would be a more promising electrode material for ICRFB applications than CF.

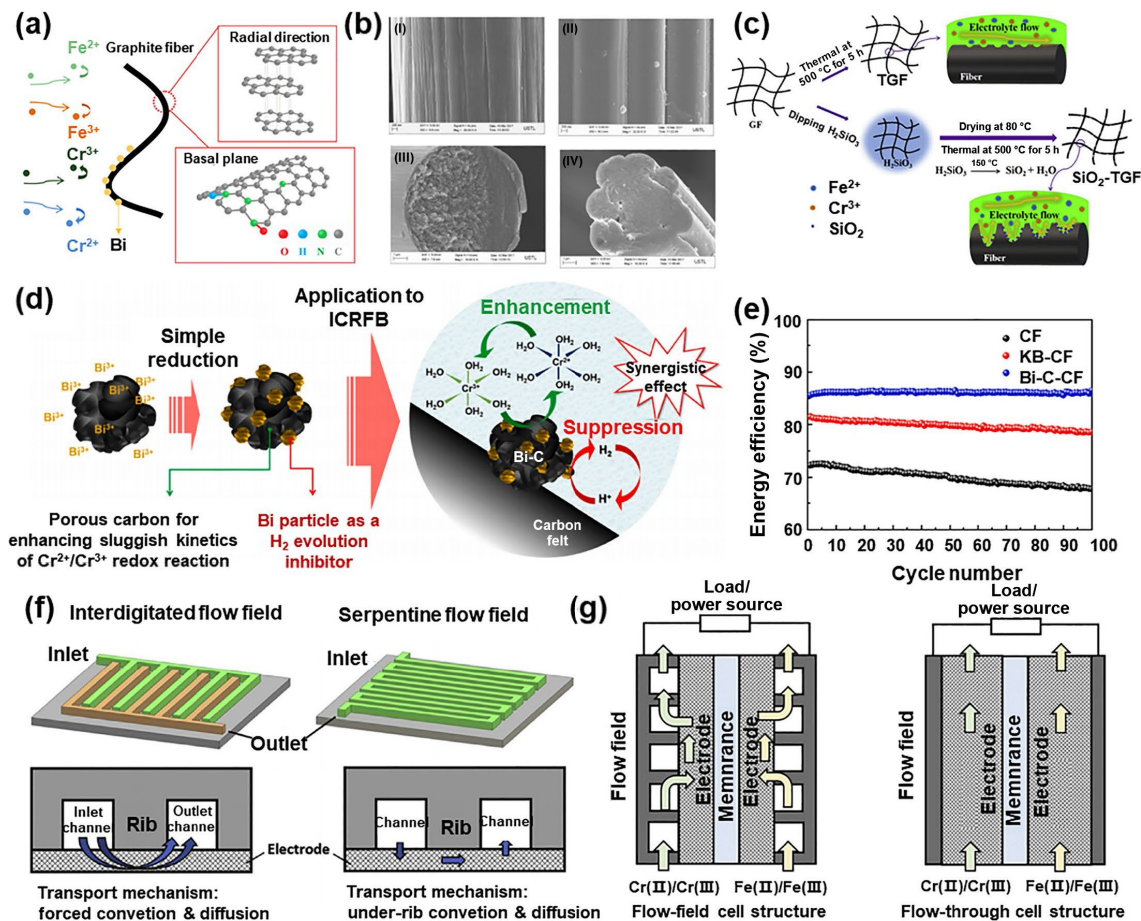


Figure 6 (a) Structural unit diagram of graphite felt. (b) PGF (I, III) and RGF (II, IV) SEM images on the surface of the electrode. Reproduced with permission from Ref. [82], © Elsevier Ltd. 2017. (c) The preparation process of silicic acid heat-treated graphite felt samples. Reproduced with permission from Ref. [84], © Elsevier Ltd. 2020. (d) Mechanism diagram of the preparation of bifunctional electrocatalyst by embedding bismuth nanoparticles in KB. (e) The EE of ICRFBs with CF, KB-CF, and Bi-C-CF in 100 cycles at 40 mA/cm^2 . Reproduced with permission from Ref. [86], © Elsevier B.V. 2020. (f) Structure diagram of IFF and SFF. Reproduced with permission from Ref. [87], © Elsevier B.V. 2016. (g) Diagram of the flow-field cell structure and flow-through cell structure. Reproduced with permission from Ref. [88], © Elsevier B.V. 2016.

Acid and heat treatment is considered the most “convenient and effective” modification method. Chen et al. researched the electrochemical performance of SiO₂-modified GF and its application in ICRFBs [84]. They impregnated GF with silicic acid and then loaded SiO₂ on the surface of GF by heat treatment (Fig. 6(c)). Because silicic acid has contained rich -OH functional groups, the GF was oxidized during heat treatment. The specific surface area and conductivity of the SiO₂ etched GF electrode increased, so the electrocatalytic performance of the electrode was improved. The VE and EE of ICRFBs assembled with SiO₂-modified GF as the electrode at the current density of 120 mA/cm² were 9.86% and 8.2% higher than the pristine electrode, respectively.

To improve the electrocatalytic performance of GF, Li et al. activated PGF by boric acid (H₃BO₃) thermal etching [85]. After H₃BO₃ thermal etching, the hydrophilicity of the graphite felt was obviously enhanced, and with the increase of H₃BO₃ concentration, the resistance value of the GF after etching showed a downward trend. A large number of round holes appeared on the surface of GF etched by H₃BO₃, increasing the specific surface area of the electrode. The specific surface area of GF etched with 25% H₃BO₃ increased by 3.6 times. The assembled ICRFBs had an EE of more than 85%, about 9.5% higher than the pristine electrode. Ahn et al. embedded bismuth nanoparticles into Ketjenblack (KB) carbon, which greatly promoted the redox electrochemical activity of Cr²⁺/Cr³⁺ and retarded the HER [86]. During charging, well-dispersed bismuth nanoparticles can form BiH_x intermediate compounds in porous carbon, delaying the reduction of H⁺. Moreover, the rich oxygen-containing functional groups of KB electrodes as active sites could enhance the oxidation–reduction reaction of Cr²⁺/Cr³⁺ (Fig. 6(d)). As shown in Fig. 6(e), the ICRFBs with Bi-C as the negative electrode achieved a high EE of 86.54% in the charge–discharge cycles at room temperature.

2.2.4 Cell structure

The design of the flow field of ICRFBs not only affects the mass transport of ions in the electrolyte but also affects the concentration distribution of ions in the electrode and the distribution of the catalyst. Thus, the active specific surface area of redox reaction in ICRFBs is affected [87].

Zeng et al. investigated the effect of flow field design on the performance of electrode surface electroplated catalysts and assembled RFBs [87]. They found that the interdigitated flow field (IFF) design can provide a higher pressure drop than the serpentine flow field (SFF) design. The convective transport of positive and negative electrolytes in the electrode has been enhanced, and the distribution of the catalyst was more uniform (Fig. 6(f)). The EE of ICRFBs with IFF was 80.7%, 8.2% higher than that of ICRFBs assembled with SFF at 320 mA/cm².

Zeng et al. developed a high-performance ICRFB with a flow-field structure [88]. As shown in Fig. 6(g), the ICRFBs traditionally adopt the flow-field structure, the electrolyte is pumped into the porous electrode by a pump, and the structure is simple to make. The energy density of ICRFBs prepared with a flow-field structure can reach 200 mA/cm² at 65 °C, and the EE was 79.6%.

2.2.5 Commercialization progress

ICRFB technology was proposed by Thaller et al. of the Lewis Research Center of NASA in 1974 [89]. Because of the low cost and good comprehensive electrochemical characteristics of the ICRFBs, they finally chose the Fe/Cr flow system as the primary

development object [90]. NASA first developed a 1 kW ICRFBs energy storage system [91]. In the later stage, they raised the operating temperature and adopted the mixed solution of Fe/Cr, thus enhancing the performance of the system.

Japan's new energy industry technology development agency cooperated with NASA to improve the electrode materials and increase the electrode area. In 1983, it launched an improved 1 kW-h ICRFBs system [92] and later launched a 10 kW-h ICRFBs system [93]. Later, Ener Vault of the USA built the world's first 250 kW/1000 kW-h ICRFBs energy storage power station in 2014 [94].

At present, the company mainly engaged in ICRFBs in China is the State Power Investment Corporation (SPIC). In November 2019, the first 31.25 kW ICRFB stack (Ronghe No.1) developed by SPIC was successfully established and stably stored and provided clean electric energy of more than 5W kW-h for the Beijing Winter Olympics area. Then, in December 2020, SPIC and Shanghai power equipment research institute CO., Ltd. completed the 250 MW/1.5 MW-h RFB light storage demonstration project (Guyuan Zhanshigou photovoltaic power station). The system consists of 8 sets of 31.25 kW ICRFB stacks, with a 6-h energy storage time (1.5 MW-h), which can effectively improve the energy utilization rate of the photovoltaic power station [95, 96].

While researchers are actively researching and developing new generation ICRFBs technology, many companies are also constructing demonstration projects. The new generation of ICRFB technology will further improve the current density, reduce costs, and have better market competitiveness. The subsequent large-scale commercial application and promotion will certainly bring new technological innovations and breakthroughs for energy storage. It will also vigorously promote the application and further development of energy storage technology [95].

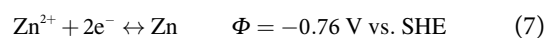
2.2.6 Brief conclusion

ICRFBs have the advantages of low cost, low toxicity and corrosivity, high safety, and good stability. In recent years, the electrolyte, electrode, membrane, and structure design of ICRFBs have been extensively studied (Table 2). Many companies are also constructing ICRFB projects to promote the application of ICRFBs in large-scale energy storage technology.

2.3 Zinc-based redox flow battery (ZRFB)

Since the zinc-based flow battery was first proposed in the 1970s, it has been developed through coupling with different positive reactions, and various ZRFB has been proposed and developed [97]. With the advantages of low price, high safety, environmental friendliness, and high energy density, it is considered one of the most promising large-scale energy storage technologies. Existing zinc-based RFBs rely on the electrodeposition of zinc in the flowing electrolyte as the negative electrode reaction, which is coupled with different positive active substances [19]. At present, the cycle life of a ZRFB is short, mainly because the stripping and electroplating reaction between zinc and zinc ions will occur during the charge–discharge process of the battery. Dendrites are easily formed during zinc deposition and dissolution, and dendrites will pierce the separator, seriously affecting the normal charge and discharge of the battery [98].

In acid media, the reaction is Eq. (7)



In an alkaline solution, zinc will react with hydroxide, so that the electrode reaction can be written as Eq. (8)

Table 2 Operational parameters and performance of ICRFBs in recent years

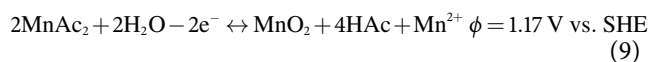
Electrolyte	Membrane	Electrode (treatment; size)	Parameters of cells: max. j (mA/cm ²)	CE (%)	VE (%)	EE (%)	Capacity decay	References
1 M FeCl ₂ + 1 M CrCl ₃ + 3 M HCl (65 °C)	IEM (60 μm)	GF; none; 50 cm ²	200	97.4	83.7	81.5	—	[70]
1 M FeCl ₂ + 1 M CrCl ₃ + 3 M HCl + 0.008 M Bi ³⁺ (40 °C)	Nafion 212	CP; thermal; 5 cm ²	—	97	80.4	78	—	[71]
1 M FeCl ₂ + 1 M CrCl ₃ + 3 M HCl + 0.01 M In ³⁺ (65 °C)	IEM (60 μm)	GF; none; 50 cm ²	200	98.5	78.2	77	0.16% (160 mA/cm ²)	[67]
0.1 M Fe(acac) ₃ + 0.1 M Cr(acac) ₃ + 0.4 M TEABF ₄	Nafion/SiO ₂	CP; HNO ₃ ; 10 cm ²	—	99	53.5	53	—	[14]
1 M FeCl ₂ + 1 M CrCl ₃ + 3 M HCl (65 °C)	Nafion 212 Nafion 115 Nafion 117	GF; thermal; 9 cm ²	120	95.03; 95.74; 97.18	87.95; 86.14; 84.46	83.58; 82.47; 82.08	1.40%; 1.25%; 1.02% (120 mA/cm ²)	[72]
1 M FeCl ₂ + 1 M CrCl ₃ + 3 M HCl + 5 Mm Bi ³⁺ (65 °C)	Nafion 211	CC; thermal; 4 cm ²	480	97.6	82.5	80.5	—	
1 M FeCl ₂ + 1 M CrCl ₃ + 3 M HCl (65 °C)	Nafion 115; SPEEK	GF; thermal; 9 cm ²	80	96.0; 98.5	85.7; 80.3	82.3; 79.1	1.49%; 1.03% (80 mA/cm ²)	
1 M FeCl ₂ + 1 M CrCl ₃ + 3 M HCl (65 °C)	D-DMAc membrane	CF; none	80	93.29	80.81	75.39	—	[79]
1 M CrCl ₃ + 2 M HCl for anolyte, 1 M FeCl ₂ + 2 M HCl for catholyte	ZSM-5 membrane	CF; none	120	~ 99	~ 86.7	85.8	—	[75]
0.47 M CrCl ₃ + 0.35 M FeCl ₂ + 2 M HCl for positive, 0.47 M CrCl ₃ + 0.35 M FeCl ₂ + 2 M HCl with 1 M BiCl ₃ for catholyte (65 °C)	Nafion 115	RGF; PGF; none; 49 cm ²	60	96.84; 94.87	72.70; 80.63	70.41; 84.99	—	[82]
1 M FeCl ₂ + 1 M CrCl ₃ + 3 M HCl (65 °C)	Nafion 115	GF; none; 9 cm ²	60	93.1	81.8	76.1	1.1% (60 mA/cm ²)	[64]
1 M FeCl ₂ + 1 M CrCl ₃ + 3 M HCl + 0.008 M Bi ³⁺ (65 °C)	Nafion 115	GF; thermal; 9 cm ²	60	96.9	89.0	86.3	1.2% (60 mA/cm ²)	[83]
1 M FeCl ₂ + 1 M CrCl ₃ + 3 M HCl (65 °C)	Nafion 115	GF; silicic acid etching; 9 cm ²	120	92.4	86.3	79.7	0.46% (120 mA/cm ²)	[84]
1 M FeCl ₂ + 1 M CrCl ₃ + 3 M HCl (65 °C)	—	GF; boric acid etching; 9 cm ²	120	—	>90	>85	—	[85]
1.5 M FeCl ₂ + 1.2 M CrCl ₃ + 2 M HCl (65 °C)	Nafion 117	Bi-C catalyst electrode; none; 6 cm ²	40	97.4	88.5	86.2	—	[86]
1 M FeCl ₂ + 1 M CrCl ₃ + 3 M HCl + 0.005 M Bi ³⁺ (65 °C)	Nafion NR-212	CP; 4 cm ²	320	~ 97	—	80.7	0.5% (320 mA/cm ²)	[87]
1 M FeCl ₂ + 1 M CrCl ₃ + 3 M HCl + 0.005 M Bi ³⁺	Nafion 212	GF; 4 cm ²	200	—	—	79.6	0.6% (200 mA/cm ²)	[88]



Theoretically, HER will generally occur at the negative potential of these two media, but zinc is a relatively poor electrocatalyst for hydrogen reactions. Therefore, the repeated charge and discharge of ZRFB can be carried out under controlled conditions. At present, the common ZRFB include zinc-manganese RFBs (ZMBs), zinc iodine RFBs (ZIBs), zinc-bromine RFBs (ZBBs), and zinc-air RFBs (ZABs), among which the ZBBs is one of the most successful batteries.

2.3.1 ZMBs

Manganese is abundant on the earth. The content of manganese in the soil is about 0.25%, which is low-cost, low toxicity, and friendly to the environment. Manganese-based materials are the first batch of materials used in zinc-based flow batteries. The reaction [97] is Eq. (9)



Although the zinc manganese flow batteries have the advantages of low cost, low toxicity, and being relatively friendly to the environment, there are still problems restricting the development of zinc manganese flow battery due to the complex electrochemical reaction of manganese. During the operation of zinc manganese flow batteries, the disproportionation reaction of Mn³⁺ is prone to occur, leading to the formation of MnO₂ solids. Due to the incomplete dissolution of MnO₂ and the detachment

of MnO₂ from mechanical cracks in the thick MnO₂ layer, the efficiency of the battery will be severely affected, leading to a rapid decrease in capacity.

Because of the phase change and structural collapse of ZMBs, it is easy to lead to poor stability of the positive electrode, which will affect the stability of the battery. Xie et al. first proposed a Zn-MnO₂ redox couple with good reversibility and stability in a neutral medium (Fig. 7(a)) [99]. This reaction uses neutral Mn(Ac)₂ as the active substance of electrolyte, which can greatly reduce the common dendrite phenomenon in a zinc-based flow battery. Mn²⁺ was deposited on the graphite fiber in the form of MnO₂ through the coordination of Ac⁻, and the redox potential was reduced by 530 mV compared with MnSO₄. In addition, the Zn-Mn flow battery prepared by the Zn/Zn²⁺ redox couple has a CE of 99% and an EE of 78% at a current density of 40 mA/cm² and can be stably cycled more than 400 times.

To solve the problem of forming MnO₂ through the disproportionation reaction of Mn³⁺, dissolving the generated MnO₂ is another solution. Lei et al. proposed a redox medium strategy, using KI to achieve effective MnO₂ dissolution to improve the stability of ZMBs [100]. It can stably cycle 400 times at 2.5 mA-h/cm² and realize 50 cycles at 50 mA-h/cm². At the same time, it also has the highest cycle area capacity among manganese-based batteries (Fig. 7(b)). To improve the reversibility and kinetics of manganese and enhance the redox couple, Minsoo Kim et al. proposed to use bismuth nanoparticles embedded in carbon felt electrode to combine with nickel and magnesium ions

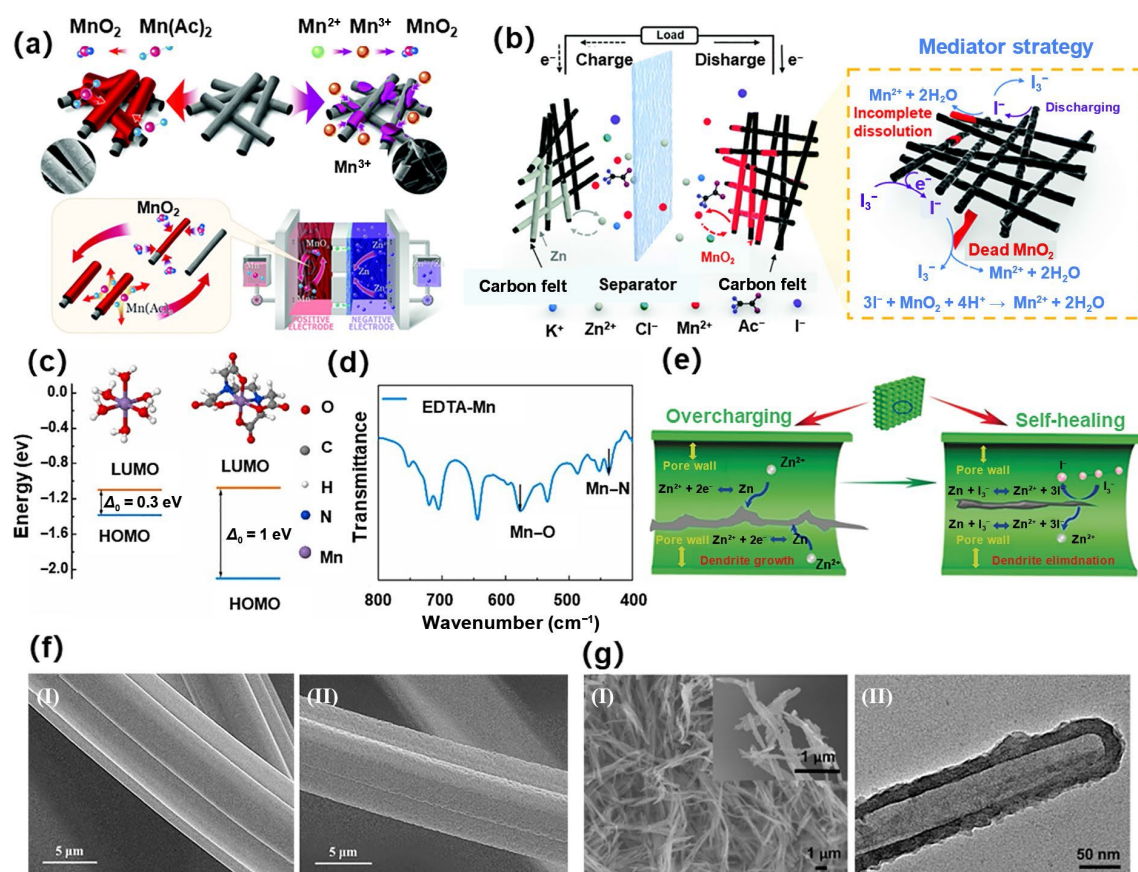


Figure 7 (a) The electrochemical mechanism of the $\text{Mn}(\text{Ac})_2$ (top left corner) and MnSO_4 electrolyte (top right corner). Reproduced with permission from Ref. [99], © The Royal Society of Chemistry 2020. (b) The mechanism diagram of adding KI to the ZMBs to help the dissolution process of MnO_2 . Reproduced with permission from Ref. [100], © The Royal Society of Chemistry 2021. (c) The optimized geometries and highest occupied molecular orbital (HOMO)–lowest unoccupied molecular orbital (LUMO) energy gaps for $[\text{Mn}(\text{H}_2\text{O})_6]^{2+}$ (left) and $[\text{Mn}(\text{EDTA})]^{2-}$ (right). (d) Infrared spectrogram of EDTA-Mn material. Reproduced with permission from Ref. [102], © Elsevier B.V. 2021. (e) Illustration of the overcharging and self-healing process. Reproduced with permission from Ref. [104], © WILEY-VCH Verlag GmbH & Co. KGaA, Weinheim 2018. (f) SEM images of (I) graphite felt and (II) thermally treated graphite felt. Reproduced with permission from Ref. [105], © Elsevier Ltd. 2018. (g) (I) SEM images and (II) transmission electron microscopy (TEM) images of carbonized tubular polypyrrole (CTPPy). Reproduced with permission from Ref. [106], © Elsevier Ltd. 2018.

simultaneously to form metal ion catalyst (MIC) to prepare a high voltage aqueous hybrid zinc-manganese flow battery with double-membrane and three-electrolyte configuration. It can realize the reversibility of manganese redox couple at a working voltage of up to 2.75 V, helping ZMBs achieve a current density of 15 mA/cm², and the EE reaches 89.8% under 150 charge–discharge cycles [101].

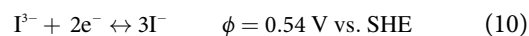
By inhibiting the disproportionation reaction of Mn^{3+} in ZMBs, the deposition of MnO_2 can be effectively prevented, which is also an idea to solve the deposition of MnO_2 . Recently, to solve the problem of MnO_2 deposition during the operation of ZMBs, Yu et al. proposed a highly reversible ZMB based on a reversible $\text{Mn}^{2+}/\text{Mn}^{3+}$ redox reaction for the first time [102]. Ethylene diamine tetraacetic acid (EDTA)-Mn is used as the positive electrode–electrolyte of the battery. Because of the synergistic effect of EDTA, EDTA has a strong ligand affinity for Mn (Figs. 7(c) and 7(d)), which completely inhibits the disproportionation reaction of Mn^{3+} in EDTA-Mn and effectively prevents the deposition of MnO_2 . The results show that the prepared ZMB can operate stably for 300 cycles at 20 mA/cm² and continuously provide 98% of CE and 75% of EE.

Although the manganese-based flow battery has many advantages, such as high solubility, easy preparation, and environmental friendliness, due to the changeable valence state of manganese and easy disproportionation reaction, it is necessary to measure the valence state change of manganese more accurately in

order to understand its mechanism, so as to help the successful commercial application of ZMB.

2.3.2 ZIBs

ZIBs have great potential in large-scale energy storage due to their high energy density, excellent electrochemical performance, and abundant iodine content in the ocean. Although the solubility of I_2 is low, when I^- ions are present in the solution, I_3^- will be formed, which will increase the solubility of the iodine solution. According to the ZIBs reported by Li et al. [103], the reaction is Eq. (10)

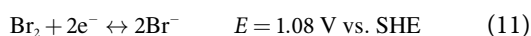


Although the energy density of ZIBs is higher than that of VFBs, and the electrolyte can be free of strong acid and corrosive components, its capacity decay, negative electrode instability, and operation instability during the charge–discharge cycles hinder their commercialization. Therefore, applying ZIBs to large-scale energy storage power stations is necessary to overcome many difficulties. Xie et al. proposed self-healing ZIBs using KI and ZnBr_2 as an electrolyte and a low-cost elastomer porous polyolefin membrane [104]. A 4 mm carbon layer was coated on the membrane, which can further improve the selectivity of the membrane and achieve higher ionic conductivity. Since the I_3^- ions filled in the pores of the porous membrane can oxidize the zinc dendrite, the cycle stability can be improved, and the battery can

recover itself (Fig. 7(e)). At the same time, the introduced Br^- can react with I_2 to form a complex to inhibit the deposition of I_2 . In addition, to effectively prevent the precipitation of hydroxide and zinc oxide in the circulation process, KI is added instead of ZnI_2 as the anolyte. The battery achieved energy densities of 69 and 80 Wh/L and an EE of about 80% and has been continuously operated more than 1000 times in three months, with no obvious change in efficiency.

2.3.3 ZBBs

The ZBBs is a promising battery for large-scale applications due to its low cost and long service life. ZBBs can exhibit excellent stability and efficiency in 2000 cycles (356 h) at a current density of 30 mA/cm² and maintain stable battery performance [107]. The reaction [108] in a typical ZBBs is Eq. (11)



However, the slow Br_2/Br^- couple reaction and the zinc dendrite problem lead to low power density and poor cycle stability. Xu et al. reviewed the reasons for the formation and growth process of zinc dendrite in ZBB [109]. Overpotential and local currents determine the extent of dendrite growth and proposed methods to prevent zinc dendrite from changing the physical characteristics of batteries, improving the performance of electrodes and membranes, and adding high-performance additives or surfactants.

For ZBBs, the formation of zinc dendrite due to uneven zinc plating during charging is still a major reason hindering its commercial development. To achieve dense zinc deposition during charging, the method of adding additives to the electrolyte is proposed. However, these methods are harmful to the environment and will increase the battery cost. Therefore, people are more inclined to help with zinc deposition. In this regard, Yin et al. proposed a simple and effective method to inhibit zinc dendrite. They used a multifunctional binder-free tin (SN) modified 3D carbon felt anodic host (SH) [110]. The prepared SH helps zinc form dense electrochemical deposition during charging by providing stronger Zn nucleation sites and deposition overpotentials. It can also help the continuous and stable operation of the ZBBs, which will greatly prolong the life of the ZBBs and effectively inhibit the HER.

The uniform distribution of zinc in the negative electrode of the ZBBs is of great significance in improving the utilization rate of the electrode, inhibiting the formation and growth of dendrites, and increasing the discharge capacity. Jiang et al. adopted a top-down method to change the distribution and morphology of zinc by adjusting the surface properties of carbon and changing the distribution of the single vacancy potential of the negative electrode [105]. Therefore, a GF negative electrode with uniform zinc distribution can be prepared through the uniform distribution of a single vacancy on the negative electrode. The GF anode with a large number of carbon defects was prepared by heat treatment. Figs. 7(f)(I) and 7(f)(II), respectively shows the original graphite felt electrode and the graphite felt electrode after heat treatment. It can be seen that there are many disordered holes in the GF electrode after heat treatment. The surface of the GF changed from smooth to rough. The formed pores mean the loss of carbon atoms, the fracture of C–C, and the formation of vacancies. The anode prepared in this way has a more uniform zinc distribution. Recently, Lu et al. proposed a multifunctional carbon felt-based electrode with nitrogen-rich defects [111]. The prepared electrode has abundant deposition points, which can

uniformly make zinc deposit on the electrode. Meanwhile, a large number of nitrogen-containing group defects provide higher catalytic activity for bromine reactions. To solve the problem of zinc dendrite generation and solid zinc accumulation in zinc-based flow batteries, improving the membrane is another idea. Chen et al. prepared a montmorillonite composite poly (another sulfone) ion conducting membrane (MMT-M) by selecting montmorillonite (MMT) with high mechanical strength and negative charge performance [112]. Because the high mechanical strength of MMT can help the membrane avoid the damage of solid zinc, it can also inhibit the formation of zinc dendrites by repelling zinc ions in the negative electrolyte, thus achieving the role of the protective membrane; it can prolong the life of the battery and improve its cycle stability. Another major issue affecting the development of ZBBs is the improvement of reaction kinetics of the Br_2/Br^- redox couple. In order to improve the reaction kinetics of bromine in the cathode, various methods are often used to modify the electrode. During thermal activation, platinum and carbon in the electrolyte are common Br_2/Br^- redox couples in ZBBs. Mariyappan et al. proposed to improve the charge transfer between bromine and the electrode by introducing platinum on the positive electrode surface (Fig. 8(a)) to improve the reaction kinetics of the Br_2/Br^- redox couple, which can achieve 300 cycles of no capacity attenuation under the current density of 30 mA/cm² [113].

The traditional electrode material has a high thickness, which will generate high electrode polarization for the Br_2/Br^- redox couple, and this will also increase the internal resistance of the RFBs and limit the current density. Therefore, in order to reduce the internal resistance of the electrode material and improve the electrode dynamic weak reaction, people are urged to pursue electrode materials with thinner thicknesses and higher conductivity. Suresh et al. prepared a surface-modified carbon paper as the cathode material of ZBBs by improving the Hummers method [114]. Because the surface-modified carbon paper has good reaction kinetics, it improves the reversibility of the Br_2/Br^- redox couple, reduces the internal resistance of the RFBs, and makes the electrode surface have more oxygen-containing functional groups, which can also promote the redox reaction of Br_2/Br^- , improving the performance of ZBBs.

For ZBBs, there is a serious problem of Br_2/Br^- redox galvanic polarization, which will bring huge losses to the battery. The use of catalysts is a common solution to this problem. Platinum and carbon have better effects on Br_2/Br^- redox couple than other catalysts. For the sake of cost, they affect the development of platinum catalysts. As for carbon catalysts, their application is restricted due to their low efficiency and complex process. In order to solve these problems, Xiang et al. proposed a nitrogen-doped carbon as the positive electrode of a ZBB [115]. The successful doping of nitrogen through high-temperature ammonia corrosion can provide higher conductivity and more abundant heteroatom-activated functional groups. It can also improve the electrode's specific surface area, making it more stable than the original electrode. The modified electrode has an excellent electrocatalytic activity for Br_2/Br^- redox couple, representing the highest reported performance.

Another obstacle to the development of ZBBs is the low power density due to the low kinetics of Br_2/Br^- . To solve this problem, Wu et al. proposed an efficient catalyst for ZBBs [108]. They synthesized an N-doped graphene nanosheet catalyst by pyrolysis. Then, the catalyst was coated on the graphite felt electrode. Because doped nitrogen can have high electronegativity, it is an

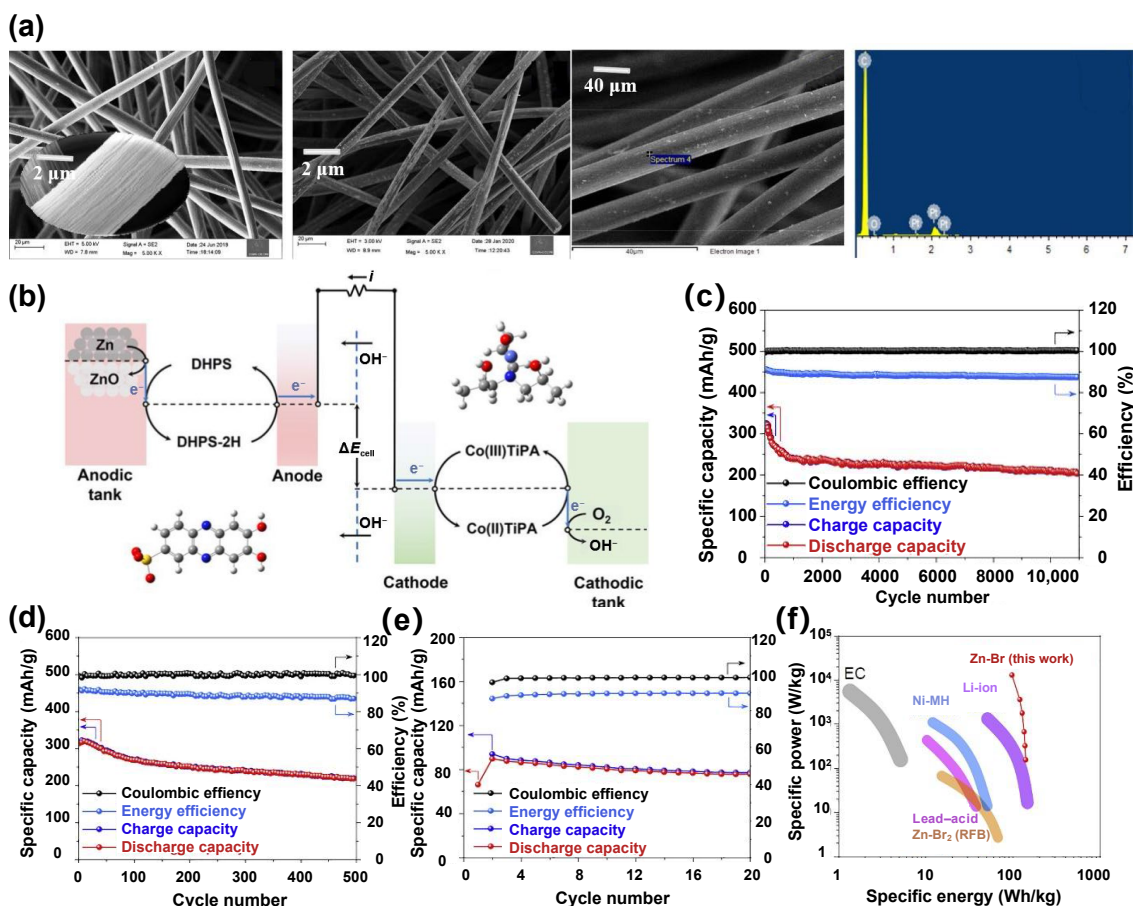


Figure 8 (a) Field-emission SEM (FE-SEM) images of HT-GF and Pt-1; energy-dispersive X-ray (EDX) analysis spot and EDX spectrum of Pt-1. Reproduced with permission from Ref. [113], © The Electrochemical Society (“ECS”). Published on behalf of ECS by IOP Publishing Limited 2021. (b) Schematic diagram of anodic and cathodic compartments undergoing zinc oxidation and ORR reactions, respectively. Reproduced with permission from Ref. [123], © American Chemical Society 2022. (c) Long-term cycling stability at 5000 mA/cm². (d) Cycling performance of the battery with Cu foil anode at 5000 mA/g (15 mA/cm²). (e) Cycling performance of the battery with TPABr₃ cathode at 1.27 mA/cm². (f) Comparison between the Ragone plot of the Zn-Br static battery and several standard devices. Reproduced with permission from Ref. [116], © The Author(s) 2020.

effective method to realize electronic modulation and can provide a favorable electronic structure for electrocatalysis. At the same time, graphene is more graphitized than graphene oxide, so it is more durable. Thus, the charge transfer between the ions adsorbed by ZBBs and the electrode is enhanced, the charge transfer resistance is reduced, and the dynamics are faster.

Wu et al. synthesized a kind of carbonized tubular polypyrrole (CTPPY) (Fig. 7(g)) is rich in nitrogen-containing and oxygen-containing functional groups and used it in the cathode material of ZBBs for the first time, which can improve the reaction kinetics of Br₂/Br⁻ and enhance the performance of ZBBs [106]. And the charging voltage can be reduced, the discharge voltage can be increased. The prepared cathode material can ensure that there is no degradation phenomenon after 100 cycles, showing good stability and durability.

For ZBBs, traditional auxiliary components (such as pipes, reservoir components, and ion-selective membranes) have an essential impact on bromine diffusion. In order to explore the impact of these components on battery performance, Gao et al. studied a zinc-bromine static battery without these traditional auxiliary components, but using glass fiber membrane [116]. The zinc bromide stationary battery can not only achieve low self-discharge rate and high battery EE but maintain the advantages of zinc bromide redox couple. It can reduce the self-discharge rate of ZBB and improve energy efficiency. It can achieve a high specific

energy of 142 Wh/kg and a high EE of 94%. After optimizing the electrode structure, the proposed RFB can stably achieve more than 11,000 cycles (Figs. 8(c)–8(f)).

2.3.4 ZABs

ZABs are also typical zinc-based RFBs. Compared with a lithium-ion battery, ZABs have a higher theoretical energy density, lower cost, less environmental pollution, and abundant raw materials. Because the active cathode material of ZABs is oxygen in the air, it is almost infinite in principle, so ZABs are considered a feasible large-scale energy storage technology. In an alkaline environment, the ZABs reaction [117] is Eq. (12)



Compared with the rapid reaction kinetics of the anode, the oxidation–reduction reaction (ORR) in the three-phase reaction zone composed of catalyst, electrolyte, and air, and the oxygen evolution reaction (OER) in the two-phase reaction zone composed of catalyst and electrolyte near the cathode are slow. During battery discharge, the ORR reaction occurs at the cathode, O₂ is reduced to hydroxyl by electrons, and the OER reaction occurs during charging. Therefore, the electrochemical performance of its battery mainly depends on the ORR reaction and OER reaction at the cathode [118]. Therefore, to improve the reaction kinetics of ORR reaction and OER reaction of ZAB, it is

of great significance to study bifunctional catalysts with low prices and excellent performance for ZAB. Therefore, people focus on developing and utilizing bifunctional electrocatalysts with high activity [119].

Compared with other types of catalysts, catalysts derived from the metal-organic framework (MOF) can easily adjust the pore structure due to their large specific surface area and controllable pore structure to obtain the optimal specific surface area and pore structure distribution. Cui et al. synthesized a MOF-derived FeNi co-doped catalyst (termed as B-FeNi-N/C-1000) by using a binary ligand strategy [120]. They combined the excellent controllable pore structure of MOFs and FeNi synergistic catalytic function, so that the prepared bifunctional catalyst has a larger comparative area and more outstanding electrochemical efficiency. The charge and discharge tests of the prepared ZAB showed that the voltage efficiency decreased by only 2% after 95 h of stable operation, showing good stability.

Because platinum metal has an electronic structure interacting with oxygen molecules and intermediate substances, it can help promote ORR and OER reactions. Zhang et al. proposed a bifunctional catalyst [121]. They chose the method of embedding ultra-low supported Pd into the surface oxidized PdNiMnO porous membrane to promote the activity of the catalyst for ORR by using the strong metal carrier interaction (SMSI) effect. This can improve the utilization rate of platinum metal to improve the performance of ORR. At the same time, Mn doping can also promote the surface oxidation reaction. As a functional carrier, Ni is used to help stabilize Pd. The maximum power density of the prepared ZAB is 211.6 mW/cm², which can realize stable operation for 2000 h under the current density of 10 mA/cm².

Another problem plaguing ZAB is the high polarization of air electrodes during charge and discharge, which reduces the energy efficiency of ZAB. However, adding soluble redox mediators (RMS) to the electrolyte is another effective method that can promote the ORR reaction and OER reaction and not cause large free energy loss. To improve the OER of ZAB, RMS is a substitute for traditional solid catalysts, commonly used in lithium-oxygen batteries, and is believed to alleviate the slow reaction kinetics of lithium-oxygen battery electrodes. Huang et al. innovatively proposed adding the redox medium of anthraquinone 2,7-disulfonic acid sodium salt (AQDS) as RMS to ZAB, which can enhance the reaction kinetics of ZAB under high pH conditions, thus improving the energy efficiency and cycle performance of ZAB [122]. The average EE of the prepared ZAB can reach more than 85% when only ORR and OER reactions are dominant, and can still reach 68.8% when fully charged and discharged. The energy efficiency is much higher than that of ordinary ZAB.

Due to the working principle of ZABs, the anode consumption or passivation problem will inevitably occur during the use of ZAB. To avoid waste, the common treatment method is to replace the anode material and electrolyte to restore capacity. However, each replacement process is too cumbersome, and the battery performance will decline. In order to solve this problem and realize the uninterrupted operation of the battery, Wang et al. proposed a redox-mediated Zn-air fuel cell (RM-ZAFC) according to the concept of redox targeting (RT) [123]. Due to the directional effect of the redox reaction, the O₂ and zinc oxide generated by the reaction are placed in different reactor tanks, and the zinc oxide generated during the battery discharge is deposited on the zinc particles in the tank (Fig. 8(b)). After the full discharge, replacing the zinc particles in the reaction tank can realize the rapid charge-discharge of the battery. This modular design makes the operation more convenient and flexible.

Although there are many solutions to the problem of slow reaction kinetics of redox and oxygen precipitation at the cathode of ZAB, there are still many problems. Therefore, to realize the large-scale commercialization of ZAB, the future development of multifunctional, low-cost, and high catalytic activity bifunctional catalysts is the focus of research and development of ZAB.

2.3.5 Brief conclusion

Although ZRFB is still in the early stage of development and commercialization compared with other battery systems. However, due to the advantages of high theoretical capacity of metal zinc, rich earth reserves of zinc ores, long cycle life of the battery, etc., people have conducted extensive research on the electrolyte, electrode, and membrane of ZRFB (Table 3). Since ZRFBs typically utilize metal deposition reactions for charging and discharging, dendrite phenomena are prone to occur and can affect the long-term stability of the battery. Moreover, this phenomenon is more severe at high current densities. The modification of electrode materials is an important method, and we can learn from other mixed redox flow batteries. Shi et al. used high-load solid conversion electrodes to replace metal deposition electrodes, which eliminated dendrite problems and metal surface capacity limitations [124]. Yao et al. proposed and demonstrated a metal electrode based on Sn(OH)₆²⁻/Sn redox couple, which also achieves dendrite-free flow batteries [125]. As a key component of zinc-based flow batteries, membrane modification is also an effective strategy. Lu et al. proposed a new type of porous polyolefin/polyethylene glycol (PEG) composite membrane by using the high-quality chemical stability of the Daramic membrane as the membrane matrix and combining it with the multi-functional PEG layer with high conductivity [126]. This membrane has high conductivity and can accelerate the propagation of zinc ions. Moreover, the dense PEG coating can achieve uniform electric field distribution, inhibit the formation of zinc dendrites, and achieve a non-dendritic zinc layering process. I believe that ZRFB can achieve large-scale commercial applications in the near future and become one of the most high-performance energy storage systems.

Compared with other costs and later maintenance costs, electrolyte costs account for a significant part of the total cost of RFBs. So the mineral conditions of different elements (Table 4) will determine the industrial development of different RFBs.

3 Organic redox flow battery

3.1 Aqueous organic RFBs (AORFBs)

The electrolyte of AORFB mainly uses water as a solvent because most active organic substances are hydrophobic functional groups, resulting in low solubility in water. Thus, hydroxyl, quaternary ammonium, and sulfonate-based hydrophilic functional groups are introduced to improve the solubility of active organic substances which can also increase the redox potential of the electrolyte. Through the design of active molecular functional groups, the energy density and EE of the battery can be improved, laying a solid foundation for large-scale energy storage. According to the acidity and alkalinity of the electrolyte, AORFB can be divided into acidic, alkaline, and neutral systems.

3.1.1 Acidic system

Acidic conditions provide good conductivity for proton transport and increase the solubility of organically active substances. Due to

Table 3 Operational parameters and performance of zinc-based RFBs in recent years

Flow battery	Electrolyte composition	Membrane	Electrode	Current density (mA/cm ²)	VE	CE	EE	References
Zn-Mn	EDTA-Mn/ZnCl ₂	Perfluorinated sulfonic acid membrane	CF	20	—	98%	75%	[102]
		Anion exchange membrane	CF	15	—	—	89.8	[101]
	Zn(Ac) ₂ /Mn(Ac) ₂	Composite porous polyolefin ion conducting membrane	GF	40	79%	99%	78%	[99]
Zn-I ₂	ZnBr ₂ /KI	Polyolefin porous membrane	GF	80	85.42%	96%	82%	[104]
	Ferricyanide	Nafion 212	CF	100	—	98%	75%	[98]
Zn-Br ₂	ZnBr ₂ /ZnCl ₂	Porous separator	GF	40	85.35%	94.72%	80.42%	[110]
	ZnBr ₂ /NH ₄ Cl	Nafion 211	GF	80	—	—	76%	[106]
	ZnBr ₂	Nafion 212	CF	30	86.7%	99.9%	87%	[107]
	ZnBr ₂	Nafion 211	GF	80	—	—	84%	[108]
	ZnBr ₂ /ZnCl	Microporous membrane	Carbon paper	20	86%	95%	78%	[114]
	ZnBr ₂ /ZnCl	Porous separator	GF	30	87.02%	95.52%	—	[113]
Zn-air	ZnO/KOH	—	Zinc foil	10	50%	100%	50%	[119]

Table 4 Reserves, annual output, and annual demand of different elements

Element	Global reserves (million tons)	Global annual production (million tons)	Annual demand in China (million tons)
Iron	180,000	2600	1420
Chromium	5700	40	23.68
Manganese	1500	20	6.9761
Iodine	7.60	0.028	30–40
Bromide	100,000,000	1	0.293
Zinc	250	0.011108	6.606

the limited variety of active organic substances and the lack of molecular design engineering studies, it is necessary to use them with other redox pairs. Amirreza et al. proposed the anthraquinone-2,7-disulfonate disodium (AQDS)/Br₂ organic-inorganic hybrid flow battery AQ-based ORFB system, with the positive electrolyte using the active organic substance and the negative electrolyte using the Br₂-Br⁻ redox substance [127]. During the redox reaction, AQDS has good reaction kinetics and electron transport properties that two electrons move to the graphite electrode in an acidic solution. The polarization curves in different state of charge (SOC) states are shown in Fig. 9(a). At high SOC, the voltage and current density show a linear relationship. Under low SOC conditions, only in the current density above 40 mA/cm² could the linear regression relationship be found, which mainly resulted from the large resistance of the battery itself. Moreover, after 200 cycles, the average discharge capacity remained above 95%, which confirmed that the battery system had good stability and excellent reversibility (Fig. 9(b)). Figure 9(c) shows that after 200 charge-discharge cycles, the pH of the electrolyte fluctuated less and the battery voltage remained at 1.3 V, which proved that the flow battery had stable performance. The AQDS/Br₂ RFBs system was further optimized, the thickness of the ion exchange membrane was reduced, and the Nafion 212 was replaced with Nafion 115 [128]. At 250 mA/cm², the charge-discharge capacity can still remain relatively stable after 200 cycles. After 5000 cycles, its charge and discharge capacity was only lost by 30%, which proved that the battery can still have good stability and high charge and discharge capacity under high current density.

Michael R. Gerhardt and collaborators studied four anthraquinone derivatives as anode active substances in AQDS/Br₂ flow battery systems, comparing the standard reduction potentials and open circuit voltages of anthraquinone-2-sulfonic acid (AQS), AQDS, 1,8-dihydroxyanthraquinone-2,7-

disulfonic acid (DHAQDS), and 1,4-dihydroxyanthraquinone-2,3-dimethylsulfonic acid (DHAQDMS), respectively [129]. As shown in Fig. 9(d), the reduction potential was regulated by controlling the functional group attachment on the molecular surface. At the SOC state, the open circuit voltages of the DHAQDMS battery and the DHAQDS battery were higher than that of the AQS base battery, and as the SOC increased, the open circuit voltages of the DHAQDMS battery and the DHAQDS battery increased linearly and then stabilized, indicating that the active organic substance had been decomposing during the operation of the battery (Fig. 9(e)). This decomposition reaction was reversible for DHAQDS but irreversible for DHAQDMS. The capacity of a DHAQDMS battery was significantly lower than that of a DHAQDS battery after 20 charge and discharge cycles (Fig. 9(f)).

Because organic-inorganic hybrid flow batteries are expensive and organic active materials are widely available and inexpensive, all-organic flow batteries become a better choice for long-term energy storage. Yang et al. first reported a full anthraquinone aqueous flow battery with AQS negative electrolyte and 1,2-dihydrobenzoquinone-3,5-disulfonic acid (BQDS) as the positive active material, and its total cost was about \$10 per kWh of electricity [130]. The CV test of the positive and negative active materials showed that the battery voltage was 0.97 V. The AQS and BQDS concentrations were 0.2 M, dissolved in 1 M H₂SO₄, and the charge and discharge capacity didn't reduce significantly after 12 cycles at 200 mA/cm², indicating that anthraquinone all-organic flow batteries had good chemical stability in redox reactions in acidic electrolytes. Although the charge-discharge capacity and electrochemical properties of all-organic flow batteries are weak, it can be proved that the all-organic flow battery system is feasible. Optimizing the battery structure and the functional group design of active organic materials will greatly improve the performance of the battery.

Many studies have reported that due to the poor stability of the

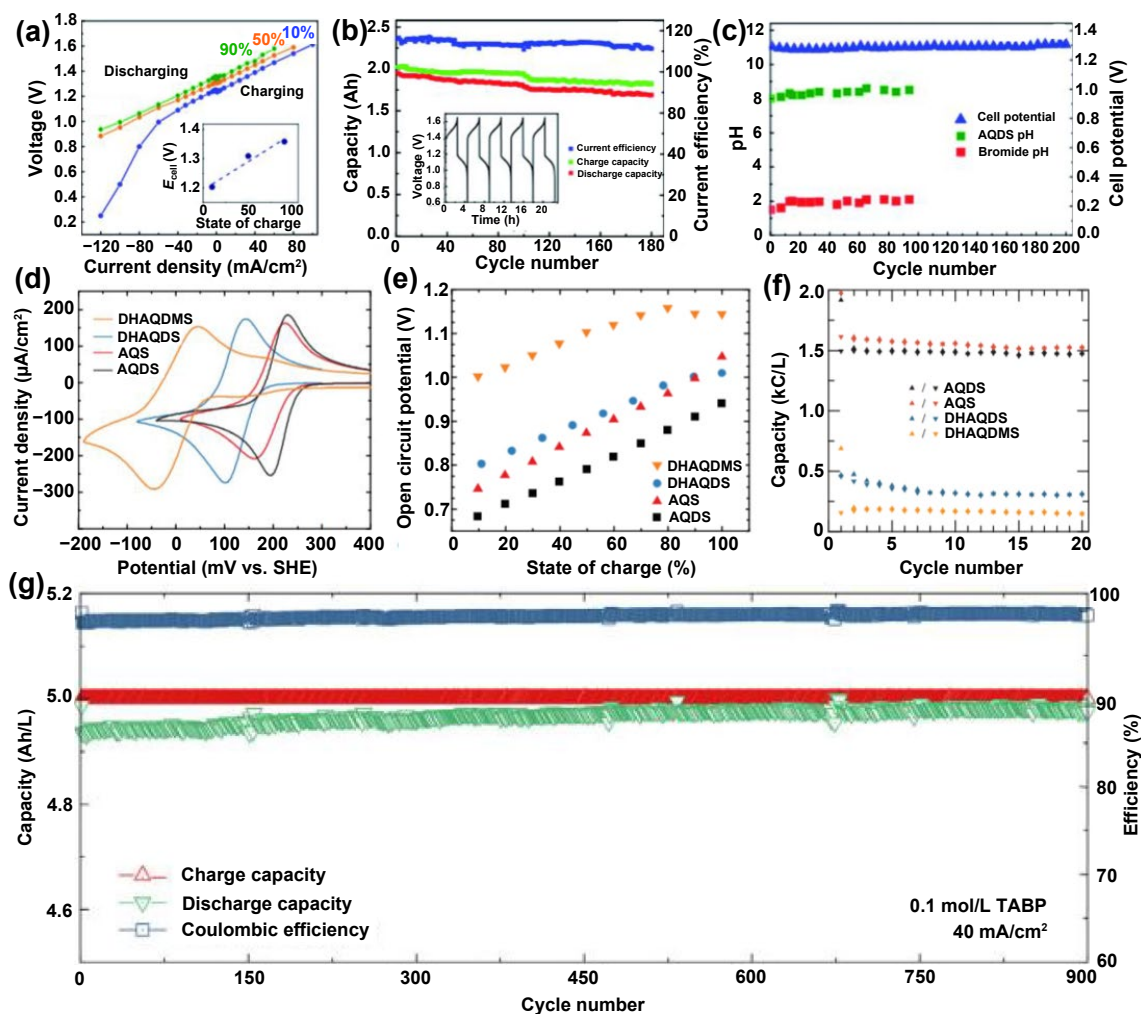


Figure 9 (a) Polarization curves under three different SOCs. (b) Current efficiency, charging capacity, and discharge capacity change with the number of cycles. (c) Variation of pH with the number of cycles at random SOC and 50% SOC. Reproduced with permission from Ref. [127], © The Royal Society of Chemistry 2017. (d) Cyclic voltammetry of AQDS, AQS, DHAQDS, and DHAQDMS. (e) Diagram of open circuit voltage variation with discharge state of different battery samples. (f) The capacity of each quinone solution varies with the number of cycles at 50 mA/cm². Reproduced with permission from Ref. [129], © WILEY-VCH Verlag GmbH & Co. KGaA, Weinheim 2016. (g) The cycle capacity and efficiency tests of the RFB with TABP at 40 mA/cm². Reproduced with permission from Ref. [131], © Science China Press. Published by Elsevier B.V. and Science China Press 2020.

organic and electrical pairs, ORFBs need nitrogen or argon atmosphere to maintain stable operation, which brings serious challenges to large-scale applications of batteries. Liu et al. designed and developed an air-stable bisphenol cathode 3,3',5,5'-tetramethylaminemethylene-4,4'-biphenol (TABP), an electrical pair characterized by high solubility and high potential [131]. In this design, the biphenyldiol structure was replaced by biphenyl, and the conjugate structure of the biphenyl could improve its stability in the air. In addition, the biphenyl structure effectively inhibited Michael's addition side reaction and improved the electrocatalytic properties of the active cathode. The organic flow battery was assembled with TABP as the positive electrode and silicon tungsten acid as the negative electrode. At a current density of 40 mA/cm², after 900 cycles, the charge–discharge capacity of ORFB has not been significantly degraded, and the CE still maintained at more than 95% (Fig. 9(g)). In addition, the ORFB achieved an EE of 85% and a charge–discharge capacity of 47 Ah/L at 60 mA/cm².

3.1.2 Alkaline system

AORFB mainly has two problems in acidic conditions. First, the battery voltage is low; second, the active cathode material is

defective. OH⁻ has a fast migration rate in alkaline conditions. Therefore, alkaline systems are considered ideal batteries for large-scale energy storage.

Wang et al. designed an anthraquinone-based redox reversible molecule with high recovery and low cost 1,3,5,7-tetrahydroxyanthraquinone (1,3,5,7-THAQ) [132]. A solubility of up to 1.88 M under alkaline conditions and a low redox potential of -0.68 V (pH = 14) are suitable as an anode active material in AORFB. When paired with a ferrocyanide cathode active substance to form a battery, the voltage could reach 1.2 V (Fig. 10(a)). Figure 10(b) shows that the maximum output power density of the battery was 0.36 W/cm². As the SOC increased, the battery output power density also increased. In Fig. 10(c), after a charge and discharge cycle of not less than 600, the capacity decay rate of the battery was only 0.35%/day. The CE was higher than 95%, indicating that the active anode material did not undergo secondary electrochemical polymerization reaction in a highly alkaline aqueous solution and had good cycle stability. Due to the problems of short circulation life and low capacity of AORFBs, Huang et al. reported that molecular engineering DHAQ-based alkaline electrolytes demonstrated molecular degradation mechanisms in electrochemical reactions and developed

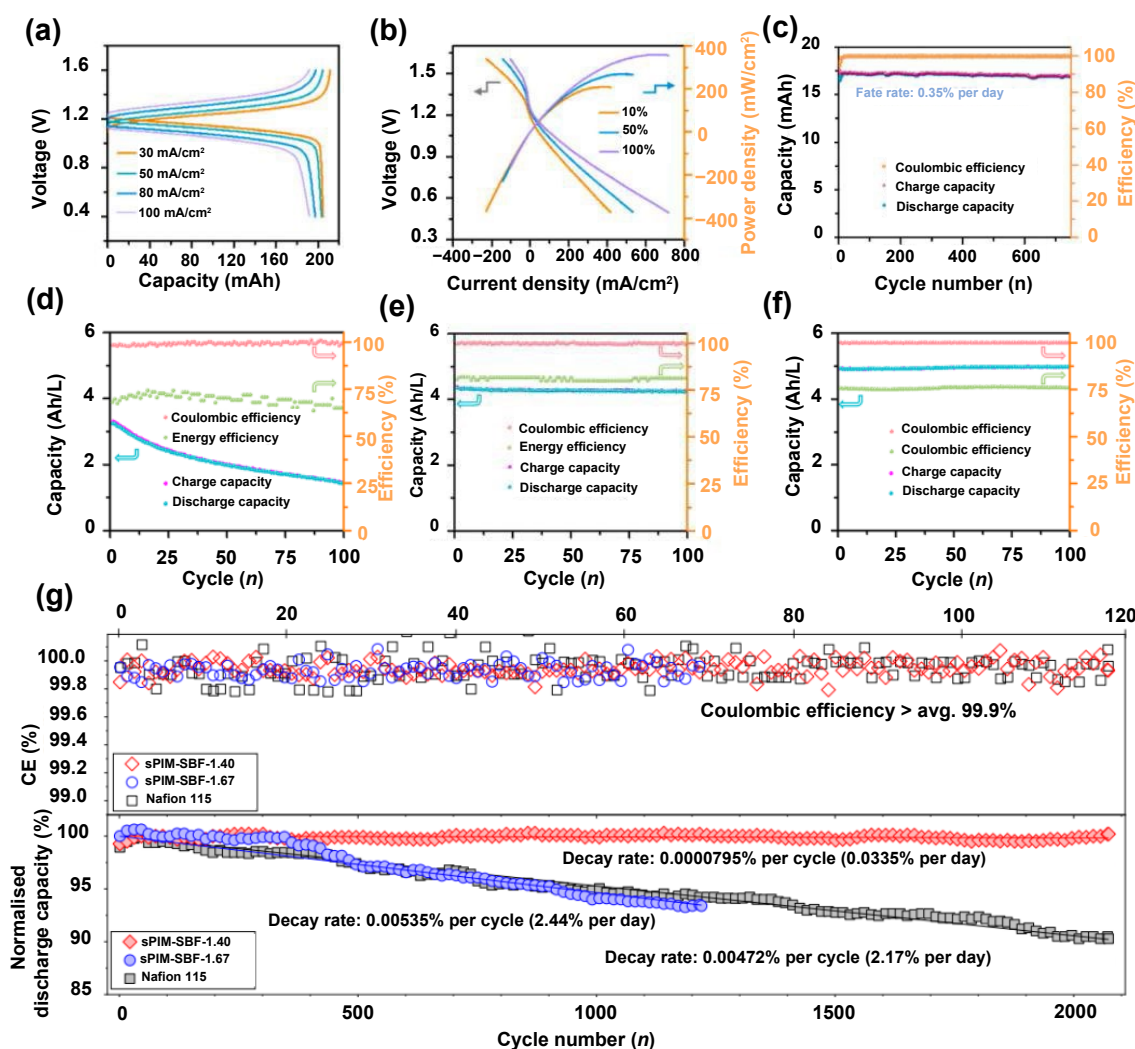


Figure 10 (a) Relationship between voltage and capacity at current densities of 30, 50, 80, and 100 mA/cm². (b) At 10%, 50%, and 100% SOC, the voltage and power density of RFBs vary with current density. (c) Capacity and efficiency variation of AFRB over 100 cycles. Reproduced with permission from Ref. [132], © Elsevier B.V. 2022. At 100 mA/cm², the capacity and efficiency of ARFBs assembled with anode electrolyte based on (d) HP, (e) AHP, and (f) BHPC varied with the number of cycles. Reproduced with permission from Ref. [134], © American Chemical Society 2020. (g) Cycling stability of RFBs assembled from sPIM-SBF-1.40 (134 μM), sPIM-SBF-1.67 (177 μM), and Nafion 115 membranes at pH = 9 and 100 mA/cm². Reproduced with permission from Ref. [138], © The Author(s) 2022.

composite electrolytes with improved electrochemical properties [133].

The composite electrolyte was anode material, and the ferrocyanide compound was cathode material, which assembled the battery. After a cycle of 1100 h (20 mA/cm²), the discharge capacity of the battery was 573 mAh, and the average discharge voltage of the battery was 0.89 V. Wang et al. designed three different phenazine derivatives (2-hydroxyphenazine (HP), 2-amino-3-hydroxyphenazine (AHP), and 5-hydroxybenzo[a]phenazine-carboxylic acid (BHPC)) through low-temperature green synthesis [134]. According to electrochemical performance tests, the orthostatic substituents of hydroxyl groups in phenazine derivatives affected battery performance. Figure 10(d) shows that after 100 charge–discharge cycles, the charge and discharge capacity of HP batteries reduced from 3.25 to 1.23 Ah/L due to the polymerization of active organic substances in the electrolyte. In Fig. 10(e), after 100 charge–discharge cycles, the capacity of the AHP battery remained at 4.35 Ah/L, the CE reached about 100%, and the EE averaged 80%, indicating that AHP was very suitable for this battery system. At 100 mA/cm², the EE of the BHPC battery reached 77%, the CE > 99%, and the

charge–discharge capacity was 4.98 Ah/L after 100 charge–discharge cycles. Figures 10(e) and 10(f) show that AHP and BHPC did not undergo polymerization reactions during charge and discharge [134]. Liu et al. synthesized a water-insoluble hexaazatriphenylene (HATN) by microwave-assisted Schiff alkali condensation reaction and studied its performance in AORFB [135]. And after 1500 cycles, the CE was 99.7%, the EE was 75.5%, and the charge–discharge capacity was 71%.

Wu et al. obtained the lowest capacity decay rate by using sulfur atom-linked carbon materials and were the record holder for the most stable materials [136]. Aaron Hollas et al. built an organic battery system by a phenazine core for the first time, with a battery voltage of 1.4 V and a theoretical energy density of 67 Ah/L [137].

Ye et al. reported on ion exchange membranes prepared by sulfonating a spirobifluorene-based microporous polymer which can be used for ion size selection and have high ion selectivity in RFB applications [138]. Ion-screened sulfonated polymer membranes can not only optimize the transfer of cations by controlling the degree of sulfonation but also inhibit the crossover of organic molecules. In addition, the enhancement of the membrane's selectivity weakened the phenomenon of capacity

decay while maintaining good ionic conductivity in the alkaline electrolyte, in which the active organic material exhibited long-term stability [138]. Figure 10(g) shows that after 2000 charge–discharge cycles, the average CE of the spirofluorene-based polymers of intrinsic microporosity-1.40 (sPIM-SBF-1.40) battery was 99.9%, and the charge–discharge capacity attenuation rate was 0.0335% per day compared to the Nafion 115 battery 2.1% per day.

3.1.3 Neutral system

Whether the electrolyte of the aqueous organic flow battery is acidic or alkaline, most ion exchange membranes are Nafion membranes, whose prices and the system cost are relatively high. In addition, the acidic and alkaline electrolytes are corrosive. The assembly parts of the battery should have a certain corrosion resistance function, while the system cost increases relatively. Moreover, acidic and alkaline batteries have a greater environmental loading. Therefore, neutral water organic flow batteries have become a hot spot. In neutral systems, the molecular design of active organic materials is necessary. Usually, hydrophilic cations are added to functional groups involved in redox reactions, and then anions dominated by chloride ions are assembled to form chlorinated organic salts eventually. The hydrophilic cation increases the conductivity of the electrolyte with inexpensive chloride salts, and the chloride ions act as selective ions, permeating through the ion exchange membrane.

It is important to study the solubility, chemical activity, and stability of organically active materials under neutral aqueous conditions, as they directly affect the service life and energy density of the battery. Lv et al. reported an anodic liquid organically active material (Dex-Vi) with excellent properties of high charge–discharge capacity, high chemical stability, and low anion exchange permeability [139]. A low-cost hydrothermal violet chloride (BTMAP-Vi) method with high yield was also proposed. The permeability test results showed that Dex-Vi had very low ionic permeability, mainly due to the presence of hydroxyl functional groups slowing down diffusion in the pores and the expansion of hydroxyl groups in the Stokes radius reducing ion mobility [139]. Degradation rate test results showed that Dex-Vi had a lower degradation rate, mainly due to the polymerization of hydroxyl groups under alkaline conditions. Due to the excellent chemical properties of Dex-Vi, the battery was assembled with the stable bis(3-trimethylammonio)propyl ferrocene dichloride (BTMAO-Fc) cathode electrolyte to investigate the electrochemical properties of Dex-Vi [139]. Figure 11(a) shows that after 1200 charge–discharge cycles, the CE was almost attenuated, and the discharge capacity remained roughly stable, which showed that Dex-Vi had excellent electrochemical properties and was an indispensable anode material for neutral aqueous organic RFBs.

In many reports, catholyte mostly use organic–inorganic hybrid salts, while capacity-dense and stable organic catholyte remains a challenge in designing energy-efficient and long-life neutral aqueous organic flow batteries. Fan et al. designed an organic cathode active material 4-[3-(trimethylammonium)acetyl amino]-2,2,6,6-tetramethylpiperidine-1-oxyl chloride (TMAAcNH-TEMPO) with stable chemical properties and high redox potential by molecular engineering which links acetamido and trimethylammonium groups. The density functional theory (DFT) simulation results showed that both the positively charged trimethylammonium group and the large van der Waals coil inhibited TMAAcNH-TEMPO cross-polymerization with ion

exchange membranes, indicating that TMAAcNH-TEMPO had significant cyclic stability [140]. The (NPr)₂V electrolyte and TMAAcNH-TEMPO were used in the organic flow batteries as the catholyte, and the battery performance was studied. Figure 11(b) shows that after 1000 charge and discharge cycles, the attenuation rate of the battery's impulse discharge capacity was about 0.0144%/h, the CE maintained at more than 99%, and the EE can reach more than 75%. Experimental characterization and theoretical simulations have proved that TMAAcNH-TEMPO is an important cathode organic active material for neutral aqueous organic RFBs [140].

The low voltage of organic flow batteries has always restricted their development, and the design of high-voltage batteries has become a research hot spot. Wu et al. reported for the first time the application of methyl purple essence dibromide as a bipolar redox electrolyte material in neutral aqueous organic flow batteries, and the low solubility [MV](Br₃)₂ complex in the positive electrolyte during battery charging not only alleviated the dissolution of Br⁻, but also solved the toxicity of bromine [141]. Bipolar water system organic RFB in the neutral electrolyte environment had stable battery performance, and charge and discharge capacity can reach 10.2 Wh/L, redox voltage up to 1.53 V, and after 100 times of charge and discharge cycles, the total capacity retention rate was 100%, the power density reached 133 mW/cm², and the EE was 56%. Bipolar materials offer a possibility for the development of high-voltage flow batteries.

Most acidic or alkaline flow batteries use Nafion membranes, but the high cost and high proportion of the system are not conducive to commercialization. The selective ions of neutral flow batteries are mostly halogen ions, so an anion exchange membrane or osmotic membrane can be used instead of the Nafion membrane. Xiao et al. reported that quaternary ammonium functionalized fluorinated polyarylene ether (QAFPAE-x) anion exchange membranes had high conductivity and chemical stability, and the grafting of quaternary ammonium salts ensured the membrane hydrophilic properties, and the assembly of fluorine-containing blocks made the membrane have low swelling characteristics [142]. As shown in Fig. 11(c), the QAFPAE-x membrane had more fluorophiles so that its Cl⁻ conductivity increases, leading to the improvement of the battery's VE. Figure 11(d) shows that at 60 mA/cm², after 1500 charge–discharge cycles, its CE, EE, and VE can remain stable, which proved that the battery had excellent electrochemical stability performance. Figure 11(e) shows that the surface functional group of the QAFPAE-100 membrane did not change significantly after 1000 charge–discharge cycles, indicating that the QAFPAE-100 membrane was not involved in the reaction during the charge–discharge process, further demonstrating that the membrane had excellent chemical stability. In the neutral water system organic flow battery, novel structures and designs have emerged, affecting the EE and VE of the battery. However, in the commercialization process, key component materials are still the focus of research.

3.2 Non-aqueous organic RFBs (NAORFBs)

The electrolyte of NAORFBs consists of active organic materials dissolved in organic solvents and the added electrolytes. Compared with aqueous solvents, organic solvents have a higher electrochemical window, and the batteries formed by them have a more open circuit voltage, thereby achieving higher energy density. However, NAORFBs still have problems to be solved. On the one hand, organic redox active materials have low solubility

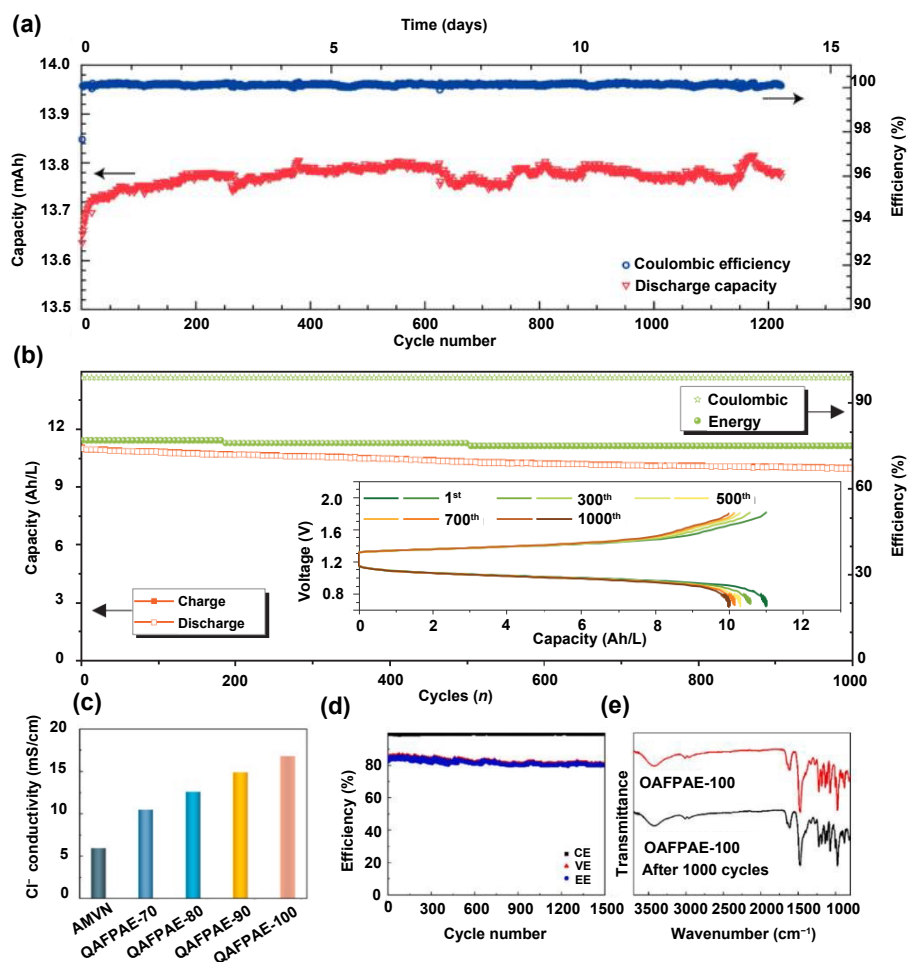


Figure 11 (a) Capacity and efficiency changes of 0.1 M Dex-Vi in 1 M NaCl during 1200 cycles. Reproduced with permission from Ref. [139], © American Chemical Society 2022. (b) Changes in charge–discharge capacity, EE, and CE of a battery with 1000 continuous cycles at 50 mA/cm². Reproduced with permission from Ref. [140], © Wiley-VCH GmbH 2022. (c) Cl⁻ conductivity of 2,2'-azobis (2,4-dimethylvaleronitrile) (AMVN) and QAFPAAE-x membranes. (d) CE, VE, and EE of the QAFPAAE-100 membrane assembled RFBs at 60 mA/cm² under 1500 cycles. (e) Fourier transform infrared (FTIR) spectra of QAFPAAE-100 membrane and QAFPAAE-100 membrane assembled into an RFB after 1500 cycles at 60 mA/cm². Reproduced with permission from Ref. [142], © Elsevier B.V. 2022.

and cannot achieve the expected high energy efficiency; on the other hand, batteries typically operate at low current density.

Liu et al. used 2,5-di-tert-butyl-1-methoxy-4-(20-methoxyethoxy)-benzene (DBMMB) and nitrobenzene (NB) as positive and negative electrodes to assemble organic RFBs with a voltage of 2.2 V and an energy density of 192 Wh/L [143]. The solubility measurement of the active material of nitrobenzene and its derivatives found that under room temperature, nitrobenzene can prepare up to 6.5 M of nitrobenzene electrolyte solution in 0.5 M acetonitrile solution, and the solubility of its derivatives was lower than that of nitrobenzene [143]. In the charge–discharge performance test, the battery can reach 90% of the CE after 100 cycles and discharge cycles at 50 mA/cm². The capacity maintained 50% of the initial capacity, proving that it had stable charge and discharge performance (Fig. 12(a)). As shown in Fig. 12(b), compared with the reported price of active organic materials commonly used in NAORFB, nitrobenzene had the lowest price, reducing the cost of the battery system. Azobenzene assembly NAORFB performance is poor. Xu et al. enhanced the activity of active organic materials by optimizing solvents, supporting electrolytes and membranes, and using azobenzene (AZOB) and DBMMB as active materials dissolved in acetonitrile to assemble batteries at 100 mA/cm², and the EE of the battery can reach 63.5% [144]. It can be seen that nitrobenzene and

azobenzene are the most promising anode-active organic substances of NAORFBs.

In order to make full use of the large potential window of organic solvents, it is necessary to develop energy storage materials with high solubility, multiple redox reactions, and good cycle stability. Yan et al. designed a new soluble and high-potential cathodic active material 2,6-dimethylpiperidine (4-DMPP) for NAORFB by connecting phenothiazine to the diaminocyclopropylene holder by C–N bond, which can still reach more than 90% of the CE after a battery cycle of 266 h at a concentration of 0.5 M [145]. Figure 12(c) shows that at 60 mA/cm², after 300 charge–discharge cycles, the battery EE was still about 70%, and the CE can reach 89%, which proved that 4-DMPP had excellent long-term cycle stability. In addition, there was no significant change in the CV test results before and after the cycle (Fig. 12(d)), indicating that the volume decay was due to the pressure difference, resulting in the formation of a liquid medium in the reservoir by the electrolyte solution at the end of the cycle [145]. Yan et al. reacted phenoxazine with halogen compounds to generate pherazine derivatives as the cathodic active substance of NAORFB and assembled with butyl violet essence as an anodic fluid into a battery, and its cycle performance was better than that of the most advanced cathode liquid under the same conditions [146]. This shows that pherazine derivatives as cathode fluids are necessary to improve NAORFB performance.

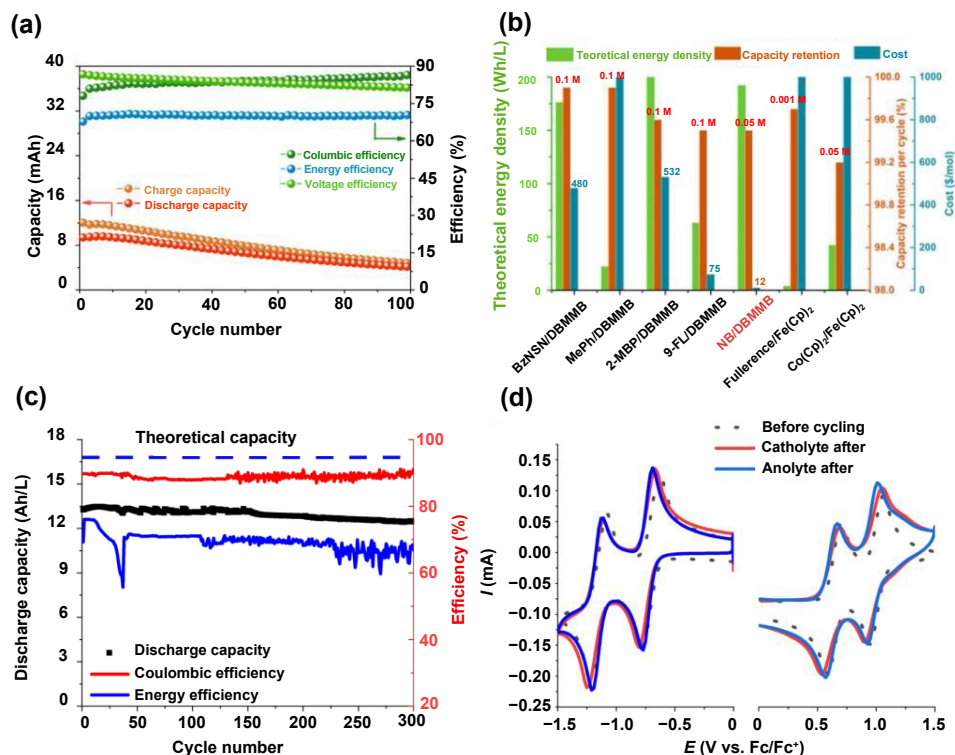


Figure 12 (a) The capacity and efficiency of the batteries vary over 100 cycles at 40 mA/cm^2 . (b) The theoretical energy density, capacity retention, and cost of NAORFBs are compared among reported plots. Reproduced with permission from Ref. [143], © American Chemical Society 2021. (c) Cyclic voltammetry of the positive and negative terminals before and after a battery cycle. (d) Diagram of discharge capacity and efficiency of the battery at 300 cycles. Reproduced with permission from Ref. [146], © Wiley-VCH GmbH 2021.

Bipolar organic redox active materials have a variety of oxidation states and can undergo a variety of redox reactions, so they can be used as anode liquid and cathode fluid to further alleviate the problem of electrolyte cross-contamination. Gabriel Sikukuu Nambafu et al. reported a NANOFB with a homophenyltetraic acid diimide bipolar molecule as the active material [147]. After 100 charge–discharge cycles, it had a CE of 90% and a battery voltage of up to 2.22 V. The research on bipolar materials has promoted the development of high-voltage and high-density flow batteries. Since the electrolyte of NAORFB is an organic solvent, the commercial membrane (Nafion) is unsuitable for selective ion permeation [19]. Ceramic separation membranes exhibit high ion selectivity according to different ionic crystal structures, but the ion conductivity is very low. Many reported NAORFBs use porous membranes as separators, which can achieve high CE and EE but are prone to cross-contamination [148].

3.3 Stability of the active material

Organic active materials have a wide range of sources, low cost, environmentally friendly, and have a high degree of functionalization modification potential. The solubility, redox potential, molecular size, and chemical structure changing reversibility of active materials have a very critical impact on the performance parameters of RFB. So in order to obtain high-performance AORFB, specific functional groups could be used to modify the redox core of organic molecules, thereby changing the relevant properties of the active material [19].

Aziz et al. synthesized a water-soluble anthraquinone compound AQ-1,8-3E-OH with PEG as the solubilizing group as the negative active material, paired with $\text{K}_4\text{Fe}(\text{CN})_6$ to form an AORFB with an open circuit voltage of 1.0 V, a volume capacity of 80.4 Ah/L, and an energy density of 25.2 Wh/L [149]. Liu et al.

constructed a $(2\text{HO-V})\text{Br}_2/\text{Br}_2$ battery system by introducing hydroxyl groups into Vi molecules, with a battery voltage of 1.89 V and a theoretical energy density of 95.1 Wh/L [150]. Janoschka et al. designed and synthesized 2,2,6,6-tetramethylpiperidin-1-yl oxyl (TEMPO) derivative TEMPTMA, containing quaternary ammonium, with an AORFB battery capacity of 54 Ah/L, a total energy density of 38 Wh/L at 1.4 V battery voltage, and a peak current density of up to 200 mA/cm^2 [151]. Pang et al. functionalized dibenzo[b,e]pyrazine by using commercial amino acids in different substitution positions and obtained amino acidulated dibenzo[b,e]pyrazine 1,6-DPAP with good stability and high solubility through screening and comparison, and the daily capacity decay rate was less than 0.0015% [152]. Aziz et al. introduced two quaternary ammonium salt groups containing aliphatic chains in the ferrocene structure [153]. The solubility of the new ferrocene molecule BTMAP-Fc in water was 1.9 mol/L, and the theoretical capacity was 50.9 Ah/L. When the concentration of the active material is in the range of 0.75–1.00 mol/L, the AORFB showed good cycle stability, and the capacity retention rate of each cycle was as high as 99.9989%.

4 Redox flow battery electrode mechanism

As the core component of redox flow battery, the electrode supports variable functions, which mainly include four sections: the supply of active sites for redox reactions, the pathways for mass and charge transports, the distribution of anolyte and catholyte throughout the reaction zone, and the buffering of mechanical compression which is necessary for the sealing system to minimize the contact resistance between adjacent components [154].

Carbon felt is made from carbon fiber, with the benefit of high

surface area and porosity, great electrochemical efficiency, and mechanical stability, while it costs relatively low, thus being considered a reliable electrode choice. Since the physiochemical processes in the electrodes affect the activation, Ohmic, and concentration losses a lot [155], it is important to get a whole picture of the mechanism of redox reactions in the electrodes to develop stable and reliable electrodes.

4.1 Model constructing method

The chemisorption mechanism is a significant part of the electrode mechanism. Compared with scientific experiments, microscale simulation is widely used to explore diffusion, sorption dynamics, viscosity, thermal conductivity, structural stability, and reaction mechanism due to its low costs, high security, and high precision demonstrating how the internal connection among the reactants impacts the kinetic, thermal, structural, and chemical properties. The kinetic and thermodynamics of the sorption, diffusion, and chemical reactions can be studied through the simulation. Here, molecular dynamics (MD) and DFT are two fundamental simulation choice methods.

4.1.1 Molecular dynamics

MD is a simulation tool that predicts and estimates related properties for interacting particles (atoms, molecules, etc.) system with time evolution. MD simulation can be reached by a set of classical Newtonian equations of motion for all particles based on the appropriate selection of interaction potentials, numerical integrals, and periodic boundary conditions.

MD simulation has been used to study the internal interactions between ions and molecules in the electrolyte. Ge et al. detected the cumulative penetration of Br through the negative electrolyte in a benzoquinone/bromo RFB by a spectrophotometer and a special reagent and clarified the crossing behavior of Br⁻ and Br₂ using MD simulation [156]. The results showed that the cross of Br is the key factor in decreasing the current efficiency, and the electric field is applied to reduce the Br⁻ cross.

4.1.2 Density functional theory

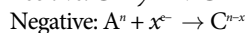
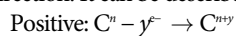
DFT has become hot research nowadays, which is widely used to study the bonding condition, adsorption structure, and the related properties of atoms based on the Schrodinger equation. Properties of atoms or molecules, such as electron transfer mechanisms, reaction pathways, bond energy, bond angle, activation energies, and chemical stability, can be acquired based on the energy minimization principle by calculating the well-setting structures.

The structure of the activated reactants can be revealed through DFT computations. Vijayakumar et al. studied the vanadium (V) structure in mixed acid-based electrolyte solution by DFT calculation and NMR spectroscopy [157]. It showed that the chlorine-bonded binuclear 2P compound is more favorable to formation than the original binuclear 4P compound. The increase in temperature promotes the forming of the chlorine-bonded binuclear compound through a ligand exchange process. Therefore, V⁵⁺ has high thermal stability in a mixed acid system.

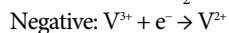
DFT calculations can also be addressed to display the synergistic effect of the active ions. Yeonjoo et al. studied the addition of electrocatalyst Bi to ICRFBs [86]. Combined experimental analysis and DFT calculations indicate that the improving electrochemical performance of the flow battery is ascribed to the synergistic effects of Bi and KB (Kochenblack), which inhibit hydrogen evolution and provide active sites for the Cr²⁺/Cr³⁺ redox reactions that mainly impact the efficiency of the ICRFB.

4.2 Reaction mechanisms in traditional carbon-based electrode

It is widely acknowledged that negative and positive electrolytes flow through the negative and positive electrodes, where the electrolytes support active species and the redox reactions occur (Fig. 13(a)), thus forming internal loops in the cathode and anolyte. During the charging process, positive active species lose several electrons and are oxidized, while negative active species gain several electrons and are reduced. The total number of the gained and lost electrons are the same in the positive and negative reactions based on the law of conservation of mass. During the discharge process, the chemical reaction occurs in the opposite direction. It can be described as follows:



Giving the VFBs as an example. As the VFBs is the most mature flow battery, which has been put into use, and the electrochemical reactions mechanism of VFBs can be described as follows:



C-OH functional groups of carbon-based electrodes affect the redox reaction process a lot. One of the widely acknowledged mechanisms of how the C-OH functional groups on the surface of the carbon-based electrode participate in the VO²⁺/VO₂⁺ redox reaction during the charging process are explained as follows: (i) Ion exchange happens when VO²⁺ from electrolyte meets H⁺, which is separated from C-OH. (ii) The hydroxyl group in H₂O reacts with VO²⁺ in electrolyte and the rest H⁺ in the H₂O generates. (iii) VO²⁺ turns into VO₂⁺ in the electrode through electron conduction, while H⁺ is desorbed from -OH. (iv) Ion exchange happens when VO₂⁺ in the electrode meets H⁺ from the electrolyte (Fig. 13(b)) [158].

The discharge process is similar to the charging process, in which reactions occur in the opposite direction and are depicted as follows: (i) Ion exchange happens when V³⁺ from electrolyte meets H⁺, which is separated from C-OH. (ii) V³⁺ turns into V²⁺ in the electrode through electron conduction. (iii) Ion exchange happens when V²⁺ in the electrode meets H⁺ from the electrolyte (Fig. 13(c)) [158].

4.3 Reaction mechanisms in metalloid elements doped electrode

4.3.1 O-doped electrode

The reaction mechanism on the surface of the oxygen-doped electrode of the VFB was first studied by Skyllas-Kazacos, who measured the efficiency of the untreated and thermal-activated VFB [159]. After the graphite felt was thermo-treated, they found that the electrode was activated, demonstrating a massive enhancement in the electrochemical efficiency. They found that the amount of oxygen groups was sorbed on the surface of the electrode, which was mainly composed of two oxygen-containing functional groups, C-O and C=O, that are considered normally to be hydroxyl and carboxyl through X-ray photoelectron spectroscopy (XPS) analysis. Thus, they attributed the increased activity to the two functional groups on the felt surface and considered that the C-O groups act as active sites to catalyze the redox reactions.

The mechanism of vanadium redox reactions occurring on the oxygen-doped electrodes is depicted as follows: (i) VO²⁺ ions are

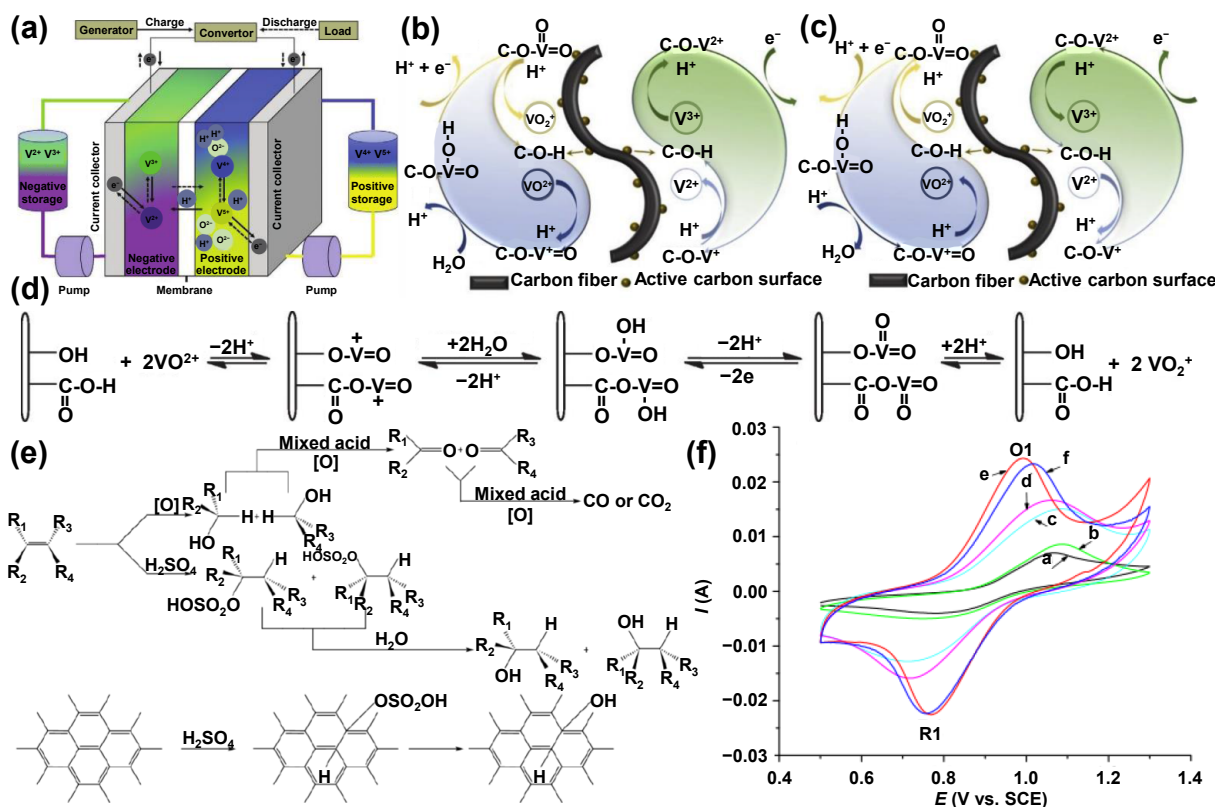


Figure 13 (a) Schematic of the VFB system. Reproduced with permission from Ref. [161], © WILEY-VCH Verlag GmbH & Co. KGaA, Weinheim 2020. (b) and (c) Mechanisms of the redox reaction during the charge process and discharge process. Reproduced with permission from Ref. [158], © Elsevier B.V. 2020. (d) The reaction mechanism on the oxygen-doped electrodes. Reproduced with permission from Ref. [162], © Elsevier Ltd. 2012. (e) Mechanism of mixed-acid-catalyzed oxidation to form active functional groups on carbon felt. (f) CV curves were recorded in the mixed acid solution at untreated carbon paper electrode, and carbon papers were treated under different ultrasonication times for 0.5, 2, 5, 8, and 10 h. Reproduced with permission from Ref. [160], © Elsevier Ltd. 2010.

sorbed to the electrode surface from the solution, and ion exchange occurs between VO^{2+} ions and the functional groups (hydroxyl and carboxyl) on the graphite surface, thus bonding onto the electrode surface. (ii) Electron transfer occurs along the $-\text{C}-\text{O}-\text{V}-$ bond, while the oxygen atom is separated from the $\text{C}-\text{O}$ functional group, and the VO^{2+} ion forms a surface VO_2^+ . (iii) After the VO_2^+ and the H^+ exchange ions with each other in the electrolyte, the oxidation reaction is terminated (Fig. 13(d)).

In addition to thermal treatment, acid treatment helps introduce oxygen atoms to the electrode surface, increasing the active sites. Lu et al. hydroxylated carbon paper with H_2SO_4 and HNO_3 to introduce oxygen atoms [160]. They suggested that the deep oxidation of phenolic groups will lead to the formation of the keto groups since the $\text{C}-\text{C}$ bonds are broken under strong oxidation. The mechanism of the reactions between electrodes and mixed acids can be described as follows: when the reaction begins, a minority of the $\text{C}-\text{C}$ bonds are broken to form AOH with the oxygen-containing groups. When oxidizing further, a huge amount of the $\text{C}-\text{C}$ bonds are broken and form AOH groups, and $\text{C}=\text{O}$ groups are easily generated from the further oxidation of AOH. At the same time, the H_2SO_4 molecule can attack the defect sites to form $\text{C}-\text{OSO}_2\text{OH}$, which transforms into AOH when meeting H_2O . It can also protect the $\text{C}=\text{C}$ from destruction (Fig. 13(e)). Besides, CV tests were conducted to demonstrate the relationship between electrochemical activity and the concentration of AOH groups. Figure 13(f) shows that the peak currents of the oxidation and reduction reactions both increase with the increase of the AOH group content. The improving electrochemical performance and the excellent activity towards the

V(IV)/V(V) reaction result from the higher concentration of AOH groups on the surface of the electrode.

Another possible reaction model on the oxygen-doped electrode has been proposed to depict the mechanism further. Wu et al. proposed an inner-sphere model to explain the mechanism for the vanadium redox reaction on the CP electrode [163]. As shown in Fig. 14(a), (I) shows that the $[\text{V}=\text{O}]^{2+}$ group releases an electron and forms $[\text{O}=\text{V}=\text{O}]^+$ by releasing two protons. (II) shows the way that the VO^{2+} group reacts with the VO_2^+ group to form a mixed-valence $\text{V}_2\text{O}_3^{3+}$ species, which has a fast speed of electron transfer with VO^{2+} groups. (III) and (IV) demonstrate that the reaction occurs through an inner-sphere species. Necessary infrared absorption tests were conducted to reveal that carbonyl and hydroxyl groups increase after acid treatment, demonstrating that oxygen is involved in the electrode mechanism. Singh et al. observed the conversion of $\text{C}-\text{OH}$ to $-\text{O}-\text{C}=\text{O}$ groups after the degradation in the CP electrodes, leading to a significant loss in performance during the operation [164]. They attributed the efficiency loss to the decrease of the active sites provided by the hydroxyl groups since the interaction with the electrolyte at the electrode promotes the reduction of hydroxy groups and their conversion to carboxyl groups.

First-principle studies have been addressed to reveal the internal interactions between the vanadium ions and oxygen ions on the electrode surfaces from the atomic level. Jiang et al. analyzed the projected density of states (PDOS) for the most stable inner-sphere structures of the O atoms at the edges [165]. The simulation result showed that the 2p state is the main hybridization of the oxygen atom, while the 3d state is that of the

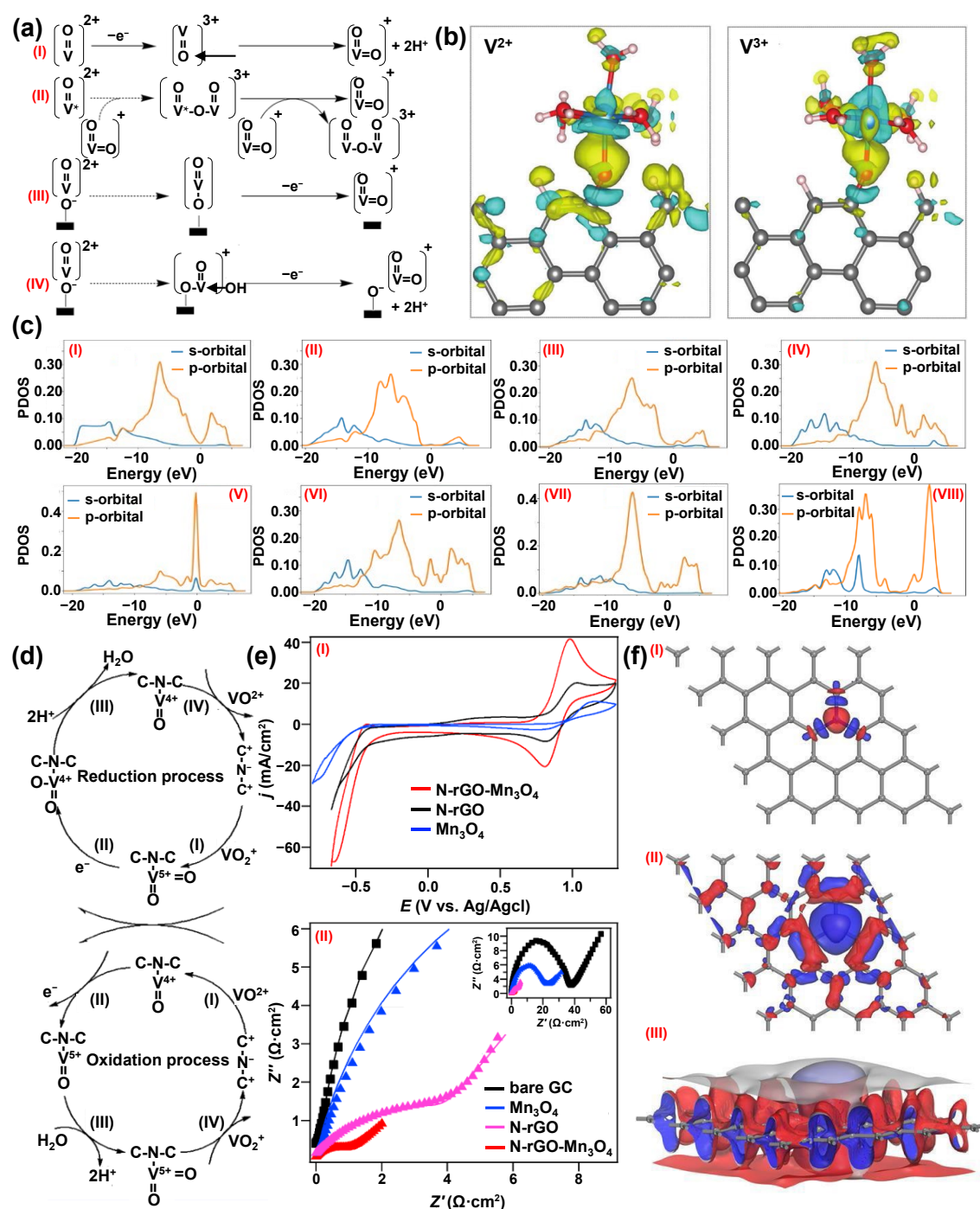


Figure 14 (a) Rapid electron exchange mechanisms for the reaction of the VO_2^+/VO_2^- on the surface of a carbon paper electrode. Reproduced with permission from Ref. [163], © Springer Science + Business Media B.V. 2011. (b) EDDM of the inner-sphere structure of the V^{2+}/V^{3+} species on the carbon electrode, in which the yellow and green parts represent the rise and fall of the electron density, respectively. Reproduced with permission from Ref. [165], © The Owner Societies 2017. (c) PDOS graphs of (I) BG, (II) BG-OH, (III) BG-O, (IV) BG-D-H, (V) BG-D, (VI) BG-D-OH, (VII) BG-D-O, and (VIII) BG-D-COOH. Reproduced with permission from Ref. [166], © Wiley-VCH GmbH 2021. (d) Proposed reaction mechanism on the surface of N-doped electrodes. Reproduced with permission from Ref. [50], © American Chemical Society 2013. (e) (I) The CVs recorded at N-rGO-Mn₃O₄, N-rGO, and Mn₃O₄ modified GC electrodes and (II) Nyquist plots acquired applying the electrodes illustrated in (I). Reproduced with permission from Ref. [170], © American Chemical Society 2015. (f) The visualized electron density model of N-doped graphene and the structure that the carbon atom has been replaced by nitrogen atom with the isosurfaces: (I) $\pm 50 e^-/nm^2$, (II) $\pm 5 e^-/nm^2$, and (III) $\pm 0.02 e^-/nm^2$. The red color represents charge concentration, while the blue color represents charge depletion. Reproduced with permission from Ref. [171], © Elsevier Ltd. 2016.

vanadium atom, which is beneficial for electron transfer. Electron density difference maps (EDDM) are shown in Fig. 14(b), demonstrating that the electron density increases along the V–O bonds. This also proves that oxygen sites promote electron transfer through the surface. Hassan et al. evaluated the oxygen functional groups' role in the redox reaction of VFBS based on

DFT calculation [166]. PDOS calculation (Fig. 14(c)) showed that the oxygenic groups enhance the affinity of the electrode towards the vanadium ions redox reactions, resulting from the increase of oxygenic groups leading to an increasing sp^3 hybridization, which mainly affects the improvement of the electroactivity.

4.3.2 N-doped electrode

Nitrogen-doped graphite felt is reported to have great electrocatalytic capability, thus being widely studied. Zhang et al. synthesized nitrogen-doped electrodes for VFBs, which exhibited excellent electrochemical activity with a relatively low inner resistance and a high efficiency [50]. Further study demonstrated that several N-doped types exist in nitrogen-doped electrodes: graphitic-N, pyridinic-N, pyrrolic-N, and oxidized-N. The pyridinic-N without a lone electrons pair has a more stable structure in the solution since the solution is acidic, and the pyridinic-N is not easily influenced by protonation. Therefore, the pyridinic-N atoms act as active sites for the $[\text{VO}]^{2+}/[\text{VO}_2]^+$ redox reaction [167], which meets the DFT calculation conducted by Ni et al. [168]. Figure 14(d) shows the reaction mechanism for vanadium redox reactions on the N-doped electrode proposed by Zhang's work. During the charging process: (i) The vanadium ions ($\text{VO}^{2+}/\text{V}^{3+}$) and the nitrogen atoms combine with each other to generate the N-V bond. (ii) Electron transfer occurs through N-V bonds during the redox reaction. (iii) The additional electron in the antibonding orbital of VO_2^+ weakens the V=O bond and removes one of the oxygens with two protons. (iv) The reaction products ($\text{VO}_2^+/\text{V}^{3+}$) diffuse back to the solution through the ion exchange. The discharge process is the opposite [50].

The improving electrochemical performance may be attributed to the decreasing resistance caused by the doped nitrogenous groups. Wu et al. used the hydrothermal ammonia method to treat graphite electrodes [169]. EIS result showed a significant decrease in charge-transfer resistance, which is ascribed to the doping of nitrogenous groups on the electrodes. They suggested that based on the Stern double layer theory, the sorption of the vanadium ions on the surface of the graphite felt leads to decreased dispersion layer thickness and increased electrode capacitance. Nitrogenous groups provide lone pair electrons with high charge density due to the edge effect, which enhances the electrical conductivity, explaining the decrease of the resistance.

Some studies have been addressed to illustrate that metal-nitrogen-carbon interaction is beneficial to enhance the performance of the electrocatalyst. Ejigu et al. studied the electrocatalytic activity of a composite N-doped, reduced graphene oxide/ Mn_3O_4 electrocatalyst (N-rGO- Mn_3O_4) in the VFB through CV and EIS [170]. The CV and EIS results (Fig. 14(e)) demonstrate that N-rGO- Mn_3O_4 electrodes have a better electrochemical performance than the N-rGO electrodes, which can be attributed to the synergy of the electrons in the electrodes due to the Mn-N-C bond formed in N-rGO- Mn_3O_4 . While the nitrogen atom substitutes for the carbon atom and is doped into the carbon framework, the synergistic effect is relatively obvious, demonstrating that the interaction among metal, nitrogen, and carbon is important to the redox reaction.

To further reveal the catalytic mechanism of nitrogen doping, Adolfo et al. built the possible chemisorption model for the redox reaction and estimated the stability of the possible reaction model through DFT calculation, leading to the result that when the hydrogenated pyridinic nitrogen is fixed at the armchair edge of the structure, molecular oxygen presents monodentate chemisorbed states, which is quite advantageous for chemisorption [171]. A model to express the mechanism of graphitic nitrogen dopants is proposed in Fig. 14(f). Their work should be helpful in designing and evaluating the nitrogen-doped electrodes in the redox flow battery.

DFT computations were also used to estimate the absorption model of the nitrogenous groups. Xu et al. estimated the

adsorption energy for $\text{V}^{2+}/\text{V}^{3+}$ on various N-doped carbon electrodes through DFT calculation [172]. They considered the inner-sphere adsorption and outer-sphere adsorption model and found that graphitic-N-doped graphene benefits the inner-sphere absorption structure for V^{2+} . In contrast, pyridinic-N-doped graphene tends to enhance the electrochemical performance towards V^{3+} . The simulation result proves that the electrode doped with different nitrogen functional groups may have a massive influence on the redox reaction.

4.3.3 P-doped electrode

Through phosphorous doping, the atomic spacing in the carbon framework between the carbon atoms and the heteroatom varies due to the change in charge distribution. The hydroxyl groups on the surface of the electrode form active functional groups with phosphorous atoms, thus promoting ion exchange. The reaction mechanism for vanadium redox reactions on the P-doped electrode with rich oxygen is studied in depicted as follows: (i) During the charging process, VO^{2+} and V^{3+} ions are transferred from the solution to the surface of the electrode and caught by the hydrogen ions in phosphorous groups. (ii) Redox reaction happens with the electron conduction on the active site provided by the phosphorous functioning groups through the P-O-V bond. VO^{2+} becomes VO_2^+ on the positive electrode during the redox reaction, while on the negative part, V^{3+} becomes V^{2+} . (iii) The reaction products diffuse back into the solution through ion exchange. The discharge process is the opposite.

Electrochemical treatment is adopted to dope phosphorous atoms on the graphene to improve the electrocatalytic performance of the electrode. Hurmus et al. treated P-doped graphene electrodes (PGE) in the phosphoric acid solution, used CV to prepare P-GPGEs, and tested the electrocatalytic activity toward redox actions [173]. They found the generation of the graphene layers resulted from the separation of the graphite layers (Fig. 15(a)) because the acid treatment and the anodic potentials provide excellent conditions for the rapid production of active functional radicals and defects, which leads to the promotion of the redox reaction. The result of CV tests illustrated that an increased number of cycles led to a highly enhanced electrochemical performance of the VFB since more phosphorous functional groups are generated with the increase of electrochemical treatment times, which brings better wettability and more defects. Besides, the graphene layers generated on the electrode surface are likely to improve the electronic conductivity, thus promoting the electrochemical performance of the battery.

The stable chelating groups formed by phosphorous groups and vanadium ions should be the key to the marvelous electrocatalytic performance of the phosphorous-doped electrode. Noh et al. synthesized phosphorylethanolamine doped carbon nanotube (POH-CNT) catalysts and compared their performance in VFB with that of the carboxylic acid functionalized CNT (CA-CNT) catalysts [174]. The electrochemical test and DFT calculation showed that the POH-CNT has a better catalytic capability towards the redox reaction than the undoped nanotubes since the phosphate functional groups can react with vanadium ions to form stable chelating active functional groups with a relatively low electron delocalization capability. Due to the generation of the chelating groups, the active sites in the POH-CNT increase. The catalytic mechanism proposed in Fig. 15(b) can be described as follows: VO^{2+} firstly is sorbed on the surface of the P-doped electrode through ion exchange, then the hydroxyl

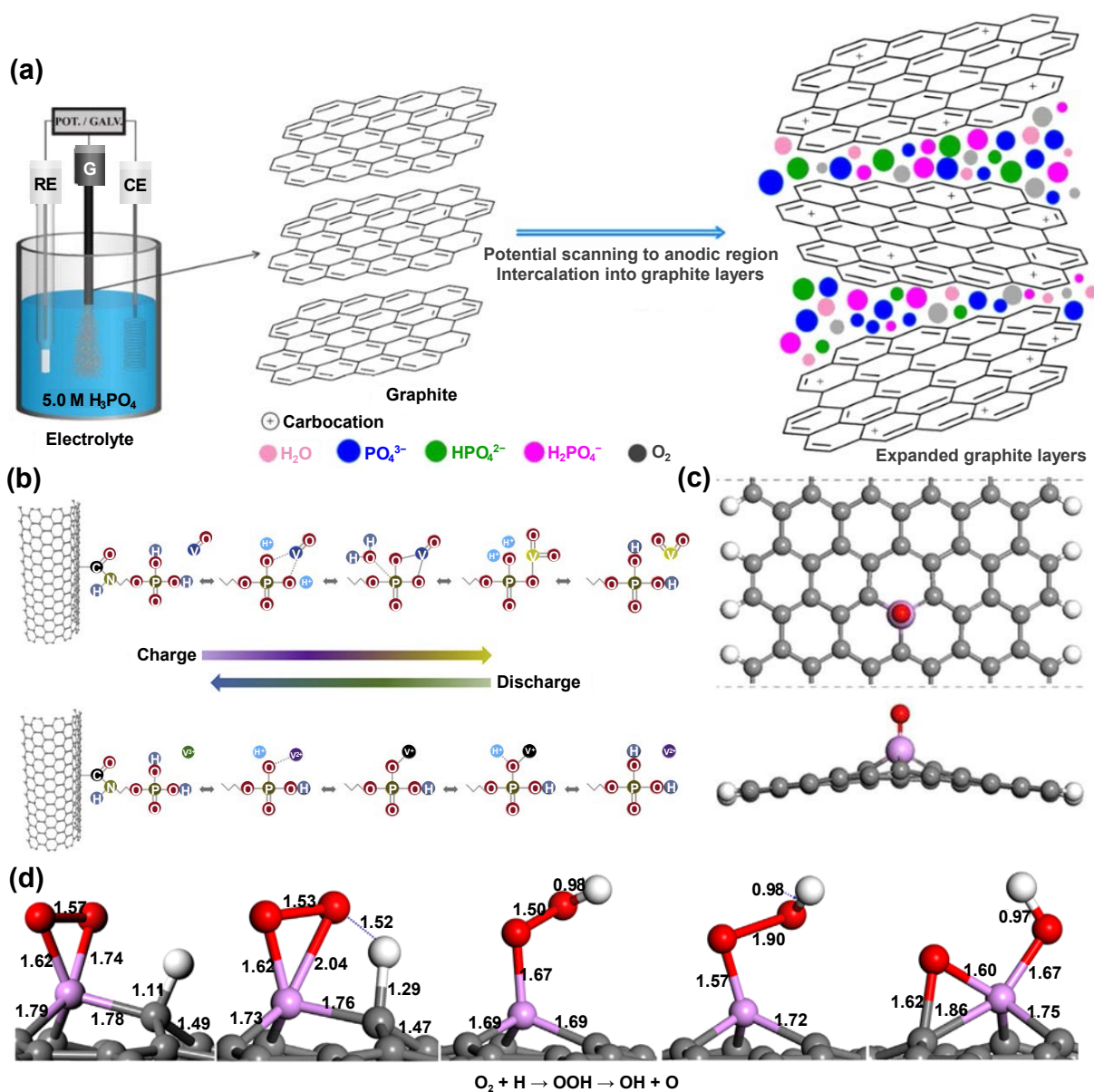


Figure 15 (a) Proposed mechanism of phosphate ions to graphite. Reproduced with permission from Ref. [173], © The Electrochemical Society (“ECS”). Published on behalf of ECS by IOP Publishing Limited 2021. (b) Proposed mechanism of the vanadium redox reaction mechanisms catalyzed by POH-CNT. Reproduced with permission from Ref. [174], © Elsevier B.V. 2018. (c) Top and side views for the proposed OPC₃G structure. The grey, white, red, and pink spheres visualize the C, H, O, and P atoms. Reproduced with permission from Ref. [175], © American Chemical Society 2017. (d) Formation and decomposition of the active functional group OOH. Reproduced with permission from Ref. [176], © Elsevier B.V. 2014.

bonds in the phosphate group dissociate protons to combine with VO²⁺ ion and form a new functional group connected by the covalent bond among them. Then water ions coordinate with the phosphate group to form a ligand. Due to the spatial effect, the oxygen atom is separated from the phosphate group and interacts with the VO²⁺ ion, forming the VO₂⁺ ion. The VO₂⁺ ion diffuse back into the electrolyte. The discharge process is the opposite.

The simulation model is built, and DFT calculation is addressed to reveal the redox reaction’s sorption mechanism. Yang et al. measured the influence of phosphorous group composition on the electronic structure and the possible reaction pathways of P-doped graphene by DFT computations [175]. The simulation result showed that a P atom can replace a C atom in the carbon framework, forming three P-C bonds. The structure can be easily oxidized, binding with an oxygen atom on the phosphorous atom to generate a P-O bond and form the oxidized P-doped graphene

(OPC3G) absorption model. The OPC3G model shown in Fig. 15(c) has strong stability and plentiful potential active sites, thus becoming the most credible P-doped graphene structure for the ORR. Zhang et al. investigated the ORR mechanism on the P-doped graphene using the DFT computations [176], indicated that the reaction efficiency of the ORR can be enhanced a lot because the phosphorous atom doped on the graphene can influence the electronic structure significantly. The Hirshfeld population analysis was conducted to investigate the reaction activity of PGr toward the ORR. The results showed that the P atom loses about 0.21e⁻ and the electron transfer occurs between the P atom and the C atom around the P atom, revealing that the P atom and C atoms around it are the active sites for the ORR. The proposed mechanism is shown in Fig. 15(d). DFT calculation could explain the mechanism of the adsorption of phosphorous atoms on the GF and the mechanism of the generation of the active sites in the RFBs.

4.3.4 B-doped electrode

The reaction mechanism on the surface of the boron-doped electrode has been studied and ascribed to the formation of B–O–V covalent bonds. David et al. synthesized 3D boron-doped mesoporous graphene functionalized carbon felt (BMG-CF) as the electrode of VFBS. The proposed reaction mechanism on the BMG-CF is depicted in Fig. 16(a) [177]. During the charging process, the oxygen atom with a negative charge binds with the boron atom connected with covalent bonds and then interacts with vanadium ions with a positive charge (VO^{2+} and V^{3+}) to form a B–O–V bond. At the same time, a proton is diffused back into the solution. VO^{2+} is oxidized to VO_2^+ , while V^{3+} is reduced to V^{2+} during this process, and then the reaction products desorb back into the electrolyte. The mechanism is the opposite during the discharge process.

The great electrocatalytic capability of the boron-doped electrode is ascribed to the high electronegativity of the boron atom revealed by the DFT calculation. Jiang et al. studied the underlying mechanism of B-doped electrodes for vanadium redox reactions through DFT calculation [178]. They found from Figs. 16(b)(I) and 16(b)(II), that the electron vacuum around the boron atoms is relatively high because the boron atom has a lower electronegativity compared with the carbon atom, leading to the fact that the inert electrons have fewer constraint forces, so that the catalytic activity would be enhanced and the reaction would be promoted. Besides, Figs. 16(b)(III) and 16(b)(IV), show that the B-doped electrode has a higher energy barrier (12.4 eV) than –OH, demonstrating that the B-doped graphite felt highly activated and stabilized reaction sites.

Another possible mechanism has been addressed to explain the reaction process. Park et al. prepared B-doped carbon felt electrode for enhancing the electrochemical performance of VFBS [179]. CV result showed a remarkable improvement in the efficiency of the B-CF electrodes compared to that with CF, whose EE increased from 63.40% to 80.56%, attributing to the introduction of boron atoms. The reaction mechanism on the B-CF was proposed in Fig. 16(c). It could be depicted as follows: during the charging process in the catholyte, VO^{2+} ions are transferred from the electrolyte to the surface of the modified electrode and then combined with the two –OH groups in the BCO_2 functional group during ion exchange, while BCO_2 exchange hydrogen ions with VO^{2+} near the surface of the electrode. H_2O in the electrolyte is then combined with the VO^{2+} ions, which are combined with BCO_2 . Finally, VO^{2+} changes into VO_2^+ , and BCO_2 remains on the surface of the B-CF through cation exchange in the catholyte. The reaction happening in the anolyte is similar to that in the catholyte. The reaction goes in the opposite direction in the discharge process.

4.3.5 Co-doped electrode

The co-doped electrode usually exhibits a better electrocatalytic performance than the mono-doped electrode since the co-doped electrode can combine the advantages of the mono-doped electrodes, thus being widely studied nowadays. Shi et al. synthesized co-doped carbon nanofiber as the reaction substrate for the $\text{VO}^{2+}/\text{VO}_2^+$ redox reaction with boron and nitrogen atoms [180]. The co-doped electrode demonstrated a massive catalytic

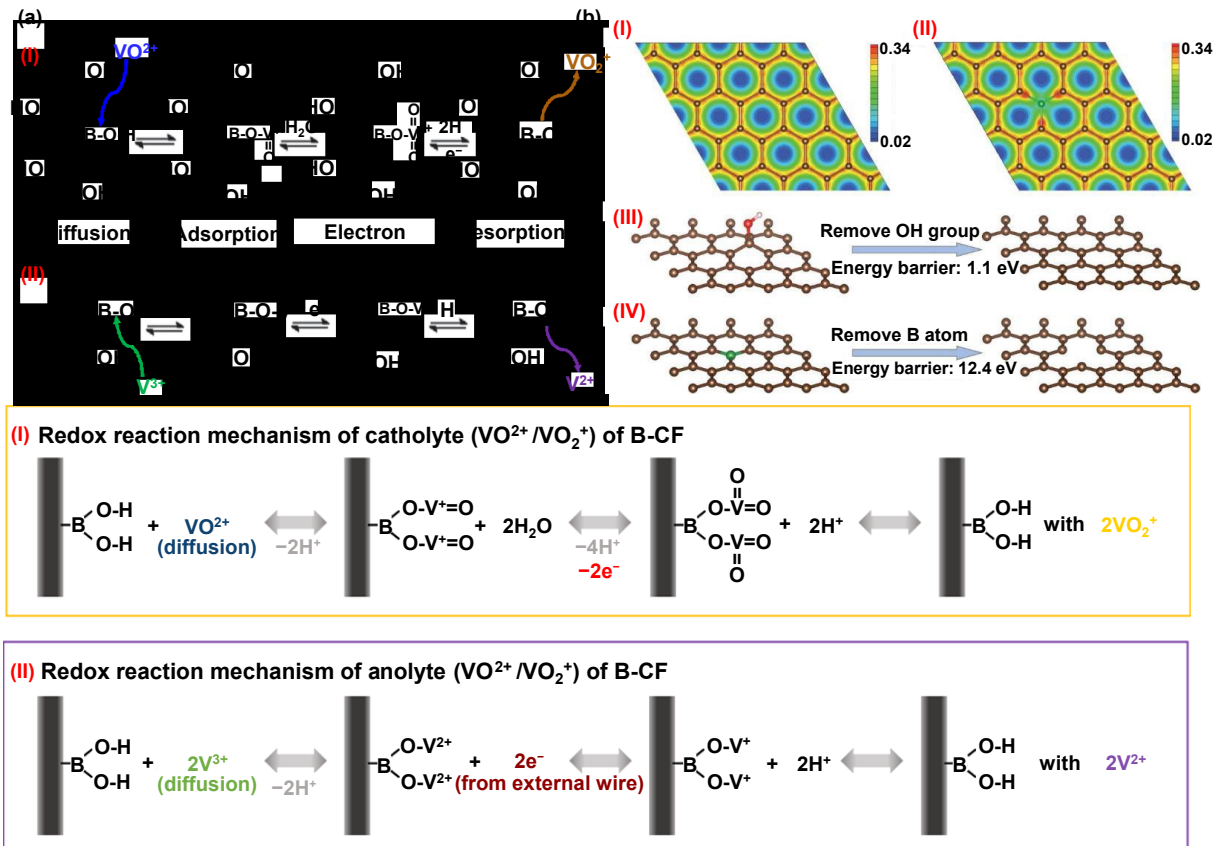


Figure 16 (a) Redox reaction mechanism on the surface of BMG-CF electrodes. Reproduced with permission from Ref. [177], © Elsevier Ltd. 2021. (b) The simulating structures and the electron density distribution of the (I) pristine graphite (0001) surface and (II) boron-doped graphite (0001) surface. The energy barriers after removing the (III) OH group and (IV) boron atom from carbon surfaces. The brown, green, red, and white balls represent the carbon, boron, oxygen, and hydrogen atoms. Reproduced with permission from Ref. [178], © The Royal Society of Chemistry 2018. (c) Proposed mechanism of redox reaction on the surface of B-CF electrode in (I) the catholyte and (II) the anolyte. Reproduced with permission from Ref. [179], © Elsevier B.V. 2021.

activity, which was better than either the boron or nitrogen monodoped case because the boron atom can form the bond of C–B–C, which plays an important role in activating the π electron to improve electron transfer kinetics, and the nitrogen atom can introduce a number of active sites containing nitrogen atoms to the surface of graphite to accelerate the mass transfer rate. The proposed reaction mechanism occurring on the co-doped electrodes is shown in Fig. 17(a).

Su et al. prepared P-doped carbon nitride-modified graphite by solvothermal and calcination process [181], which exhibits excellent wettability and electrocatalytic activity, reaching 616.2 mW/cm² of power density. The mechanism is proposed in Fig. 17(b). Firstly, ion exchange transfers VO³⁺ (V³⁺) ions to the surface of the modified electrode. Then, the ions are sorbed on the electrode, generating P–O–V and N–V bonds through the covalent bonds. Thirdly, electronic conduction occurs, and the redox reaction generates the oxidation product VO₂⁺ (reduction product V²⁺). Finally, the VO₂⁺ (V²⁺) desorbs and is transferred back into the electrolyte through ion exchange. The forming of P–O–V and N–V bonds on the surface may be the rate-limiting step, which helps accelerate the reaction of VO²⁺/VO₂⁺ and V²⁺/V³⁺ (Figs. 17(c) and 17(d)).

4.3.6 Carbon-nanocatalyst-supported electrode

Carbon nanotubes introduce a high specific surface area and rich

catalytically active functional groups, improving electrochemical activity. The hydro and carboxyl groups on the nanotubes activate the redox reaction in VFBS since the redox reaction process of VO₂⁺/VO²⁺ involves the transfer of an oxygen atom. Carbon nanotubes provide carboxyl, which can be desorbed from the functional group and replaced by VO₂⁺ more easily than the hydroxyl group so that it can enhance the efficiency of the redox reactions. Li et al. hypothesized that the reaction mechanism was Fig. 18(a), in which the transfer of oxygen atoms is likely to be the speed-limiting step in the overall mechanism [182].

The advantageous structure of carbon nanotubes improves the electrochemical performance of flow cells. Gonzalez et al. prepared a single-walled carbon nanotube thin membrane [183]. They found that the interconnected networks of two-dimensional (2D)-graphene nanostructures show a great electrochemical response toward the redox reaction. CV test showed that the peak currents ratio is greater than unity, which is related to a chemical reaction–electronic transfer–chemical reaction (CEC mechanism) that can be explained by the mechanism proposed for the V⁴⁺/V⁵⁺ reactions (Fig. 18(b)).

Han et al. prepared composite electrodes of multi-walled carbon nanotubes (MWCNTs) and graphite oxidized by electrostatic injection and found an improvement in electrochemical reversibility [184]. They attributed the

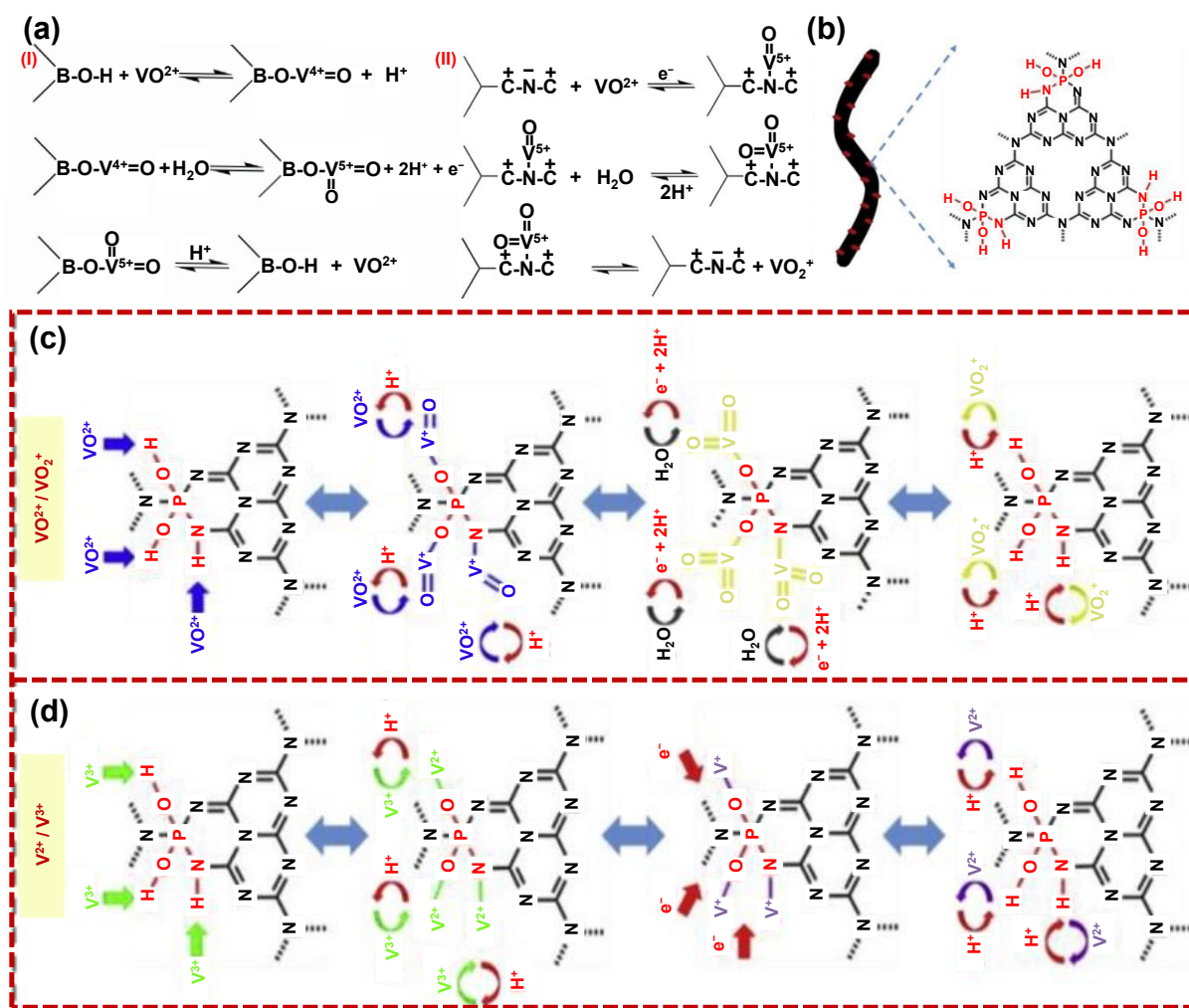


Figure 17 (a) Proposed mechanism of N-doping for the VO²⁺/VO₂⁺ redox reaction. Reproduced with permission from Ref. [180], © Elsevier Ltd. 2015. (b) Schematic of the P-C₃N₄@GF. (c) Proposed positive reaction mechanisms of P-C₃N₄@GF. (d) Proposed negative reaction mechanisms of P-C₃N₄@GF. Reproduced with permission from Ref. [181], © Elsevier Ltd. 2018.

enhancement to the fact that the VFB with the modified electrode has a fast speed of ion exchange and electronic conduction characteristics since GO/MWCNTs have a cross-linked structure and a strong electron-conducting network resulting from the electrocatalytic hybrid. The reaction mechanism presumed by them, which is quite correlated to the concentration of hydroxyl functional groups, is similar to the mechanism reported by Sun and Skylas-Kazacos [159].

DFT calculation has been addressed to study the catalytic mechanism of the carbon-nanotube-doped electrodes. Chaudhuri et al. estimated various nanotubes of carbon, boron, and nitrogen with different configurations and values of tube diameters through DFT calculation [185]. The model of the zigzag nanotube and the armchair nanotubes for the three configurations is shown in Fig. 18(c). They observed that the nanotube stability is positively correlated with the nanotube diameters. The minimized diameter of the stable CN nanotubes is 3.03 Å. For BN nanotube, it demonstrated semiconducting characteristics with small band gaps, which would vary depending on the change of its configuration like diameter and chirality. Only with a small diameter could CN nanotubes exhibit semiconducting

characteristics. Their work has guiding significance when researchers prepare nanotube-doped electrodes to increase the efficiency of the RFBs.

The distribution of the electrons greatly influences the electrocatalytic activity of the nanotube electrode. Jiang et al. used B₄C nanoparticles to modify GF as metal-free catalysts [186]. The first-principle calculation was adopted to illustrate that the B₄C has a mass of unpaired electrons around the center, which leads to the nonuniform distribution of electrons shown in Fig. 18(d) and helps enhance the electrochemical performance of the reaction. Therefore, it is presumed that the carbon atoms with the lower electron density area around the boron atoms can act as active sites to promote the reaction.

4.4 Reaction mechanisms in metal-modified electrode

Metal ion doping improves the conductivity of graphite felt by coating metal particles, metal oxide particles, and metal ions such as platinum, lead, gold, manganese, and bismuth on the surface. Early reports use noble metals Pt, Ir, etc., for modifying vanadium battery electrodes [187, 188]. However, the high price limits their practical application.

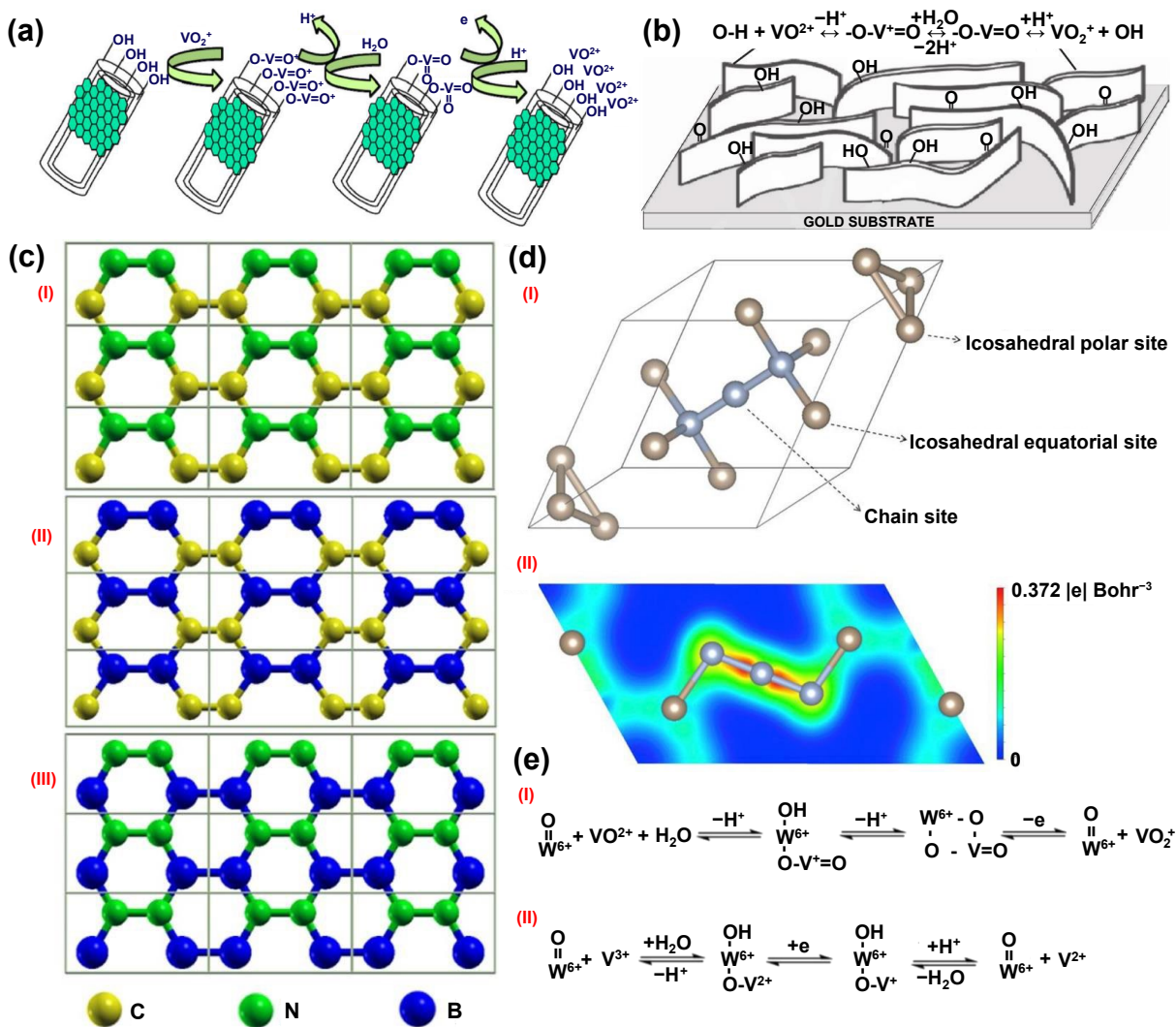


Figure 18 (a) Proposed mechanism of the carbon nanotubes. Reproduced with permission from Ref. [182], © Elsevier Ltd. 2011. (b) Proposed mechanism of the redox reactions on three carbon nanowalls (CNWs) thin membrane. Reproduced with permission from Ref. [183], © Elsevier Ltd. 2012. (c) The structure of the doped graphene-like layer: (I) CN, (II) CB, and (III) BN. Reproduced with permission from Ref. [185], © Elsevier B.V. 2019. (d) (I) Proposed structure of B₄C unit cell. The brown and blue balls represent boron and carbon atoms, respectively. (II) The electron density contour of the B₄C (110) surface. Reproduced with permission from Ref. [186], © Elsevier B.V. 2017. (e) Proposed mechanism of WO₃/SAC towards the redox couples. Reproduced with permission from Ref. [189], © Elsevier B.V. 2012.

With the increasing demand for battery performance, Bi-functional metal-modified electrodes are studied and synthesized to enhance the overall performance of flow batteries [189]. Yao et al. synthesized carbon paper electrode covered with supported WO_3 for VFBS, demonstrating massive electrochemical activity towards the reactants, attributing to the fact that WO_3 acts as the active center towards the redox reaction, reducing the adsorption difficulty of the reactants [189]. Figure 18(e) indicates the reaction mechanism on the surface of the WO_3 -modified electrode. During the charging process: (i) The H_2O ions are separated into proton ions and hydroxyl ions, then the hydroxyl ions and VO^{2+} ions bind with the $\text{W}=\text{O}$ by covalent bonding; (ii) the proton is separated from the hydroxyl group and diffused into the electrolyte; (iii) electron conduction occurs while the redox reaction happens, and the product (VO_2^+) is formed and then diffused back into the electrolyte through ions exchange. The mechanism is opposite during the discharge process. Tungsten trioxide can form $-\text{W}^{6+}=\text{O}$ on the surface, which can be the key factor in improving electrochemical activities. So the composite can show excellent performance for vanadium batteries.

The synergistic effect of the metal atoms has a strong impact on the redox reaction. Ahn et al. proposed the KB electrode embedded with Bi in ICRFBs [76]. The result showed that the Bi-KB electrode maintained excellent electrochemical activity and reversibility, improving the peak current and decreasing the resistance. A proposed reaction mechanism on the surface of Bi-C was presumed shown in Fig. 19(a). During the charging process, the reaction may form intermediate compounds of BiH_x , which compete with the formation of hydrogen, thus delaying the reduction of H^+ and suppressing the generation of H_2 . At the same time, the plentiful oxygen-containing functional groups provide a number of active sites to improve the $\text{Cr}^{2+}/\text{Cr}^{3+}$ redox reaction. The massive electrocatalytic performance is ascribed to the synergistic effect of Bi and KB.

Huge amounts of hydroxyl groups brought by the metal atoms improve the performance of the electrode. Flox et al. prepared graphene as the electrode for VFBS with the support of nano- CuPt_3 electrocatalyst, which reached higher current values than the pristine electrode, leading to better electrochemical performance [190]. The catalytic mechanism is shown in Fig. 19(b) and can be depicted as follows: large amounts of activated vanadium ions are sorbed on the surface of the modified electrode because of the hydroxyl groups brought by the electrocatalyst, thus enhancing the capability of the electronic conduction and oxygen transfer.

Zhang et al. fabricated CeO_2 -decorated GF as the electrode of VFBS. The modified electrode increased the peak current of the redox reaction through the CV test, leading to the enhancement of the reversibility of the redox reaction, and the EE of the decorated electrode was 10.8% higher than that of the pristine electrode at the current density of $200 \text{ mA}/\text{cm}^2$ [191]. The improvement of electrochemical activity was attributed to the active functional groups on the surface of the electrode. The mechanism shown in Fig. 19(c) can be explained as follows: the transformation between the Ce^{4+} and Ce^{3+} occurs, then the active sites are regenerated by removing the hydroxyl groups on them, and the vanadium ions exchange protons with the hydroxyl group on CeO_2/GF surface. Then, a surface VO_2^+ is formed and diffused back into the solution.

5 Novel flow batteries

With the vigorous development of flow batteries, more and more

types of new flow batteries have been invented. Different types of flow batteries have various advantages and can cope with different use needs. Several emerging flow batteries are described below.

5.1 Sodium-sulfur (Na-S) flow battery

Yang et al. first developed a novel Na-S flow battery that uses metallic sodium and non-metallic sulfur elements as electrodes [192]. The new Na-S flow battery offers many advantages, including easy electrode preparation and integration, low energy efficiency loss, and high resistance to metal anode volume changes. The system cost of the Na-S flow battery is less than $100\$ \text{ kWh}^{-1}$. This showed that the battery has great potential in grid-scale energy storage applications. The schematic of a semi-solid-state Na-S flow battery is shown in Fig. 20(a).

Wei et al. reported a sodium-sulfur battery that can operate stably at room temperature. The battery used a microporous carbon-sulfur composite cathode and a liquid carbonate electrolyte containing the ionic liquid 1-methyl-3-propylimidazolium-chl [193]. The cell showed the great reversible capacity and high coarse CE during cycling at a rate of 0.5 C ($1 \text{ C} = 1675 \text{ mAh/g}$). The reversible capacity during battery cycling is up to 600 mAh/g , and the CE is close to 100%.

A charge-enhanced ion-selective membrane for ameliorating polysulfide cross-contamination and poor cycle lifetime defects was developed by Li et al. The polysulfide flow cell using this membrane decreased by only 0.005% capacity over 1200 cycles, with an average of 0.0004% per cycle. A flow cell containing $4.0 \text{ M KI}/2.0 \text{ M K}_2\text{S}_2$ demonstrated stable cycling at 17.9 Ah^{-1} over 500 cycles [194].

Some researchers also pay attention to the sulfur flow batteries of other metal-positive electrodes. Lei et al. described a sulfur manganese oxide reduction flow battery, the use of polysulfide solvent in the battery development process to eliminate the metal dendrite problem of metal manganese batteries, and the battery showed good cycle stability during the operation. The electrolyte cost of this system is as low as $11.00\$ \text{ kWh}^{-1}$. This work broadens the horizon of manganese-based batteries and provides a potential approach for low-cost and long-term energy storage [195].

5.2 Lithium semi-solid-state battery

Wei et al. have developed an unconventional flow battery that circulates cathode/anode slurry consisting of a conductive agent that stores particles of active substance and is dispersed in a high salinity water-electrolyte [196]. Submicron cathode $\text{LiV}_a\text{X}_b(\text{PO}_4)_c$ and anode VO_2 particles are considered ideal active materials for the slurry due to their advantages of high lattice stability and appropriate potential. Aqueous lithium-ion slurry flow batteries (ALISFBs) achieved long cycle life, high CE (close to 100%), and good operating voltage in state-of-the-art waterborne RFBs. A schematic structure of an aqueous lithium-ion slurry flow battery is shown in Fig. 20(b).

5.3 Battery with silicon carbon nanocomposites as electrolyte

Si-C nanocomposite semisolid sea usury was proposed and proved to have great potential in replacing lithium metal in Li-RFBs. Chen et al. prepared a monodisperse Si-C material with ultra-thin (9 nm) graphite carbon coatings [197]. The Si-C nanocomposite melt has been shown to have a good reversible capacity ($> 1200 \text{ mAh/g}$) in Li half-batteries, with high CE ($> 90\%$) and long cycle life (> 100 cycles). By using the Si-C

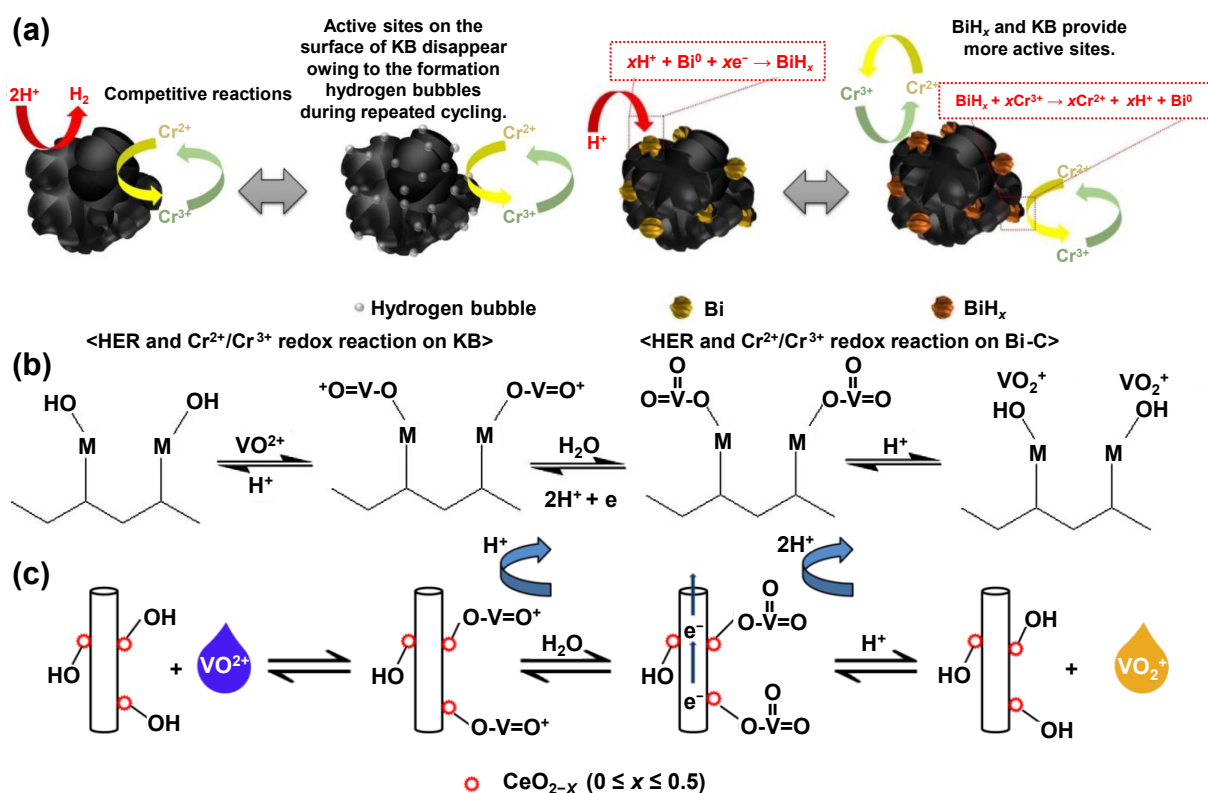


Figure 19 (a) Schematic of the electrochemical reaction on the KB and Bi-C. Reproduced with permission from Ref. [86], © Elsevier B.V. 2020. (b) Proposed catalytic mechanism on the CuPt₃ decorated electrode. Reproduced with permission from Ref. [190], © Elsevier Ltd. 2012. (c) Proposed mechanism on CeO₂/GF electrode. Reproduced with permission from Ref. [191], © The Royal Society of Chemistry 2014.

nanocomposite fluidization in this study, a lithium-free metal 3 V full-flow battery coupled with a high-concentration cathode electrolyte (5.0 M LiI) was realized. The CE is greater than 90% during cycling and exhibits a long cycle life.

5.4 Solid-state zinc ion batteries

Chu et al. have discovered a novel 3D interconnected electron transfer network. This structure adapts well to the abundance of active zinc and can inhibit the appearance of zinc dendrites [198]. The structure is constructed by stacking zinc paste and porous graphite felt layer by layer. This 3D structure exhibits excellent electrochemical activity and stability in zinc-based flow batteries. The battery capacity can reach 100 mAh/cm² during cycling, and the battery energy efficiency can reach 90%. The different charging processes of the zinc anode are shown in Figs. 20(c) and 20(d).

Wang et al. proposed poly(4,4'-hexanediol)-modified nanoporous carbon cathode zinc-ion batteries using antifreeze gels as a solid electrolyte [199]. In this study, they performed a range test on the battery service temperature, and the results showed that the battery could operate stably from 25 to -20 °C. And they also found that the redox reaction of the polymer electrode decreased reversibly as the operating temperature dropped. The batteries in this study could provide a discharge platform of about 1.15 V, which is superior to most other Zn organic batteries.

5.5 Potassium semi-solid battery

Wang et al. developed a non-corrosive, cost-effective aqueous slurry battery with an indigo anode electrolyte, which is easily homogeneously dispersed and exhibits superior K⁺ diffusion capabilities [200]. In this study, 1000 cycles were performed on the indigo/K₄Fe(CN)₆ battery. The results showed that the battery has

excellent cycle performance, the average CE exceeds 97.7%, and the capacity retention rate per cycle is close to 100% (99.98%). The research and development of this battery provides a new development idea for the application of insoluble oxidizing raw materials and successfully breaks through the barrier of solubility limit affecting energy density in battery systems.

5.6 A membrane-free redox flow battery

Wang et al. have successfully developed a flow-type membrane-free battery with high energy, high capacity, and long life. The separation of positive and negative poles depends on the principle of the organic and water phases not being insoluble. At a current density of 8.54 mA/cm², the membrane-free battery showed a capacity retention rate of 94.5% in 190 charge and discharge cycles, the membrane-free battery almost had no self-discharge reaction, and the Coulomb efficiency was greater than 99% [201].

5.7 Redox-targeted flow batteries using solid capacitor boosters

Elena Zanzola et al. designed a flow battery system with polyaniline (PANI) as a charge storage material and developed an indirect chemical cycle method. In this work, they used PANI and carbon black (CB) to significantly enhance the capacity and electronic conductivity of the battery system, and the battery used PANI/CB composite material is three times higher than the battery capacity of the electrolyte alone. This study showed that using solid charge storage materials can improve the energy and capacity of aqueous redox flow batteries, reduce reaction overpotential, and improve battery efficiency and performance [202].

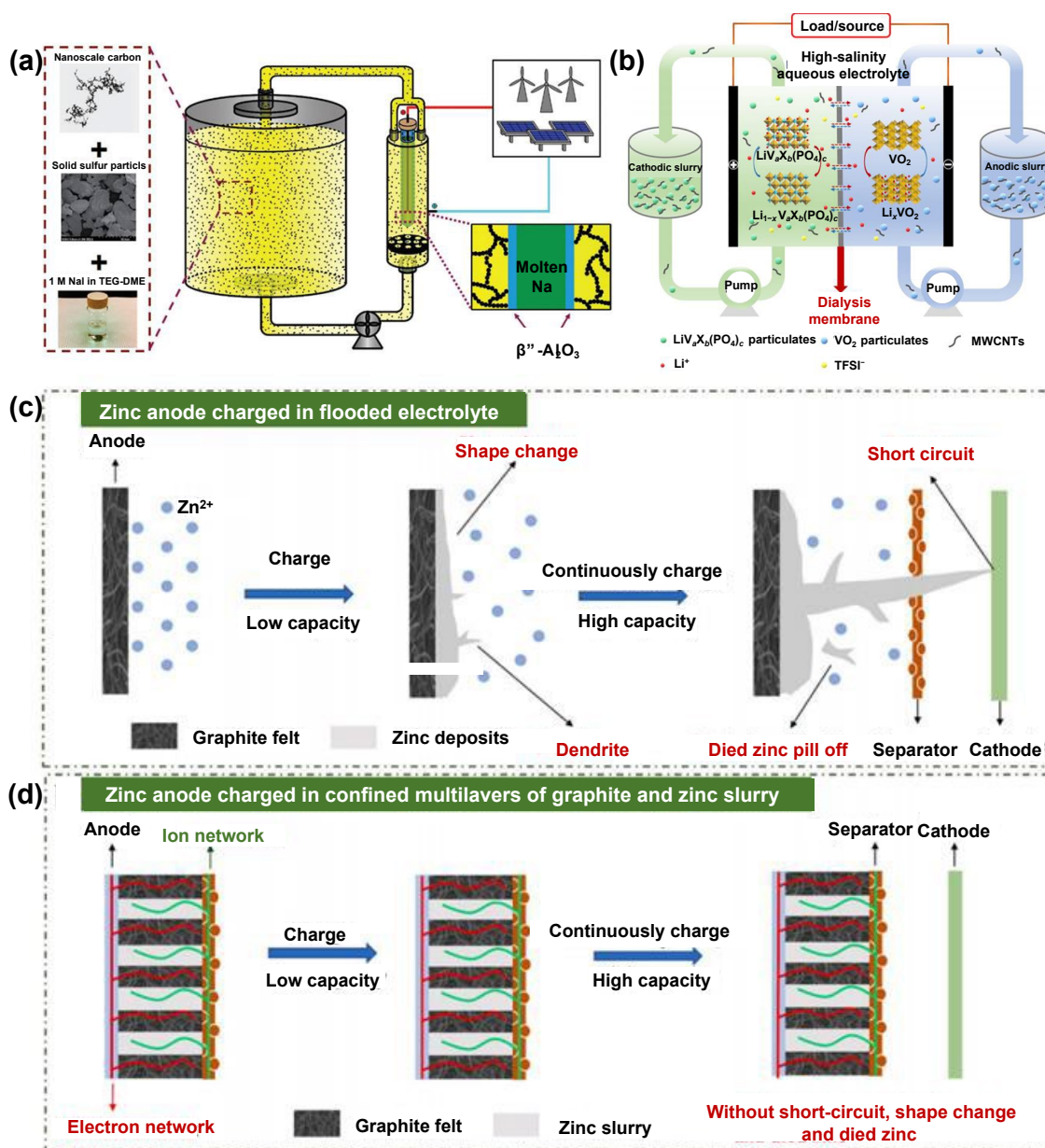


Figure 20 (a) A schematic of the semi-solid Na-S flow battery. Reproduced with permission from Ref. [192], © WILEY-VCH Verlag GmbH & Co. KGaA, Weinheim 2018. (b) Schematic configuration of an aqueous lithium-ion slurry flow battery. Reproduced with permission from Ref. [196], © American Chemical Society 2022. Schematic illustrations for different charging processes at zinc anodes: (c) traditional zinc anode and (d) zinc slurry anode. Reproduced with permission from Ref. [198], © Elsevier B.V. 2022.

6 Conclusions

In this review, we summarized the development of flow batteries in recent years, including types, mechanism studies, key component materials, and application areas. However, there are a few issues that should be taken seriously by us:

(1) Some limitations and challenges still exist that should be noted, which will be the focus of both research and application, such as the low current density and low power density of flow batteries. To solve these problems, research and exploration are essential.

(2) In addition, novel flow battery systems should be designed and applied to large-scale energy storage.

(3) Moreover, the combined cost of the flow battery system remains a key issue constraining its large-scale application.

(4) Finally, the study of the mechanism of the flow batteries is still necessary. Therefore, advanced technology should be

introduced into the flow battery. If this is achieved, the time and cost of experimentation will be greatly reduced. At the same time, the technical support and the analysis of data will accelerate the development of flow batteries.

VFBs can be used as energy storage power sources mainly used in power plant peak shaving to balance loads, large-scale photoelectric conversion, energy storage power sources for wind power generation, smart grids, and as energy storage systems in marginal areas, uninterruptible power supply or emergency power supply systems, municipal transportation, and military facilities. With the formation and improvement of the VFBs industry chain, VFBs will enter a period of rapid development. The breakthrough of the VFB key technology and further cost performance improvement will be beneficial to the industrialization of the VFBs.

ICRFBs have obvious advantages and are a powerful complement to flywheel energy storage and lithium-ion energy

storage. Opportunities are more concentrated in large-scale and long-term energy storage areas, such as peak shaving and valley filling on the grid side, renewable energy grid integration on the power generation side, and long-term energy storage. Whether it can become the mainstream technical route of large-scale energy storage depends on the level of technological development and national policies.

ZRFBs are expected to be widely used in large-scale energy storage technology due to their low cost and excellent performance. At present, it still needs the joint efforts of the national government and Research & Development institutions to develop and grow rapidly.

Organic non-aqueous RFBs have great Ohmic polarization due to their low conductivity and low concentration of active substances, resulting in low operating current density and high system cost. The main problems of organic aqueous flow batteries are poor conductivity, low working current density, small solubility, low energy density, low chemical stability, and poor cycle performance. The premise of the large-scale application is to solve these problems. First, the electrochemical and physicochemical properties of the electrolyte need to be studied more systematically. At the same time, new electrochemically active substances in the electrolyte also need to be explored. In addition, as one of the most critical materials for flow batteries, the research and development of separator materials should be strengthened in the research and development process of the new system.

So far, flow batteries have developed rapidly, including VFBS, ICRFBs, ZRFBs, organic RFBs, etc. Especially based on the low-carbon goal, RFBs have received great attention and expectations from researchers. RFBs are regarded as an advanced technology due to their large energy storage capacity, excellent charge and discharge characteristics, adjustable output power, long cycle life, environmental friendliness, and high safety.

In the past few decades, RFBs have been used in energy storage fields, such as renewable energy power generation, power system peak shaving and valley filling, industrial and commercial standby power stations, and civil power sources. In particular, some RFBs exhibit cycle stability with zero attenuation at high concentrations and can maintain high volume capacity and high conductivity at low temperatures, indicating the application potential in extreme environments.

Looking ahead, we believe that promoting technological innovation and development on the road to commercialization and industrialization is necessary. Artificial intelligence and machine learning techniques should be applied to the process of designing and improving the materials of key components of RFBs. These technologies can save material costs, increase productivity, and improve reliability.

Acknowledgements

This work was fully supported by the National Natural Science Foundation of China (No. 52211530034), the foundation of China University of Petroleum, Beijing (Nos. 2462020YXZZ018 and 2462023XKBH005), and the foundation of Beijing National Science Foundation (No. 3222018).

Declaration of conflicting interests

The authors declare no conflicting interests regarding the content of this article.

References

- Noack, J.; Roznyatovskaya, N.; Herr, T.; Fischer, P. The chemistry of redox-flow batteries. *Angew. Chem., Int. Ed* **2015**, *54*, 9776–9809.
- Zheng, Q.; Li, X. F.; Cheng, Y. H.; Ning, G. L.; Xing, F.; Zhang, H. M. Development and perspective in vanadium flow battery modeling. *Appl. Energy* **2014**, *132*, 254–266.
- Arévalo-Cid, P.; Dias, P.; Mendes, A.; Azevedo, J. Redox flow batteries: A new frontier on energy storage. *Sustainable Energy Fuels* **2021**, *5*, 5366–5419.
- Li, B.; Liu, J. Progress and directions in low-cost redox-flow batteries for large-scale energy storage. *Natl. Sci. Rev.* **2017**, *4*, 91–105.
- Wei, L.; Zhao, T. S.; Zeng, L.; Zhou, X. L.; Zeng, Y. K. Copper nanoparticle-deposited graphite felt electrodes for all vanadium redox flow batteries. *Appl. Energy* **2016**, *180*, 386–391.
- Leung, P.; Li, X. H.; Ponce de León, C.; Berlouis, L.; Low, C. T. J.; Walsh, F. C. Progress in redox flow batteries, remaining challenges and their applications in energy storage. *RSC Adv.* **2012**, *2*, 10125–10156.
- Park, M.; Ryu, J.; Wang, W.; Cho, J. Material design and engineering of next-generation flow-battery technologies. *Nat. Rev. Mater.* **2017**, *2*, 16080.
- Li, L. Y.; Kim, S.; Wang, W.; Vijayakumar, M.; Nie, Z. M.; Chen, B. W.; Zhang, J. L.; Xia, G. G.; Hu, J. Z.; Graff, G. et al. A stable vanadium redox-flow battery with high energy density for large-scale energy storage. *Adv. Energy Mater.* **2011**, *1*, 394–400.
- Yao, Y. X.; Lei, J. F.; Shi, Y.; Ai, F.; Lu, Y. C. Assessment methods and performance metrics for redox flow batteries. *Nat. Energy* **2021**, *6*, 582–588.
- Yang, D. S.; Han, J. H.; Jeon, J. W.; Lee, J. Y.; Kim, D. G.; Seo, D. H.; Kim, B. G.; Kim, T. H.; Hong, Y. T. Multimodal porous and nitrogen-functionalized electrode based on graphite felt modified with carbonized porous polymer skin layer for all-vanadium redox flow battery. *Mater. Today Energy* **2019**, *11*, 159–165.
- Branchi, M.; Gigli, M.; Mecheri, B.; Zurlo, F.; Licocchia, S.; D'Epifanio, A. Highly ion selective hydrocarbon-based membranes containing sulfonated hypercrosslinked polystyrene nanoparticles for vanadium redox flow batteries. *J. Membr. Sci.* **2018**, *563*, 552–560.
- Lu, W. J.; Yuan, Z. Z.; Zhao, Y. Y.; Zhang, H. Z.; Zhang, H. M.; Li, X. F. Porous membranes in secondary battery technologies. *Chem. Soc. Rev.* **2017**, *46*, 2199–2236.
- Cao, L. Y.; Skyllas-Kazacos, M.; Menictas, C.; Noack, J. A review of electrolyte additives and impurities in vanadium redox flow batteries. *J. Energy Chem.* **2018**, *27*, 1269–1291.
- Bamgbopa, M. O.; Shao-Horn, Y.; Almheiri, S. The potential of non-aqueous redox flow batteries as fast-charging capable energy storage solutions: Demonstration with an iron-chromium acetylacetonate chemistry. *J. Mater. Chem. A* **2017**, *5*, 13457–13468.
- Yu, L. H.; Xi, J. Y. Durable and efficient PTFE sandwiched SPEEK membrane for vanadium flow batteries. *ACS Appl. Mater. Interfaces* **2016**, *8*, 23425–23430.
- Sun, C. Y.; Zhang, H. Review of the development of first-generation redox flow batteries: Iron-chromium system. *ChemSusChem* **2022**, *15*, e202101798.
- Yuan, Z. Z.; Liu, X. Q.; Xu, W. B.; Duan, Y. Q.; Zhang, H. M.; Li, X. F. Negatively charged nanoporous membrane for a dendrite-free alkaline zinc-based flow battery with long cycle life. *Nat. Commun.* **2018**, *9*, 3731.
- Fu, J.; Cano, Z. P.; Park, M. G.; Yu, A. P.; Fowler, M.; Chen, Z. W. Electrically rechargeable zinc-air batteries: Progress, challenges, and perspectives. *Adv. Mater.* **2017**, *29*, 1604685.

- [19] Khor, A.; Leung, P.; Mohamed, M. R.; Flox, C.; Xu, Q.; An, L.; Wills, R. G. A.; Morante, J. R.; Shah, A. A. Review of zinc-based hybrid flow batteries: From fundamentals to applications. *Mater. Today Energy* **2018**, *8*, 80–108.
- [20] Hu, B.; Tang, Y. J.; Luo, J.; Grove, G.; Guo, Y. S.; Liu, T. L. Improved radical stability of viologen anolytes in aqueous organic redox flow batteries. *Chem. Commun.* **2018**, *54*, 6871–6874.
- [21] Yang, C. Z.; Nikiforidis, G.; Park, J. Y.; Choi, J.; Luo, Y.; Zhang, L.; Wang, S. C.; Chan, Y. T.; Lim, J.; Hou, Z. M. et al. Designing redox-stable cobalt-polypyridyl complexes for redox flow batteries: Spin-crossover delocalizes excess charge. *Adv. Energy Mater.* **2018**, *8*, 1702897.
- [22] Ding, Y.; Zhang, C. K.; Zhang, L. Y.; Zhou, Y. E.; Yu, G. H. Molecular engineering of organic electroactive materials for redox flow batteries. *Chem. Soc. Rev.* **2018**, *47*, 69–103.
- [23] Kowalski, J. A.; Su, L.; Milshtein, J. D.; Brushett, F. R. Recent advances in molecular engineering of redox active organic molecules for nonaqueous flow batteries. *Curr. Opin. Chem. Eng.* **2016**, *13*, 45–52.
- [24] Wei, X. L.; Pan, W. X.; Duan, W. T.; Hollas, A.; Yang, Z.; Li, B.; Nie, Z. M.; Liu, J.; Reed, D.; Wang, Y. et al. Materials and systems for organic redox flow batteries: Status and challenges. *ACS Energy Lett.* **2017**, *2*, 2187–2204.
- [25] Wei, L.; Zhao, T. S.; Zhao, G.; An, L.; Zeng, L. A high-performance carbon nanoparticle-decorated graphite felt electrode for vanadium redox flow batteries. *Appl. Energy* **2016**, *176*, 74–79.
- [26] Abbas, S.; Lee, H.; Hwang, J.; Mehmood, A.; Shin, H. J.; Mehboob, S.; Lee, J. Y.; Ha, H. Y. A novel approach for forming carbon nanorods on the surface of carbon felt electrode by catalytic etching for high-performance vanadium redox flow battery. *Carbon* **2018**, *128*, 31–37.
- [27] Zhao, Y.; Liu, L.; Qiu, X. P.; Xi, J. Y. Revealing sulfuric acid concentration impact on comprehensive performance of vanadium electrolytes and flow batteries. *Electrochim. Acta* **2019**, *303*, 21–31.
- [28] Yang, Y. D.; Zhang, Y. M.; Liu, T.; Huang, J. Improved broad temperature adaptability and energy density of vanadium redox flow battery based on sulfate-chloride mixed acid by optimizing the concentration of electrolyte. *J. Power Sources* **2019**, *415*, 62–68.
- [29] Nguyen, T. D.; Wang, L. P.; Whitehead, A.; Wai, N.; Scherer, G. G.; Xu, Z. J. Insights into the synergistic effect of ammonium and phosphate-containing additives for a thermally stable vanadium redox flow battery electrolyte. *J. Power Sources* **2018**, *402*, 75–81.
- [30] Song, Y. X.; Li, X. R.; Yan, C. W.; Tang, A. Uncovering ionic conductivity impact towards high power vanadium flow battery design and operation. *J. Power Sources* **2020**, *480*, 229141.
- [31] Wei, L.; Zeng, L.; Wu, M. C.; Fan, X. Z.; Zhao, T. S. Seawater as an alternative to deionized water for electrolyte preparations in vanadium redox flow batteries. *Appl. Energy* **2019**, *251*, 113344.
- [32] Zhang, Z. H.; Wei, L.; Wu, M. C.; Bai, B. F.; Zhao, T. S. Chloride ions as an electrolyte additive for high performance vanadium redox flow batteries. *Appl. Energy* **2021**, *289*, 116690.
- [33] Mousa, A.; Skyllas-Kazacos, M. Effect of additives on the low-temperature stability of vanadium redox flow battery negative half-cell electrolyte. *ChemElectroChem* **2015**, *2*, 1742–1751.
- [34] Ai, F.; Wang, Z. Y.; Lai, N. C.; Zou, Q. L.; Liang, Z. J.; Lu, Y. C. Heteropoly acid negolytes for high-power-density aqueous redox flow batteries at low temperatures. *Nat. Energy* **2022**, *7*, 417–426.
- [35] Min-suk, J. J.; Parrondo, J.; Arges, C. G.; Ramani, V. Polysulfone-based anion exchange membranes demonstrate excellent chemical stability and performance for the all-vanadium redox flow battery. *J. Mater. Chem. A* **2013**, *1*, 10458–10464.
- [36] Gan, R. J.; Ma, Y. J.; Li, S. S.; Zhang, F. X.; He, G. H. Facile fabrication of amphoteric semi-interpenetrating network membranes for vanadium flow battery applications. *J. Energy Chem.* **2018**, *27*, 1189–1197.
- [37] Li, X. F.; Zhang, H. M.; Mai, Z. S.; Zhang, H. Z.; Vankelecom, I. Ion exchange membranes for vanadium redox flow battery (VRB) applications. *Energy Environ. Sci.* **2011**, *4*, 1147–1160.
- [38] Kim, J. Q.; So, S.; Kim, H. T.; Choi, S. Q. Highly ordered ultrathin perfluorinated sulfonic acid ionomer membranes for vanadium redox flow battery. *ACS Energy Lett.* **2021**, *6*, 184–192.
- [39] Zeng, L.; Zhao, T. S.; Wei, L.; Zeng, Y. K.; Zhang, Z. H. Polyvinylpyrrolidone-based semi-interpenetrating polymer networks as highly selective and chemically stable membranes for all vanadium redox flow batteries. *J. Power Sources* **2016**, *327*, 374–383.
- [40] Shin, D. W.; Guiver, M. D.; Lee, Y. M. Hydrocarbon-based polymer electrolyte membranes: Importance of morphology on ion transport and membrane stability. *Chem. Rev.* **2017**, *117*, 4759–4805.
- [41] Bhushan, M.; Kumar, S.; Singh, A. K.; Shahi, V. K. High-performance membrane for vanadium redox flow batteries: Cross-linked poly(ether ether ketone) grafted with sulfonic acid groups via the spacer. *J. Membr. Sci.* **2019**, *583*, 1–8.
- [42] Zhou, J. H.; Liu, Y. H.; Zuo, P. P.; Li, Y. Y.; Dong, Y.; Wu, L.; Yang, Z. J.; Xu, T. W. Highly conductive and vanadium sieving microporous Tröger's base membranes for vanadium redox flow battery. *J. Membr. Sci.* **2021**, *620*, 118832.
- [43] Lohse, M. S.; Bein, T. Covalent organic frameworks: Structures, synthesis, and applications. *Adv. Funct. Mater.* **2018**, *28*, 1705553.
- [44] Sasmal, H. S.; Aiyappa, H. B.; Bhange, S. N.; Karak, S.; Halder, A.; Kurungot, S.; Banerjee, R. Superprotonic conductivity in flexible porous covalent organic framework membranes. *Angew. Chem.* **2018**, *130*, 11060–11064.
- [45] Di, M. T.; Hu, L.; Gao, L.; Yan, X. M.; Zheng, W. J.; Dai, Y.; Jiang, X. B.; Wu, X. M.; He, G. H. Covalent organic framework (COF) constructed proton permselective membranes for acid supporting redox flow batteries. *Chem. Eng. J.* **2020**, *399*, 125833.
- [46] Deng, Q.; Huang, P.; Zhou, W. X.; Ma, Q.; Zhou, N.; Xie, H.; Ling, W.; Zhou, C. J.; Yin, Y. X.; Wu, X. W. et al. A high-performance composite electrode for vanadium redox flow batteries. *Adv. Energy Mater.* **2017**, *7*, 1700461.
- [47] Zhang, Y.; Qian, G. C.; Huang, C. D.; Wang, Y. X. Effect of modification of polyacrylonitrile-based graphite felts on their performance in redox fuel cell and redox flow battery. *J. Power Sources* **2016**, *324*, 528–537.
- [48] Han, P. X.; Wang, H. B.; Liu, Z. H.; Chen, X.; Ma, W.; Yao, J. H.; Zhu, Y. W.; Cui, G. L. Graphene oxide nanoplatelets as excellent electrochemical active materials for $\text{VO}_2^+/\text{VO}^{2+}$ and $\text{V}^{2+}/\text{V}^{3+}$ redox couples for a vanadium redox flow battery. *Carbon* **2011**, *49*, 693–700.
- [49] Lim, H.-S.; Chae, S.; Yan, L. T.; Li, G. S.; Feng, R. Z.; Shin, Y.; Nie, Z. M.; Sivakumar, B. M.; Zhang, X.; Liang, Y. G. et al. Crosslinked polyethyleneimine gel polymer interface to improve cycling stability of RFBs. *Energy Mater. Adv.* **2022**, *2022*, <https://doi.org/10.34133/32022/9863679>.
- [50] Jin, J. T.; Fu, X. G.; Liu, Q.; Liu, Y. R.; Wei, Z. Y.; Niu, K. X.; Zhang, J. Y. Identifying the active site in nitrogen-doped graphene for the $\text{VO}^{2+}/\text{VO}_2^+$ redox reaction. *ACS Nano* **2013**, *7*, 4764–4773.
- [51] Li, W. Y.; Zhang, Z. Y.; Tang, Y. B.; Bian, H. D.; Ng, T. W.; Zhang, W. J.; Lee, C. S. Graphene-nanowall-decorated carbon felt with excellent electrochemical activity toward $\text{VO}_2^+/\text{VO}^{2+}$ couple for all vanadium redox flow battery. *Adv. Sci.* **2016**, *3*, 1500276.
- [52] Huang, P.; Ling, W.; Sheng, H.; Zhou, Y.; Wu, X. P.; Zeng, X. X.; Wu, X. W.; Guo, Y. G. Heteroatom-doped electrodes for all-vanadium redox flow batteries with ultralong lifespan. *J. Mater. Chem. A* **2018**, *6*, 41–44.
- [53] Ma, Q.; Deng, Q.; Sheng, H.; Ling, W.; Wang, H. Y.; Jiao, H. W.; Wu, X. W.; Zhou, W. X.; Zeng, X. X.; Yin, Y. X. et al. High electro-catalytic graphite felt/ MnO_2 composite electrodes for vanadium redox flow batteries. *Sci. China* **2018**, *61*, 732–738.

- [54] Petek, T. J.; Hoyt, N. C.; Savinell, R. F.; Wainright, J. S. Characterizing slurry electrodes using electrochemical impedance spectroscopy. *J. Electrochem. Soc.* **2016**, *163*, A5001–A5009.
- [55] Percin, K.; Rommerskirchen, A.; Sengpiel, R.; Gendel, Y.; Wessling, M. 3D-printed conductive static mixers enable all-vanadium redox flow battery using slurry electrodes. *J. Power Sources* **2018**, *379*, 228–233.
- [56] Zheng, Q.; Xing, F.; Li, X. F.; Liu, T.; Lai, Q. Z.; Ning, G. L.; Zhang, H. M. Dramatic performance gains of a novel circular vanadium flow battery. *J. Power Sources* **2015**, *277*, 104–109.
- [57] Bhattarai, A.; Wai, N.; Schweiss, R.; Whitehead, A.; Lim, T. M.; Hng, H. H. Advanced porous electrodes with flow channels for vanadium redox flow battery. *J. Power Sources* **2017**, *341*, 83–90.
- [58] Al-Yasiri, M.; Park, J. A novel cell design of vanadium redox flow batteries for enhancing energy and power performance. *Appl. Energy* **2018**, *222*, 530–539.
- [59] Li, X. F.; Zhang, H. Z.; Zheng, Q.; Yan, J. W.; Guo, Y. G.; Hu, Y. S. Electrochemical energy storage technology in energy revolution. *Bull. Chin. Acad. Sci.* **2019**, *34*, 443–449.
- [60] Sun, C. Y.; Zhang, H.; Luo, X. D.; Chen, N. A comparative study of Nafion and sulfonated poly(ether ether ketone) membrane performance for iron-chromium redox flow battery. *Ionics* **2019**, *25*, 4219–4229.
- [61] *Wuhan Nanrui VFBS energy storage system* [Online]. https://www.sohu.com/a/498690633_418320 (accessed Apr 30, 2023).
- [62] *Weilide Xinjiang Awati VFBS energy storage power station* [Online]. https://m.sohu.com/a/440547278_465261 (accessed Apr 30, 2023).
- [63] *Shantou Smart Energy RFBs Energy Storage* [Online]. <https://mnewenergy.in-en.com/html/newenergy-2406327.shtml> (accessed Apr 30, 2023).
- [64] Zhang, H.; Tan, Y.; Luo, X. D.; Sun, C. Y.; Chen, N. Polarization effects of a rayon and polyacrylonitrile based graphite felt for iron-chromium redox flow batteries. *ChemElectroChem* **2019**, *6*, 3175–3188.
- [65] Su, Y.; Chen, N.; Ren, H. L.; Guo, L. L.; Li, Z.; Wang, X. M. Preparation and properties of indium ion modified graphite felt composite electrode. *Front. Chem.* **2022**, *10*, 899287.
- [66] Zeng, Y. K.; Zhao, T. S.; An, L.; Zhou, X. L.; Wei, L. A comparative study of all-vanadium and iron-chromium redox flow batteries for large-scale energy storage. *J. Power Sources* **2015**, *300*, 438–443.
- [67] Wang, S. L.; Xu, Z. Y.; Wu, X. L.; Zhao, H.; Zhao, J. L.; Liu, J. G.; Yan, C. W.; Fan, X. Z. Excellent stability and electrochemical performance of the electrolyte with indium ion for iron-chromium flow battery. *Electrochim. Acta* **2021**, *368*, 137524.
- [68] Johnson, D. A.; Reid, M. A. Chemical and electrochemical behavior of the Cr(III)/Cr(II) half-cell in the iron-chromium redox energy storage system. *J. Electrochem. Soc.* **1985**, *132*, 1058–1062.
- [69] Zhang, H.; Sun, C. Y. Cost-effective iron-based aqueous redox flow batteries for large-scale energy storage application: A review. *J. Power Sources* **2021**, *493*, 229445.
- [70] Wang, S. L.; Xu, Z. Y.; Wu, X. L.; Zhao, H.; Zhao, J. L.; Liu, J. G.; Yan, C. W.; Fan, X. Z. Analyses and optimization of electrolyte concentration on the electrochemical performance of iron-chromium flow battery. *Appl. Energy* **2020**, *271*, 115252.
- [71] Waters, S. E.; Robb, B. H.; Marshak, M. P. Effect of chelation on iron-chromium redox flow batteries. *ACS Energy Lett.* **2020**, *5*, 1758–1762.
- [72] Sun, C. Y.; Zhang, H. Investigation of Nafion series membranes on the performance of iron-chromium redox flow battery. *Int. J. Energy Res.* **2019**, *43*, 8739–8752.
- [73] Yang, P.; Xuan, S. S.; Long, J.; Wang, Y. L.; Zhang, Y. P.; Zhang, H. P. Fluorine-containing branched sulfonated polyimide membrane for vanadium redox flow battery applications. *ChemElectroChem* **2018**, *5*, 3695–3707.
- [74] Teng, X. G.; Yu, C.; Wu, X. F.; Dong, Y. C.; Gao, P.; Hu, H. L.; Zhu, Y. M.; Dai, J. C. PTFE/SPEEK/PDDA/PSS composite membrane for vanadium redox flow battery application. *J. Mater. Sci.* **2018**, *53*, 5204–5215.
- [75] Xu, Z.; Michos, I.; Cao, Z. S.; Jing, W. H.; Gu, X. H.; Hinkle, K.; Murad, S.; Dong, J. H. Proton-selective ion transport in ZSM-5 zeolite membrane. *J. Phys. Chem. C* **2016**, *120*, 26386–26392.
- [76] Zeng, Y. K.; Zhao, T. S.; Zhou, X. L.; Zeng, L.; Wei, L. The effects of design parameters on the charge–discharge performance of iron-chromium redox flow batteries. *Appl. Energy* **2016**, *182*, 204–209.
- [77] Nibel, O.; Schmidt, T. J.; Gubler, L. Bifunctional ion-conducting polymer electrolyte for the vanadium redox flow battery with high selectivity. *J. Electrochem. Soc.* **2016**, *163*, A2563–A2570.
- [78] Mu, D.; Yu, L. H.; Liu, L.; Xi, J. Y. Rice paper reinforced sulfonated poly(ether ether ketone) as low-cost membrane for vanadium flow batteries. *ACS Sustainable Chem. Eng.* **2017**, *5*, 2437–2444.
- [79] Qiao, L.; Liu, S. M.; Fang, M. L.; Yang, M. J.; Ma, X. K. A composite membrane with high stability and low cost specifically for iron-chromium flow battery. *Polymers* **2022**, *14*, 2245.
- [80] Rabbow, T. J.; Trampert, M.; Pokorny, P.; Binder, P.; Whitehead, A. H. Variability within a single type of polyacrylonitrile-based graphite felt after thermal treatment. Part I: Physical properties. *Electrochim. Acta* **2015**, *173*, 17–23.
- [81] Kim, K. J.; Park, M. S.; Kim, Y. J.; Kim, J. H.; Dou, S. X.; Skyllas-Kazacos, M. A technology review of electrodes and reaction mechanisms in vanadium redox flow batteries. *J. Mater. Chem. A* **2015**, *3*, 16913–16933.
- [82] Zhang, H.; Tan, Y.; Li, J. Y.; Xue, B. Studies on properties of rayon- and polyacrylonitrile-based graphite felt electrodes affecting Fe/Cr redox flow battery performance. *Electrochim. Acta* **2017**, *248*, 603–613.
- [83] Zhang, H.; Chen, N.; Sun, C. Y.; Luo, X. D. Investigations on physicochemical properties and electrochemical performance of graphite felt and carbon felt for iron-chromium redox flow battery. *Int. J. Energy Res.* **2020**, *44*, 3839–3853.
- [84] Chen, N.; Zhang, H.; Luo, X. D.; Sun, C. Y. SiO₂-decorated graphite felt electrode by silicic acid etching for iron-chromium redox flow battery. *Electrochim. Acta* **2020**, *336*, 135646.
- [85] Li, Z.; Guo, L. L.; Chen, N.; Su, Y.; Wang, X. M. Boric acid thermal etching graphite felt as a high-performance electrode for iron-chromium redox flow battery. *Mater. Res. Express* **2022**, *9*, 025601.
- [86] Ahn, Y.; Moon, J.; Park, S. E.; Shin, J.; Wook Choi, J.; Kim, K. J. High-performance bifunctional electrocatalyst for iron-chromium redox flow batteries. *Chem. Eng. J* **2021**, *421*, 127855.
- [87] Zeng, Y. K.; Zhou, X. L.; Zeng, L.; Yan, X. H.; Zhao, T. S. Performance enhancement of iron-chromium redox flow batteries by employing interdigitated flow fields. *J. Power Sources* **2016**, *327*, 258–264.
- [88] Zeng, Y. K.; Zhou, X. L.; An, L.; Wei, L.; Zhao, T. S. A high-performance flow-field structured iron-chromium redox flow battery. *J. Power Sources* **2016**, *324*, 738–744.
- [89] Thaller, L. H. Electrically rechargeable redox flow cells. In *Proceedings of the 9th Intersociety Energy Conversion Engineering Conference*, San Francisco, USA, 1974; pp 924–928.
- [90] Hagedorn, N. H. NASA redox storage system development project. Final Report. NASA Lewis Research Center, Cleveland, OH (USA), 1984.
- [91] Thaller, L. Redox flow cell energy storage systems. In *Proceedings of Terrestrial Energy Systems Conference*, Orlando, USA, 1979; pp 989.
- [92] Lin, Z. Q.; Jiang, Z. Research progress of Fe-Cr redox-flow battery

- in Japan I development progress of Fe-Cr redox-flow battery. *Chin. J. Power Sources* **1991**, 32–39, 47.
- [93] Futamata, M.; Higuchi, S.; Nakamura, O.; Ogino, I.; Takada, Y.; Okazaki, S.; Ashimura, S.; Takahashi, S. Performance testing of 10 kW-class advanced batteries for electric energy storage systems in Japan. *J. Power Sources* **1988**, 24, 137–155.
- [94] Soloveichik, G. L. Flow batteries: Current status and trends. *Chem. Rev.* **2015**, 115, 11533–11558.
- [95] Yang, L.; Wang, H.; Li, X. M.; Zhao, Z.; Zuo, Y. J.; Liu, Y. J.; Liu, Y. Introduction and engineering case analysis of 250 kW/1.5 MW-h iron-chromium redox flow batteries energy storage demonstration power station. *Energy Storage Sci. Technol.* **2020**, 9, 751–756.
- [96] Song, Z. C.; Zhang, B. F.; Tong, B.; Zhong, Y. Q.; Kang, M. Commercialization progress of flow battery and its application prospects in electric power system. *Therm. Power Gener.* **2022**, 51, 9–20.
- [97] Wang, G. X.; Zou, H. T.; Zhu, X. B.; Ding, M.; Jia, C. K. Recent progress in zinc-based redox flow batteries: A review. *J. Phys. D Appl. Phys.* **2022**, 55, 163001.
- [98] Huang, S. Q.; Yuan, Z. Z.; Salla, M.; Wang, X.; Zhang, H.; Huang, S. P.; Lek, D. G.; Li, X. F.; Wang, Q. A redox-mediated zinc electrode for ultra-robust deep-cycle redox flow batteries. *Energy Environ. Sci.* **2023**, 16, 438–445.
- [99] Xie, C. X.; Li, T. Y.; Deng, C. Z.; Song, Y.; Zhang, H. M.; Li, X. F. A highly reversible neutral zinc/manganese battery for stationary energy storage. *Energy Environ. Sci.* **2020**, 13, 135–143.
- [100] Lei, J. F.; Yao, Y. X.; Wang, Z. Y.; Lu, Y.-C. Towards high-areal-capacity aqueous zinc-manganese batteries: Promoting MnO₂ dissolution by redox mediators. *Energy Environ. Sci.* **2021**, 14, 4418–4426.
- [101] Kim, M.; Lee, S.; Choi, J.; Park, J.; Park, J. W.; Park, M. Reversible metal ionic catalysts for high-voltage aqueous hybrid zinc-manganese redox flow batteries. *Energy Storage Mater.* **2023**, 55, 698–707.
- [102] Yu, X.; Song, Y. X.; Tang, A. Tailoring manganese coordination environment for a highly reversible zinc-manganese flow battery. *J. Power Sources* **2021**, 507, 230295.
- [103] Li, B.; Nie, Z. M.; Vijayakumar, M.; Li, G. S.; Liu, J.; Sprenkle, V.; Wang, W. Ambipolar zinc-polyiodide electrolyte for a high-energy density aqueous redox flow battery. *Nat. Commun.* **2015**, 6, 6303.
- [104] Xie, C. X.; Zhang, H. M.; Xu, W. B.; Wang, W.; Li, X. F. A long cycle life, self-healing zinc-iodine flow battery with high power density. *Angew. Chem., Int. Ed.* **2018**, 57, 11171–11176.
- [105] Jiang, H. R.; Wu, M. C.; Ren, Y. X.; Shyy, W.; Zhao, T. S. Towards a uniform distribution of zinc in the negative electrode for zinc bromine flow batteries. *Appl. Energy* **2018**, 213, 366–374.
- [106] Wu, M. C.; Zhao, T. S.; Zhang, R. H.; Wei, L.; Jiang, H. R. Carbonized tubular polypyrrole with a high activity for the Br₂/Br⁻ redox reaction in zinc-bromine flow batteries. *Electrochim. Acta* **2018**, 284, 569–576.
- [107] Yang, M. H.; Xu, Z. Z.; Xiang, W. Z.; Xu, H.; Ding, M.; Li, L. Y.; Tang, A.; Gao, R. H.; Zhou, G. M.; Jia, C. K. High performance and long cycle life neutral zinc-iron flow batteries enabled by zinc-bromide complexation. *Energy Storage Mater.* **2022**, 44, 433–440.
- [108] Wu, M. C.; Jiang, H. R.; Zhang, R. H.; Wei, L.; Chan, K. Y.; Zhao, T. S. N-doped graphene nanoplatelets as a highly active catalyst for Br₂/Br⁻ redox reactions in zinc-bromine flow batteries. *Electrochim. Acta* **2019**, 318, 69–75.
- [109] Xu, Z. C.; Fan, Q.; Li, Y.; Wang, J.; Lund, P. D. Review of zinc dendrite formation in zinc bromine redox flow battery. *Renew. Sustainable Energy Rev.* **2020**, 127, 109838.
- [110] Yin, Y. B.; Wang, S. N.; Zhang, Q.; Song, Y.; Chang, N. N.; Pan, Y. W.; Zhang, H. M.; Li, X. F. Dendrite-free zinc deposition induced by tin-modified multifunctional 3d host for stable zinc-based flow battery. *Adv. Mater.* **2020**, 32, 1906803.
- [111] Lu, W. J.; Xu, P. C.; Shao, S. Y.; Li, T. Y.; Zhang, H. M.; Li, X. F. Multifunctional carbon felt electrode with N-rich defects enables a long-cycle zinc-bromine flow battery with ultrahigh power density. *Adv. Funct. Mater.* **2021**, 31, 2102913.
- [112] Chen, H. L.; Kang, C. Z.; Shang, E. H.; Liu, G. Y.; Chen, D. J.; Yuan, Z. Z. Montmorillonite-based separator enables a long-life alkaline zinc-iron flow battery. *Ind. Eng. Chem. Res.* **2023**, 62, 676–684.
- [113] Mariyappan, K.; Ragupathy, P.; Ulaganathan, M. Enhancement of bromine kinetics using Pt@graphite felt and its applications in Zn-Br₂ redox flow battery. *J. Electrochem. Soc.* **2021**, 168, 090566.
- [114] Suresh, S.; Ulaganathan, M.; Aswathy, R.; Ragupathy, P. Enhancement of bromine reversibility using chemically modified electrodes and their applications in zinc bromine hybrid redox flow batteries. *ChemElectroChem* **2018**, 5, 3411–3418.
- [115] Xiang, H. X.; Tan, A. D.; Piao, J. H.; Fu, Z. Y.; Liang, Z. X. Efficient nitrogen-doped carbon for zinc-bromine flow battery. *Small* **2019**, 15, 1901848.
- [116] Gao, L. J.; Li, Z. X.; Zou, Y. P.; Yin, S. F.; Peng, P.; Shao, Y. Y.; Liang, X. A high-performance aqueous zinc-bromine static battery. *iScience* **2020**, 23, 101348.
- [117] Zelger, C.; Stübenbacher, M.; Laskos, A.; Gollas, B. State of charge indicators for alkaline zinc-air redox flow batteries. *J. Power Sources* **2019**, 424, 76–81.
- [118] Abbasi, A.; Hosseini, S.; Somwangthanaroj, A.; Checharoen, R.; Oлару, S.; Kheawhom, S. Discharge profile of a zinc-air flow battery at various electrolyte flow rates and discharge currents. *Sci. Data* **2020**, 7, 196.
- [119] Cheng, Y. H.; Li, D. M.; Shi, L.; Xiang, Z. H. Efficient unitary oxygen electrode for air-based flow batteries. *Nano Energy* **2018**, 47, 361–367.
- [120] Cui, J.; Leng, Y. M.; Xiang, Z. H. FeNi co-doped electrocatalyst synthesized via binary ligand strategy as a bifunctional catalyst for Zn-air flow battery. *Chem. Eng. Sci.* **2022**, 247, 117038.
- [121] Zhang, W.; Chang, J. F.; Wang, G. Z.; Li, Z.; Wang, M. Y.; Zhu, Y. M.; Li, B. Y.; Zhou, H.; Wang, G. F.; Gu, M. et al. Surface oxygenation induced strong interaction between Pd catalyst and functional support for zinc-air batteries. *Energy Environ. Sci.* **2022**, 15, 1573–1584.
- [122] Huang, S. Q.; Zhang, H.; Zhuang, J. H.; Zhou, M. Y.; Gao, M. Q.; Zhang, F. F.; Wang, Q. Redox-mediated two-electron oxygen reduction reaction with ultrafast kinetics for Zn-air flow battery. *Adv. Energy Mater.* **2022**, 12, 2103622.
- [123] Zhang, H.; Huang, S. Q.; Salla, M.; Zhuang, J. H.; Gao, M. Q.; Lek, D. G.; Ye, H. L.; Wang, Q. A redox-mediated zinc-air fuel cell. *ACS Energy Lett.* **2022**, 7, 2565–2575.
- [124] Shi, Y.; Wang, Z. Y.; Yao, Y. X.; Wang, W. W.; Lu, Y. C. High-areal-capacity conversion type iron-based hybrid redox flow batteries. *Energy Environ. Sci.* **2021**, 14, 6329–6337.
- [125] Yao, Y. X.; Wang, Z. Y.; Li, Z. J.; Lu, Y. C. A dendrite-free tin anode for high-energy aqueous redox flow batteries. *Adv. Mater.* **2021**, 33, 2008095.
- [126] Lu, W. J.; Li, T. Y.; Yuan, C. G.; Zhang, H. M.; Li, X. F. Advanced porous composite membrane with ability to regulate zinc deposition enables dendrite-free and high-areal capacity zinc-based flow battery. *Energy Storage Mater.* **2022**, 47, 415–423.
- [127] Khataee, A.; Wedege, K.; Dražević, E.; Bontien, A. Differential pH as a method for increasing cell potential in organic aqueous flow batteries. *J. Mater. Chem. A* **2017**, 5, 21875–21882.
- [128] Gerhardt, M. R.; Beh, E. S.; Tong, L. C.; Gordon, R. G.; Aziz, M. J. Comparison of capacity retention rates during cycling of quinone-bromide flow batteries. *MRS Adv.* **2017**, 2, 431–438.
- [129] Gerhardt, M. R.; Tong, L. C.; Gómez-Bombarelli, R.; Chen, Q.; Marshak, M. P.; Galvin, C. J.; Aspuru-Guzik, A.; Gordon, R. G.; Aziz, M. J. Anthraquinone derivatives in aqueous flow batteries. *Adv. Energy Mater.* **2017**, 7, 1601488.

- [130] Yang, B.; Hooper-Burkhardt, L.; Wang, F.; Surya Prakash, G. K.; Narayanan, S. R. An inexpensive aqueous flow battery for large-scale electrical energy storage based on water-soluble organic redox couples. *J. Electrochem. Soc.* **2014**, *161*, A1371–A1380.
- [131] Liu, W. Q.; Zhao, Z. M.; Li, T. Y.; Li, S. H.; Zhang, H. M.; Li, X. F. A high potential biphenol derivative cathode: Toward a highly stable air-insensitive aqueous organic flow battery. *Sci. Bull.* **2021**, *66*, 457–463.
- [132] Wang, C. X.; Yang, Z.; Yu, B.; Wang, H. Z.; Zhang, K. Q.; Li, G. G.; Tie, Z. X.; Jin, Z. Alkaline soluble 1,3,5,7-tetrahydroxyanthraquinone with high reversibility as anolyte for aqueous redox flow battery. *J. Power Sources* **2022**, *524*, 231001.
- [133] Huang, S. Q.; Zhang, H.; Salla, M.; Zhuang, J. H.; Zhi, Y. F.; Wang, X.; Wang, Q. Molecular engineering of dihydroxyanthraquinone-based electrolytes for high-capacity aqueous organic redox flow batteries. *Nat. Commun.* **2022**, *13*, 4746.
- [134] Wang, C. X.; Li, X.; Yu, B.; Wang, Y. R.; Yang, Z.; Wang, H. Z.; Lin, H. N.; Ma, J.; Li, G. G.; Jin, Z. Molecular design of fused-ring phenazine derivatives for long-cycling alkaline redox flow batteries. *ACS Energy Lett.* **2020**, *5*, 411–417.
- [135] Liu, Z. R.; Wang, Z.; Shi, Y. J.; Shen, Y. M.; Wang, W. C.; Chen, Z. D.; Xu, J.; Cao, J. Y. A high-capacity hexaazatrinaphthylene anode for aqueous organic hybrid flow batteries. *J. Mater. Chem. A* **2021**, *9*, 27028–27033.
- [136] Wu, M.; Jing, Y.; Wong, A. A.; Fell, E. M.; Jin, S. J.; Tang, Z. J.; Gordon, R. G.; Aziz, M. J. Extremely stable anthraquinone nopolymers synthesized from common precursors. *Chem* **2020**, *6*, 1432–1442.
- [137] Hollas, A.; Wei, X. L.; Murugesan, V.; Nie, Z. M.; Li, B.; Reed, D.; Liu, J.; Sprenkle, V.; Wang, W. A biomimetic high-capacity phenazine-based anolyte for aqueous organic redox flow batteries. *Nat. Energy* **2018**, *3*, 508–514.
- [138] Ye, C. C.; Wang, A. Q.; Breakwell, C.; Tan, R.; Grazia Bezzu, C.; Hunter-Sellars, E.; Williams, D. R.; Brandon, N. P.; Klusener, P. A. A.; Kucernak, A. R. et al. Development of efficient aqueous organic redox flow batteries using ion-sieving sulfonated polymer membranes. *Nat. Commun.* **2022**, *13*, 3184.
- [139] Lv, X. L.; Sullivan, P.; Fu, H. C.; Hu, X. X.; Liu, H. H.; Jin, S.; Li, W. J.; Feng, D. W. Dextrosil-viologen: A robust and sustainable anolyte for aqueous organic redox flow batteries. *ACS Energy Lett.* **2022**, *7*, 2428–2434.
- [140] Fan, H.; Wu, W. D.; Ravivarma, M.; Li, H. B.; Hu, B.; Lei, J. F.; Feng, Y. Y.; Sun, X. H.; Song, J. X.; Liu, T. L. Mitigating ring-opening to develop stable TEMPO catholytes for pH-neutral all-organic redox flow batteries. *Adv. Funct. Mater.* **2022**, *32*, 2203032.
- [141] Wu, W. D.; Luo, J.; Wang, F.; Yuan, B.; Liu, T. L. A self-trapping, bipolar viologen bromide electrolyte for redox flow batteries. *ACS Energy Lett.* **2021**, *6*, 2891–2897.
- [142] Xiao, Y.; Xu, J. H.; Hu, L.; Wang, H.; Gao, L.; Peng, S. Q.; Di, M. T.; Sun, X. J.; Liu, J.; Yan, X. M. Advanced anion-selective membranes with pendant quaternary ammonium for neutral aqueous supporting redox flow battery. *J. Membr. Sci.* **2022**, *659*, 120748.
- [143] Liu, B.; Tang, C. W.; Zhang, C.; Jia, G. C.; Zhao, T. S. Cost-effective, high-energy-density, nonaqueous nitrobenzene organic redox flow battery. *Chem. Mater.* **2021**, *33*, 978–986.
- [144] Xu, D. H.; Zhang, C. J.; Zhen, Y. H.; Zhao, Y. C.; Li, Y. D. A high-rate nonaqueous organic redox flow battery. *J. Power Sources* **2021**, *495*, 229819.
- [145] Yan, Y. C.; Walser-Kuntz, R.; Sanford, M. S. Targeted optimization of phenoxazine redox center for nonaqueous redox flow batteries. *ACS Mater. Lett.* **2022**, *4*, 733–739.
- [146] Yan, Y. C.; Vogt, D. B.; Vaid, T. P.; Sigman, M. S.; Sanford, M. S. Development of high energy density diamino-cyclopropenium-phenothiazine hybrid catholytes for non-aqueous redox flow batteries. *Angew. Chem., Int. Ed.* **2021**, *60*, 27039–27045.
- [147] Nambafu, G. S.; Delmo, E. P.; Bin Shahid, U.; Zhang, C.; Chen, Q.; Zhao, T. S.; Gao, P.; Amine, K.; Shao, M. H. Pyromellitic diimide based bipolar molecule for total organic symmetric redox flow battery. *Nano Energy* **2022**, *94*, 106963.
- [148] Su, L.; Darling, R. M.; Gallagher, K. G.; Xie, W.; Thelen, J. L.; Badel, A. F.; Barton, J. L.; Cheng, K. J.; Balsara, N. P.; Moore, J. S. et al. An investigation of the ionic conductivity and species crossover of lithiated Nafion 117 in nonaqueous electrolytes. *J. Electrochem. Soc.* **2016**, *163*, A5253–A5262.
- [149] Kwabi, D. G.; Ji, Y. L.; Aziz, M. J. Electrolyte lifetime in aqueous organic redox flow batteries: A critical review. *Chem. Rev.* **2020**, *120*, 6467–6489.
- [150] Liu, T. B.; Wei, X. L.; Nie, Z. M.; Sprenkle, V.; Wang, W. A total organic aqueous redox flow battery employing a low cost and sustainable methyl viologen anolyte and 4-HO-TEMPO catholyte. *Adv. Energy Mater.* **2016**, *6*, 1501449.
- [151] Janoschka, T.; Morgenstern, S.; Hiller, H.; Friebe, C.; Wolkersdörfer, K.; Häupler, B.; Hager, M. D.; Schubert, U. S. Synthesis and characterization of TEMPO- and viologen-polymers for water-based redox-flow batteries. *Polym. Chem.* **2015**, *6*, 7801–7811.
- [152] Pang, S.; Wang, X. Y.; Wang, P.; Ji, Y. L. Biomimetic amino acid functionalized phenazine flow batteries with long lifetime at near-neutral pH. *Angew. Chem., Int. Ed.* **2021**, *60*, 5289–5298.
- [153] Beh, E. S.; de Porcellinis, D.; Gracia, R. L.; Xia, K. T.; Gordon, R. G.; Aziz, M. J. A neutral pH aqueous organic/organometallic redox flow battery with extremely high capacity retention. *ACS Energy Lett.* **2017**, *2*, 639–644.
- [154] Forner-Cuenca, A.; Brushett, F. R. Engineering porous electrodes for next-generation redox flow batteries: Recent progress and opportunities. *Curr. Opin. Electrochem.* **2019**, *18*, 113–122.
- [155] Wu, Q. X.; Lv, Y. H.; Lin, L. Y.; Zhang, X. Y.; Liu, Y.; Zhou, X. L. An improved thin-film electrode for vanadium redox flow batteries enabled by a dual layered structure. *J. Power Sources* **2019**, *410–411*, 152–161.
- [156] Li, G.; Jia, Y. B.; Zhang, S.; Li, X.; Li, J. L.; Li, L. J. The crossover behavior of bromine species in the metal-free flow battery. *J. Appl. Electrochem.* **2017**, *47*, 261–272.
- [157] Vijayakumar, M.; Wang, W.; Nie, Z. M.; Sprenkle, V.; Hu, J. Z. Elucidating the higher stability of vanadium(V) cations in mixed acid based redox flow battery electrolytes. *J. Power Sources* **2013**, *241*, 173–177.
- [158] Wang, R.; Li, Y. S. Carbon electrodes improving electrochemical activity and enhancing mass and charge transports in aqueous flow battery: Status and perspective. *Energy Storage Mater.* **2020**, *31*, 230–251.
- [159] Sun, B.; Skyllas-Kazacos, M. Modification of graphite electrode materials for vanadium redox flow battery application—I. Thermal treatment. *Electrochim. Acta* **1992**, *37*, 1253–1260.
- [160] Yue, L.; Li, W. S.; Sun, F. Q.; Zhao, L. Z.; Xing, L. D. Highly hydroxylated carbon fibres as electrode materials of all-vanadium redox flow battery. *Carbon* **2010**, *48*, 3079–3090.
- [161] Esan, O. C.; Shi, X. Y.; Pan, Z. F.; Huo, X. Y.; An, L.; Zhao, T. S. Modeling and simulation of flow batteries. *Adv. Energy Mater.* **2020**, *10*, 2000758.
- [162] Zhang, W. G.; Xi, J. Y.; Li, Z. H.; Zhou, H. P.; Liu, L.; Wu, Z. H.; Qiu, X. P. Electrochemical activation of graphite felt electrode for VO²⁺/VO₂⁺ redox couple application. *Electrochim. Acta* **2013**, *89*, 429–435.
- [163] Wu, X. W.; Yamamura, T.; Ohta, S.; Zhang, Q. X.; Lv, F. C.; Liu, C. M.; Shirasaki, K.; Satoh, I.; Shikama, T.; Lu, D. et al. Acceleration of the redox kinetics of VO³⁺/VO₂⁺ and V³⁺/V²⁺ couples on carbon paper. *J. Appl. Electrochem.* **2011**, *41*, 1183–1190.
- [164] Singh, A. K.; Pahlevaninezhad, M.; Yasri, N.; Roberts, E. P. L. Degradation of carbon electrodes in the all-vanadium redox flow battery. *ChemSusChem* **2021**, *14*, 2100–2111.
- [165] Jiang, Z.; Klyukin, K.; Alexandrov, V. First-principles study of adsorption-desorption kinetics of aqueous V²⁺/V³⁺ redox species on

- graphite in a vanadium redox flow battery. *Phys. Chem. Chem. Phys.* **2017**, *19*, 14897–14901.
- [166] Hassan, A.; Haile, A. S.; Tzedakis, T.; Hansen, H. A.; de Silva, P. The role of oxygenic groups and sp^3 carbon hybridization in activated graphite electrodes for vanadium redox flow batteries. *ChemSusChem* **2021**, *14*, 3945–3952.
- [167] Moro, F.; Trovò, A.; Bortolin, S.; del Col, D.; Guarnieri, M. An alternative low-loss stack topology for vanadium redox flow battery: Comparative assessment. *J. Power Sources* **2017**, *340*, 229–241.
- [168] Ni, S.; Li, Z. Y.; Yang, J. L. Oxygen molecule dissociation on carbon nanostructures with different types of nitrogen doping. *Nanoscale* **2012**, *4*, 1184–1189.
- [169] Wu, T.; Huang, K. L.; Liu, S. Q.; Zhuang, S. X.; Fang, D.; Li, S.; Lu, D.; Su, A. Q. Hydrothermal ammoniated treatment of PAN-graphite felt for vanadium redox flow battery. *J. Solid State Electrochem.* **2012**, *16*, 579–585.
- [170] Ejigu, A.; Edwards, M.; Walsh, D. A. Synergistic catalyst-support interactions in a graphene- Mn_2O_4 electrocatalyst for vanadium redox flow batteries. *ACS Catal.* **2015**, *5*, 7122–7130.
- [171] Ferre-Vilaplana, A.; Herrero, E. Understanding the chemisorption-based activation mechanism of the oxygen reduction reaction on nitrogen-doped graphitic materials. *Electrochim. Acta* **2016**, *204*, 245–254.
- [172] Xu, A.; Shi, L.; Zeng, L.; Zhao, T. S. First-principle investigations of nitrogen-, boron-, phosphorus-doped graphite electrodes for vanadium redox flow batteries. *Electrochim. Acta* **2019**, *300*, 389–395.
- [173] Gursu, H.; Gencten, M.; Sahin, Y. Synthesis of phosphorus doped graphenes via the yucel's method as the positive electrode of a vanadium redox flow battery. *J. Electrochem. Soc.* **2021**, *168*, 060504.
- [174] Noh, C.; Kwon, B. W.; Chung, Y.; Kwon, Y. Effect of the redox reactivity of vanadium ions enhanced by phosphorylethanolamine based catalyst on the performance of vanadium redox flow battery. *J. Power Sources* **2018**, *406*, 26–34.
- [175] Yang, N.; Zheng, X. Q.; Li, L.; Li, J.; Wei, Z. D. Influence of phosphorus configuration on electronic structure and oxygen reduction reactions of phosphorus-doped graphene. *J. Phys. Chem. C* **2017**, *121*, 19321–19328.
- [176] Zhang, X. L.; Lu, Z. S.; Fu, Z. M.; Tang, Y. A.; Ma, D. W.; Yang, Z. X. The mechanisms of oxygen reduction reaction on phosphorus doped graphene: A first-principles study. *J. Power Sources* **2015**, *276*, 222–229.
- [177] Opar, D. O.; Nankya, R.; Raj, C. J.; Jung, H. *In-situ* functionalization of binder-free three-dimensional boron-doped mesoporous graphene electrocatalyst as a high-performance electrode material for all-vanadium redox flow batteries. *Appl. Mater. Today* **2021**, *22*, 100950.
- [178] Jiang, H. R.; Shyy, W.; Zeng, L.; Zhang, R. H.; Zhao, T. S. Highly efficient and ultra-stable boron-doped graphite felt electrodes for vanadium redox flow batteries. *J. Mater. Chem. A* **2018**, *6*, 13244–13253.
- [179] Park, S. E.; Yang, S. Y.; Kim, K. J. Boron-functionalized carbon felt electrode for enhancing the electrochemical performance of vanadium redox flow batteries. *Appl. Surf. Sci.* **2021**, *546*, 148941.
- [180] Shi, L.; Liu, S. Q.; He, Z.; Yuan, H.; Shen, J. X. Synthesis of boron and nitrogen co-doped carbon nanofiber as efficient metal-free electrocatalyst for the VO_2^+/VO_2^{2+} redox reaction. *Electrochim. Acta* **2015**, *178*, 748–757.
- [181] Su, J. C.; Zhao, Y.; Xi, J. Y. Phosphorus-doped carbon nitride as a powerful electrocatalyst for high-power vanadium flow battery. *Electrochim. Acta* **2018**, *286*, 22–28.
- [182] Li, W. Y.; Liu, J. G.; Yan, C. W. Multi-walled carbon nanotubes used as an electrode reaction catalyst for VO_2^+/VO_2^{2+} for a vanadium redox flow battery. *Carbon* **2011**, *49*, 3463–3470.
- [183] González, Z.; Vizireanu, S.; Dinescu, G.; Blanco, C.; Santamaría, R. Carbon nanowalls thin films as nanostructured electrode materials in vanadium redox flow batteries. *Nano Energy* **2012**, *1*, 833–839.
- [184] Han, P. X.; Yue, Y. H.; Liu, Z. H.; Xu, W.; Zhang, L. X.; Xu, H. X.; Dong, S. M.; Cui, G. L. Graphene oxide nanosheets/multi-walled carbon nanotubes hybrid as an excellent electrocatalytic material towards VO_2^+/VO_2^{2+} redox couples for vanadium redox flow batteries. *Energy Environ. Sci.* **2011**, *4*, 4710–4717.
- [185] Chaudhuri, P.; Lima, C. N.; Frota, H. O.; Ghosh, A. First-principles study of nanotubes of carbon, boron and nitrogen. *Appl. Surf. Sci.* **2019**, *490*, 242–250.
- [186] Jiang, H. R.; Shyy, W.; Wu, M. C.; Wei, L.; Zhao, T. S. Highly active, bi-functional and metal-free B_4C -nanoparticle-modified graphite felt electrodes for vanadium redox flow batteries. *J. Power Sources* **2017**, *365*, 34–42.
- [187] Jeong, S.; Kim, S.; Kwon, Y. Performance enhancement in vanadium redox flow battery using platinum-based electrocatalyst synthesized by polyol process. *Electrochim. Acta* **2013**, *114*, 439–447.
- [188] Sun, B. T.; Skyllas-Kazakos, M. Chemical modification and electrochemical behaviour of graphite fibre in acidic vanadium solution. *Electrochim. Acta* **1991**, *36*, 513–517.
- [189] Yao, C.; Zhang, H. M.; Liu, T.; Li, X. F.; Liu, Z. H. Carbon paper coated with supported tungsten trioxide as novel electrode for all-vanadium flow battery. *J. Power Sources* **2012**, *218*, 455–461.
- [190] Flox, C.; Rubio-Garcia, J.; Nafria, R.; Zamani, R.; Skoumal, M.; Andreu, T.; Arbiol, J.; Cabot, A.; Morante, J. R. Active nano- $CuPt_3$ electrocatalyst supported on graphene for enhancing reactions at the cathode in all-vanadium redox flow batteries. *Carbon* **2012**, *50*, 2372–2374.
- [191] Zhou, H. P.; Xi, J. Y.; Li, Z. H.; Zhang, Z. Y.; Yu, L. H.; Liu, L.; Qiu, X. P.; Chen, L. Q. CeO_2 decorated graphite felt as a high-performance electrode for vanadium redox flow batteries. *RSC Adv.* **2014**, *4*, 61912–61918.
- [192] Yang, F. C.; Mousavie, S. M. A.; Oh, T. K.; Yang, T. R.; Lu, Y. Q.; Farley, C.; Bodnar, R. J.; Niu, L.; Qiao, R.; Li, Z. Sodium-sulfur flow battery for low-cost electrical storage. *Adv. Energy Mater.* **2018**, *8*, 1701991.
- [193] Wei, S. Y.; Xu, S. M.; Agrawal, A.; Choudhury, S.; Lu, Y. Y.; Tu, Z. Y.; Ma, L.; Archer, L. A. A stable room-temperature sodium-sulfur battery. *Nat. Commun.* **2016**, *7*, 11722.
- [194] Li, Z. J.; Lu, Y. C. Polysulfide-based redox flow batteries with long life and low levelized cost enabled by charge-reinforced ion-selective membranes. *Nat. Energy* **2021**, *6*, 517–528.
- [195] Lei, J. F.; Yao, Y. X.; Huang, Y. Q.; Lu, Y. C. A highly reversible low-cost aqueous sulfur-manganese redox flow battery. *ACS Energy Lett.* **2022**, *8*, 429–435.
- [196] Wei, J.; Zhang, P. B.; Liu, Y. Z.; Liang, J. C.; Xia, Y. R.; Tao, A. Y.; Zhang, K. Q.; Tie, Z. X.; Jin, Z. Hypersaline aqueous lithium-ion slurry flow batteries. *ACS Energy Lett.* **2022**, *7*, 862–870.
- [197] Chen, H. N.; Lai, N. C.; Lu, Y. C. Silicon-carbon nanocomposite semi-solid negolyte and its application in redox flow batteries. *Chem. Mater.* **2017**, *29*, 7533–7542.
- [198] Chu, F. J.; Guo, L. B.; Wang, S. C.; Cheng, Y. H. Semi-solid zinc slurry with abundant electron-ion transfer interfaces for aqueous zinc-based flow batteries. *J. Power Sources* **2022**, *535*, 231442.
- [199] Wang, N.; Zhou, R. K.; Zheng, Z. L.; Xin, T.; Hu, M. J.; Wang, B.; Liu, J. Z. Flexible solid-state Zn-polymer batteries with practical functions. *Chem. Eng. J.* **2021**, *425*, 131454.
- [200] Wang, X.; Chai, J. C.; Zhang, S.; Chen, B. B.; Chaturvedi, A.; Cui, G. L.; Jiang, J. J. Insights into Indigo K^+ association in a half-slurry flow battery. *ACS Energy Lett.* **2022**, *7*, 1178–1186.
- [201] Wang, X.; Lashgari, A.; Chai, J. C.; Jiang, J. J. A membrane-free, aqueous/nonaqueous hybrid redox flow battery. *Energy Storage Mater.* **2022**, *45*, 1100–1108.
- [202] Zanzola, E.; Dennison, C. R.; Battistel, A.; Peljo, P.; Vrabel, H.; Amstutz, V.; Girault, H. H. Redox solid energy boosters for flow batteries: Polyaniline as a case study. *Electrochim. Acta* **2017**, *235*, 664–671.



Yingping Liu is a doctoral student in the College of New Energy and Materials, China University of Petroleum, Beijing (CUPB), China. Her main research interests are the application of hydrogels in the field of sensors and smart windows, and the modification of electrolytes and electrodes of iron-chromium flow batteries



Yingchun Niu, a postdoctoral fellow of the China University of Petroleum, Beijing (CUPB), China, studied under academican Chunming Xu. Her research interests are electrode and electrolyte modification in iron/chromium flow batteries



Quan Xu is the vice president of the School of Carbon Neutralization and Future Technology of China University of Petroleum, Beijing (CUPB), China. In 2013, he received his doctorate in the Department of Materials Science and Engineering at the University of North Texas, and joined the CUPB. His research interests focus on long-term energy storage of low-cost large-scale iron-chrome flow batteries